

Measurement of the Production Cross-Section of the Z Boson and Determination of its Spin with the ATLAS Detector

SHALU SOLOMON
DEPARTMENT OF PHYSICS
McGILL UNIVERSITY, MONTREAL

A thesis submitted to McGill University
in partial fulfillment of the requirements for the degree of
MASTER OF SCIENCE
with the support of
the National Sciences and Engineering Research Council (NSERC)
and the Fonds de recherche du Québec - Nature et technologies (FRQNT)

November, 2018

© Shalu Solomon 2018

Abstract

This thesis presents the results of two measurements of the Z boson, one of the mediators of the electroweak force in the Standard Model of particle physics. The first is the measurement of the total and the differential production cross-sections of the Z boson, and the second is the determination of the spin of the particle. The measurements are made with the 6.1 fb^{-1} proton-proton collision data collected by the ATLAS detector in 2016 at a center of mass energy of 13 TeV with the Large Hadron Collider. The leptonic decay of the Z boson into an electron-positron pair is the channel examined. The measurements are compared with the theoretical predictions at next-to-leading order for a quantitative and a precise understanding of the process. The observed results agree with the Standard Model expectations within uncertainties. The total cross-section of Z production in the di-electron channel is measured to be $1.878 \pm 0.02 \text{ (stat)} \begin{smallmatrix} +0.045 \\ -0.052 \end{smallmatrix} \text{ (syst)} \pm 0.042 \text{ (lumi)} \text{ nb}$ and the differential cross-sections as functions of the transverse momentum and the rapidity of the Z particle match with the predictions. The angular distribution of the electrons confirms the spin 1 nature of the Z boson, also in accordance with the Standard Model.

Résumé

Cette thèse présente les résultats de deux mesures du boson Z, l'un des médiateurs de la force d'interaction faible du Modèle Standard de la physique des particules. La première est la mesure des sections efficaces de production totale et différentielle du boson Z, et la deuxième est la détermination du spin de la particule. Les mesures sont effectuées avec les données de collision proton-proton de 6.1 fb^{-1} recueillies par le détecteur ATLAS en 2016 à un centre de masse ayant une énergie de 13 TeV avec le grand collisionneur de hadrons. La désintégration leptonique du boson Z en une paire électron-positron est le canal examiné. Les mesures sont comparées aux prévisions théoriques du second ordre afin de permettre une compréhension quantitative et précise du processus. Les résultats observés concordent avec les prédictions du Modèle Standard dans la limite des incertitudes. La section transversale totale de la production de Z dans le canal di-électron est mesurée à $1.878 \pm 0.02 \text{ (stat)}^{+0.045}_{-0.052} \text{ (syst)} \pm 0.042 \text{ (lumi)} \text{ nb}$ et les sections efficaces différentielles en fonction de la quantité de mouvement transversal et de la rapidité de la particule Z correspondent aux prévisions. La distribution angulaire des électrons confirme la nature du spin 1 du boson Z, également conformément au Modèle Standard.

“As we conquer peak after peak we see in front of us regions full of interest and beauty, but we do not see our goal, we do not see the horizon; in the distance tower still higher peaks, which will yield to those who ascend them still wider prospects, and deepen the feeling, the truth of which is emphasized by every advance in science, that ‘Great are the Works of the Lord’.”

J.J. Thomson
Nature 81 (1909):257

Acknowledgments

First, I would like to express my sincere gratitude to my supervisor, Prof. François Corriveau, for giving me the opportunity to work on the ATLAS experiment. His valuable guidance, support, and encouragement paved the way towards completing this thesis. I cannot forget how you have always backed my research aspirations.

I am eternally grateful to Dr. Heather Russell, McGill research associate, without whom I would not have made it this far. I cannot thank you enough for being who you have been to me, patiently enduring my mistakes from the first compilation to the luminosity calculation. At the end of these two years, I realize that I have run to you for almost everything, not just for my analysis. I still wonder how you manage to keep all the twikis at your fingertips!

To the McGill ATLAS group for being a wonderful team to work with. I am indebted to my family, especially my mother, for always believing in me and loving me immensely. My deep gratitude to Carlo Parisi and Mirella Facchini for giving me a home and a reason to visit Montreal again. At the end of the day, I know I can always count on you.

To all my friends, special mention to Christina Nelson, Zahra Zahree, Matt Hodel and Mir Faruk. Words cannot express how much I owe you. Thank you for all the laughter, fun and memories we shared together.

Author's Contribution

The analysis and the results presented in this thesis are the author's original work. All the chapters in this thesis are written by the author.

- The analysis is performed within the ATLAS Athena software framework, built on the contributions of thousands of people across the world over the years.
- The author's contributions to the analysis begin from Chapter 6 onwards.
- The Monte Carlo samples used for spin 0 and spin 2 particles in Chapter 11 are generated by Dr. Heather Russell.

This work is dedicated to Dr. Laly Pothan for her endless support.

Contents

Abstract	iii
Résumé	iv
Acknowledgments	v
Author’s Contribution	vi
Dedication	vii
OVERVIEW	1
1 Introduction	2
2 Theory	5
2.1 Standard Model	5
2.1.1 Introduction	6
2.1.2 Particle Content in the Standard Model	7
2.1.3 Mathematical Formalism	8
2.2 Phenomenology of Proton–Proton Collisions	16

3	Z Boson Production at the LHC and Monte Carlo Generators	22
3.1	Z Boson Production	22
3.2	Monte Carlo Event Generators	27
4	The Large Hadron Collider	30
4.1	Introduction	30
4.2	Accelerator Complex at CERN	31
4.3	Vacuum System	32
4.4	Magnetic System and Cryogenics	33
4.5	Proton Bunching	35
4.6	Luminosity	36
4.6.1	Instantaneous Luminosity	36
4.6.2	Integrated Luminosity	37
5	The ATLAS Experiment	38
5.1	Introduction	38
5.2	Coordinate System	39
5.3	Sub-Detector Systems	41
5.3.1	The Inner Detector	41
5.3.2	The Calorimeter	43
5.3.3	The Muon Spectrometer	44
5.3.4	The Magnet System	45
5.4	Trigger and Data Acquisition	45
6	Electron Reconstruction	48
6.1	Electron Reconstruction	48

6.2	Electron Background	50
6.3	Electron Identification	53
6.4	Electron Isolation	54
7	Event Selection and Signal Extraction	56
7.1	Selection Criteria	56
7.2	Electron Distribution	58
7.3	Reconstruction Method	62
8	Z Boson Reconstruction	65
8.1	Invariant Mass Reconstruction	65
8.2	Unfolding	70
8.3	Mass and Width Measurements	71
8.4	Geometric and Kinematic Distributions	74
	CROSS-SECTION MEASUREMENT	77
9	Results	78
9.1	Total Cross-Section Measurement	78
9.1.1	Uncertainties	80
9.2	Differential Cross-Section Measurement	85
9.2.1	Transverse Momentum Distribution	85
9.2.2	Rapidity Distribution	86
9.3	Summary	92

SPIN VERIFICATION	94
10 Collins Soper Frame	95
11 Results	103
SUMMARY	108
12 Conclusion and Outlook	109
Appendix A	112
Appendix B	116
Appendix C	119
Appendix D	124
Glossary	126
References	129

Part I

Overview

Chapter 1

Introduction

The modern theory of particle physics called the Standard Model (SM) is a scientifically stunning piece of work which theorizes and predicts the framework of the universe. The Z boson is a pivotal figure in the SM as one of the mediators of the electroweak force. This massive particle is produced abundantly at the Large Hadron Collider (LHC), which is located at the research center CERN in Geneva and is at present the biggest Z factory. Adorned as an engineering marvel, this hadron collider is the world's largest and most powerful accelerator machine that smashes hadrons, mainly protons, at extremely high energies. The proton beams are accelerated to nearly the speed of light and are then collided at a center of mass energy of 13 TeV, which is the largest ever reached in a laboratory. The energy released in these collisions materializes in the form of new particles like quarks, leptons, gluons or even massive bosons including the Z and the Higgs. The LHC collides protons at four main points along its accelerator ring where huge detectors are housed to detect the particles produced. The ATLAS detector is one such gigantic detector which acts like a huge camera capturing

almost all the particles formed from the high energy collisions.

The ATLAS experiment has garnered some serious attention with its remarkable contribution to the discovery of the Higgs boson, the latest solved puzzle in the SM. The ATLAS experiment is constantly advancing in its search for new physics including dark matter, heavy quarks, new symmetries etc. Therefore, it is very important to understand the detector and assessing its reliability before answering these questions. This is done by measuring some standard physics processes and one such interesting process is the production and the subsequent decay of the Z boson. Z production was a well understood and a precisely measured process at the Large Electron-Positron Collider (LEP), an earlier lepton collider at CERN. Re-measuring the process with ATLAS at the LHC is vital to apprehend how the detector behaves and its reliability as ATLAS is venturing into new discoveries.

With very high production rate and clean decay signatures, Z production serves as a benchmark process to calibrate the detector. Furthermore, the production of the Z boson is an important tool to validate the predictions of the Standard Model and is also sensitive to new physics beyond the SM. Z production is highly useful to test the calculations of perturbative Quantum Chromodynamics (QCD) and to determine the Parton Distribution Functions (PDFs) [1]. The Z bosons produced at large transverse momenta can constrain the gluon PDFs as well [2]. Moreover, the Z production channel was instrumental in the discovery of the Higgs boson [3,4]. In addition, it also served as a standard reference for the recent precise measurement of the W boson mass [5,6].

The primary objective of this thesis is to measure the total and the differential production cross-sections of the Z boson in the electron-positron channel. A preliminary study of determining the spin of the Z particle is also done as an extension to the cross-section measurement.

The chapters in this thesis are arranged into four parts and the outline is as follows: Part I consists of all the chapters up to Chapter 8 and includes the underpinning information of the analysis: theory, tools, analysis techniques and procedures. A brief introduction to the theory of Standard Model and to the phenomenology of proton-proton collisions is given in Chapter 2. Chapter 3 discusses Z production at the LHC in a nutshell. An overview of the LHC and the ATLAS experiment is given in Chapter 4 and Chapter 5 respectively. Chapter 6 describes briefly the electron reconstruction procedure. The analysis methodology begins in Chapter 7 which discusses the selection criteria employed in the study. The Z reconstruction procedure is detailed in Chapter 8. Part II of the thesis consists of Chapter 9 which presents the cross-section measurement and the results. In Part III, Chapter 10 and Chapter 11 discuss the method and the results of the spin measurement. A general conclusion to the work is given in Chapter 12, which comes under Part IV.

Chapter 2

Theory

2.1 Standard Model

The ordinary matter in the universe is made up of a small number of fundamental particles governed by the four forces of nature: gravitational, electromagnetic, electroweak and strong forces. Our current best understanding of the phenomenology of particle physics is condensed into a theoretical framework called the Standard Model (SM) [7–9], which beautifully describes the fundamental constituents of matter and all the associated interactions except gravity.¹ In the SM, the fundamental particles that make up the matter are *fermions*, with an intrinsic spin $\frac{1}{2}$. The *force carriers*, which mediate an interaction between the matter particles, are *bosons* with an intrinsic spin 1, also known as vector bosons. Fermions can possess different *charge* quantum numbers which determine the type of their associated interactions (e.g color charge, hypercharge, weak isospin). A summary of the SM constituents is shown in Figure 2.1.

¹Compared to the other forces, gravity is weaker by nearly 37 orders of magnitude. Hence, the effect of gravity on elementary particles is negligible.

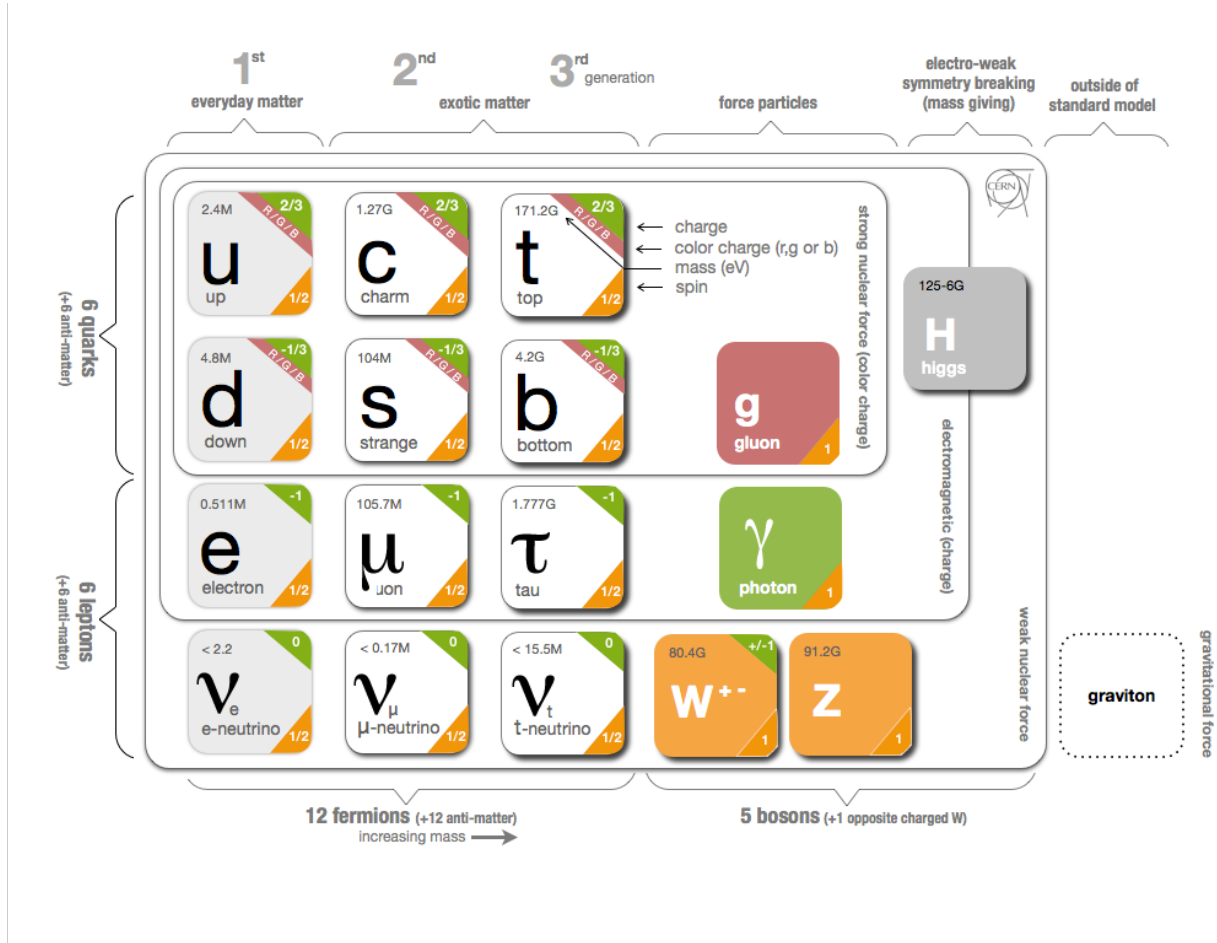


Figure 2.1: Fundamental particles in the Standard Model of particle physics [10].

2.1.1 Introduction

The Standard Model is a renormalizable gauge quantum field theory. The underlying gauge symmetry of the SM is a product of three unitary Lie groups,

$$\underbrace{SU(3)_C}_{\text{strong}} \otimes \underbrace{SU(2)_L \otimes U(1)_Y}_{\text{electroweak}}. \tag{2.1}$$

The $SU(3)_C$ symmetry group describes the strong force, which acts on all particles that carry a color charge. The electroweak interaction described by $SU(2)_L \otimes U(1)_Y$ unifies the electromagnetic and the weak forces. The $SU(2)_L$ symmetry group acts only on left-handed particles with a weak isospin, while $U(1)_Y$ acts on particles carrying a weak hypercharge. The SM is a gauge theory, which means that the Lagrangian describing the physical state has to be invariant under local gauge transformations. To satisfy this gauge invariance, new vector fields or gauge fields have to be introduced in the Lagrangian. The quanta of the gauge fields are called the *gauge* or *vector bosons* which mediate the interactions between the fermions. The electroweak symmetry is spontaneously broken through the Higgs mechanism, as a result of which the SM particles acquire mass. The Higgs mechanism also predicted a new particle called the *Higgs boson* having a spin 0, which was discovered in 2012 at the LHC [3,4].

2.1.2 Particle Content in the Standard Model

Fermions

Fermions, or matter particles, are categorized into *quarks* and *leptons* depending on their interaction with the strong field. Quarks carry the color quantum number and can interact via the strong interaction while leptons cannot. All fermions, however, participate in weak interaction. Quarks and leptons are classified into three generations in the order of increasing mass. Ordinary matter is built from the first generation fermions, while second and third generations are heavier cousins of the first. Quarks occur in six *flavours* each carrying a color and an electric charge, thus taking part in both strong and electromagnetic interactions. Each lepton generation consists of an electrically charged massive fermion along

with an associated electrically neutral *neutrino*. Therefore, neutrinos can only interact via the weak force.

Bosons

The force carriers in the SM are vector bosons. The electromagnetic interaction is mediated by a massless, electrically neutral *photon* while the mediators of the strong force are eight massless *gluons*, which carry color charge. Gluons are electrically neutral as well. Unlike the electromagnetic and the strong interactions, the mediators of the weak force are the very massive *Z* and *W bosons*. The massive nature of these particles restricts the force range to short distances.² The *Z* boson has an electric charge of 0, while the *W* bosons occur in two oppositely signed unit charges. In the SM, the fermions and the weak gauge bosons acquire mass as a consequence of the Higgs mechanism, described in detail in Section 2.1.3. The Higgs boson, which is a massive excitation of the Higgs field, is the only known fundamental scalar particle in the SM. The origin of the mass of the Higgs particle is currently at the forefront of research in particle physics.

2.1.3 Mathematical Formalism

The SM, like any other quantum field theory [11], integrates quantum mechanics with special relativity. Schrödinger's equation is a momentous contribution to the field of quantum mechanics but it fails to explain the creation and annihilation of particles. To consistently include both relativistic and quantum mechanical limits, one has to turn to the framework of quantum field theory. According to the theory, the equation for the free propagation of a

²Electromagnetic interaction is long-ranged due to the massless nature of photon. Even though gluons are massless, their self-interaction prevents them from propagating to long distances.

fermion with mass m is given by:

$$(i\gamma^\mu\partial_\mu - m)\psi = 0, \quad (2.2)$$

and the corresponding Lagrangian density is:

$$\mathcal{L} = \bar{\psi}(i\gamma^\mu\partial_\mu - m)\psi. \quad (2.3)$$

The Lagrangian density is invariant under a global phase transformation of the form $\psi \rightarrow e^{iq\alpha}\psi$, where α is a constant and q is the fermion charge. This is the $U(1)$ symmetry group. But according to the SM requirements, the Lagrangian density must satisfy local gauge invariance as well, thus obeying transformations of the type $\psi \rightarrow e^{iq\alpha(x)}\psi$. The Lagrangian density given by Equation 2.3, is not invariant under the local phase transformation. To achieve this invariance, the derivative ∂_μ in the equation has to be replaced by a covariant derivative $\mathcal{D}_\mu = \partial_\mu - iqA_\mu$. The covariant derivative introduces a new vector field A_μ called the electromagnetic vector field, and the Lagrangian density becomes:

$$\begin{aligned} \mathcal{L} &= \bar{\psi}(i\gamma^\mu\mathcal{D}_\mu - m)\psi \\ &= \bar{\psi}i\gamma^\mu\partial_\mu\psi - m\bar{\psi}\psi - q\bar{\psi}\gamma^\mu A_\mu\psi. \end{aligned} \quad (2.4)$$

The field theory that describes the interaction of a fermion with the electromagnetic field via the exchange of the respective gauge boson is called *Quantum Electrodynamics* (QED). In this theory, the mediating gauge boson is a massless photon. Taking into account the kinetic term of the gauge field as well in Equation 2.4, the QED Lagrangian density can be

written as:

$$\mathcal{L}_{QED} = \underbrace{\bar{\psi}i\gamma^\mu\partial_\mu\psi}_{\text{fermion kinetic term}} - \underbrace{m\bar{\psi}\psi}_{\text{fermion mass term}} - \underbrace{\frac{1}{4}\mathcal{F}^{\mu\nu}\mathcal{F}_{\mu\nu}}_{\text{field kinetic term}} - \underbrace{q\bar{\psi}\gamma^\mu A_\mu\psi}_{\text{interaction term}}, \quad (2.5)$$

where $\mathcal{F}_{\mu\nu} = \partial_\mu A_\nu - \partial_\nu A_\mu$ is the electromagnetic field tensor. A mass term for the photon violates the gauge invariance, hence it cannot be included in the Lagrangian density. QED is an abelian gauge theory, therefore it disallows any photon self-interaction terms.³

The strong interaction is described by a gauge theory called *Quantum Chromodynamics* (QCD) [12, 13], built on the $SU(3)_C$ symmetry group that conserves the color charge. Only quarks and gluons carry color charge and thus participate in strong interactions, while other bosons and leptons do not. The three color quantum numbers are r for red, g for green and b for blue.⁴ To achieve local gauge invariance, ∂_μ in Equation 2.3 is replaced by a covariant derivative $\mathcal{D}_\mu = \partial_\mu - ig_3 T_a G_{a\mu}$, where T_a are the eight generators of $SU(3)$ that satisfy the commutation relation $[T_a, T_b] = if_{abc}T_c$ and G_a corresponds to each of the eight gluon fields ($a, b, c \in 1, \dots, 8$). f_{abc} are the structure constants of $SU(3)$ and g_3 is the coupling strength of the gluon field. The QCD Lagrangian density is given by

$$\mathcal{L}_{QCD} = \underbrace{\bar{\psi}_f i\gamma^\mu \partial_\mu \psi_f}_{\text{quark kinetic term}} - \underbrace{m\bar{\psi}_f \psi_f}_{\text{quark mass term}} - \underbrace{\frac{1}{4}\mathcal{G}_a^{\mu\nu}\mathcal{G}_{a\mu\nu}}_{\text{field kinetic term}} - \underbrace{g_3\bar{\psi}_f \gamma^\mu T_a G_{a\mu} \psi_f}_{\text{interaction term}}, \quad (2.6)$$

where $\mathcal{G}_a^{\mu\nu} = \partial^\mu G_a^\nu - \partial^\nu G_a^\mu - g_3 f_{abc} G_b^\mu G_c^\nu$ is the gluon field strength tensor. The subscript f on the field denotes the quark flavour, ($f \in 1, \dots, 6$), summed over all the colors. QCD is

³Self-interactions come from the commutator of the gauge field in the field strength, \mathcal{F} in this case. Therefore, abelian (or commutative) theories have no such self-interactions.

⁴The colors are just a naming convention with no physical meaning.

a non-abelian theory, thus allowing for gluon self-interactions as seen by the cubic and the quartic terms in the Lagrangian density.

Electroweak Interaction

The symmetry group underlying the electroweak interaction [14–16] is $SU(2)_L \otimes U(1)_Y$. $SU(2)_L$ conserves the weak isospin (I) and couples only to left-handed fermions as denoted by the index L . But $U(1)_Y$, the symmetry group of weak hypercharge (Y), couples to both left- and right-handed particles. The covariant derivative describing the electroweak force is given by:

$$\mathcal{D}_\mu = \partial_\mu - ig_2 \frac{\sigma^a}{2} W_\mu^a - ig_1 B_\mu. \quad (2.7)$$

Here, Pauli matrices denoted by $\frac{\sigma^a}{2}$ with $a \in 1, 2, 3$ are the three generators of the $SU(2)$ symmetry group. The three massless vector fields W_μ^a with the field tensor $\mathcal{W}_{\mu\nu}^a = \partial_\mu W_\nu^a - \partial_\nu W_\mu^a$ are introduced to preserve the local $SU(2)_L$ transformations. $U(1)_Y$ introduces an additional massless vector field B_μ and the field tensor $\mathcal{B}_{\mu\nu} = \partial_\mu B_\nu - \partial_\nu B_\mu$. The physically observable fields of the gauge bosons mediating the electroweak force are superpositions of the four fields described by W_μ^a and B_μ . The mixing depends on the coupling strength of the fields and the mixing angle is called the Weinberg angle denoted by θ_W . Equation 2.8 gives the vector fields for W^+ and W^- bosons. The Z boson and the photon fields are given by Equations 2.9 and 2.10 respectively.

$$W_\mu^\pm = \frac{1}{\sqrt{2}}(W_\mu^1 \mp iW_\mu^2) \quad (2.8)$$

$$Z_\mu = W_\mu^3 \cos \theta_W - B_\mu \sin \theta_W \quad (2.9)$$

$$A_\mu = W_\mu^3 \sin \theta_W + B_\mu \cos \theta_W \quad (2.10)$$

$$\text{where } \cos \theta_W = \frac{g_2}{\sqrt{g_1^2 + g_2^2}} \quad \text{and} \quad \sin \theta_W = \frac{g_1}{\sqrt{g_1^2 + g_2^2}}.$$

The Lagrangian density describing the electroweak interaction is written as:

$$\begin{aligned} \mathcal{L}_{electroweak} = & \underbrace{\bar{\psi}_L i \gamma^\mu \partial_\mu \psi_L}_{\text{left-handed}} + \underbrace{\bar{\psi}_R i \gamma^\mu \partial_\mu \psi_R}_{\text{right-handed}} && \text{fermion kinetic terms} \\ & - \underbrace{\frac{g_2}{2} \bar{\psi}_L \gamma^\mu \sigma^a W_\mu^a \psi_L - \frac{g_1}{2} \bar{\psi}_L \gamma^\mu \sigma^0 B_\mu \psi_L}_{\text{left-handed}} - \underbrace{\frac{g_1}{2} \bar{\psi}_R \gamma^\mu B_\mu \psi_R}_{\text{right-handed}} && \text{fermion interaction terms} \\ & - \frac{1}{4} \mathcal{W}^{\alpha\mu\nu} \mathcal{W}_{\mu\nu}^\alpha - \frac{1}{4} \mathcal{B}^{\mu\nu} \mathcal{B}_{\mu\nu} && \text{gauge field kinetic and self-interaction terms} \end{aligned} \tag{2.11}$$

The non-abelian nature of the electroweak theory allows for the cubic and the quartic self-interaction terms for W and Z bosons. It is evident that the gauge bosons emerging from the vector fields are massless, as constrained by the local gauge invariance. Today, it is a known fact that a photon is massless but W and Z bosons have exceptionally large masses. Even if the local gauge invariance is ignored, adding mass terms by hand for W and Z bosons results in non-renormalizable divergences, rendering the theory meaningless. This problem is solved by the Higgs mechanism [17, 18], as a consequence of which W and Z bosons acquire mass while photons remain massless. The W and Z bosons were discovered [19, 20] at CERN in the 1980s and the experimentally observed mass of these particles matched well with the predictions, which was one of the early achievements of the SM. A brief description of the Higgs mechanism and how particles acquire mass is given below.

Higgs Mechanism

A locally gauge invariant $SU(2)_L \otimes U(1)_Y$ symmetry forbids the existence of massive gauge bosons. To introduce the mass terms and to keep the theory renormalizable, the symmetry has to be spontaneously broken, which means that the Lagrangian is invariant under the electroweak transformation but the states are not. For this, a new complex scalar field φ with a specific potential is introduced. To keep the Lagrangian invariant, only $SU(2)_L \otimes U(1)_Y$ multiplets can be added and the simplest one is an isospin doublet as given in Equation 2.12. The electric charges of the two field components ensure a hypercharge $Y = +1$. This choice of the fields leaves the photon massless after the symmetry breaking, which will become clear from the discussion below.

$$\varphi = \begin{pmatrix} \phi^+ \\ \phi^0 \end{pmatrix} = \frac{1}{\sqrt{2}} \begin{pmatrix} \phi_1 + i\phi_2 \\ \phi_3 + i\phi_4 \end{pmatrix} \quad (2.12)$$

The Lagrangian density for the scalar field is given by:

$$\mathcal{L} = (\mathcal{D}^\mu \varphi)^\dagger (\mathcal{D}_\mu \varphi) - V(\varphi), \quad (2.13)$$

where \mathcal{D}_μ is the covariant derivative of $SU(2)_L \otimes U(1)_Y$ symmetry group [see Equation 2.7]. The potential added to spontaneously break the symmetry is denoted by $V(\varphi)$, according to Equation 2.14, with $\mu^2 < 0$ and $\lambda > 0$. A pictorial representation of the potential is also shown in Figure 2.2.

$$V(\varphi) = \mu^2 \varphi^2 + \lambda \varphi^4 \quad (2.14)$$

From Equation 2.14, it is obvious that there is not a single vacuum but an infinite number

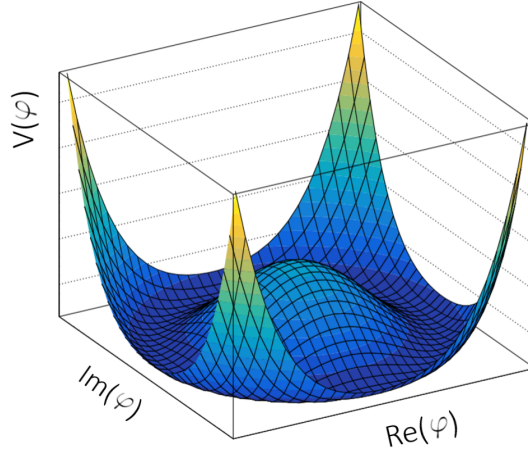


Figure 2.2: A pictorial representation of the potential $V(\varphi)$ of the complex scalar field [21].

of vacua located at:

$$\varphi_{min}^2 = (\phi_1^2 + \phi_2^2 + \phi_3^2 + \phi_4^2)_{min} = -\frac{\mu^2}{2\lambda}, \quad (2.15)$$

on a four-dimensional hypersphere,⁵ in the φ hyperplane.⁶ One is free to choose any of the vacuum states and the chosen vacuum here is at:

$$\phi_{1,min}^2 = \phi_{2,min}^2 = \phi_{4,min}^2 = 0 \quad \text{and} \quad \phi_{3,min}^2 = -\frac{\mu^2}{2\lambda} = \nu^2, \quad (2.16)$$

where ν is the vacuum expectation value for which $V(\varphi)$ is minimized. The vacuum can be written as:

$$\varphi_0 = \frac{1}{\sqrt{2}} \begin{pmatrix} 0 \\ \nu \end{pmatrix}, \quad \text{where } \nu = \sqrt{\frac{-\mu^2}{\lambda}}. \quad (2.17)$$

Currently, there are three massless degrees of freedom associated with the vacuum of the φ field. The Lagrangian is studied under small oscillations around the vacuum and within the

⁵A hypersphere is an n-dimensional sphere.

⁶A hyperplane is an n-dimensional plane.

freedom of gauge invariance, φ can be re-formulated. Perturbations around the vacuum in a direction away from the potential minimum correspond to a real massive scalar field called the Higgs field denoted by h , and the new vacuum can be written as:

$$\varphi_0 = \frac{1}{\sqrt{2}} \begin{pmatrix} 0 \\ \nu + h \end{pmatrix} \quad (2.18)$$

One can notice that the vacuum defined is neutral. It is because, with hypercharge $Y = +1$, weak isospin $I = \frac{1}{2}$ and its third component $I_3 = -\frac{1}{2}$, the electric charge $Q = I_3 + \frac{1}{2}Y$ yields 0. This choice of vacuum breaks the $SU(2)_L \otimes U(1)_Y$ symmetry completely but leaves $U(1)_{EM}$ invariant, which is the reason why photons are still massless after the symmetry breaking.

Using the new definition of φ , the Higgs sector of the Lagrangian density can be written as:

$$\begin{aligned} \mathcal{L} = & \frac{1}{2} \partial_\mu h \partial^\mu h & - & \lambda \nu^2 h^2 & & \text{Kinetic and mass terms} \\ & & & & & \text{of the Higgs field} \\ & + \frac{1}{2} \left(\frac{g_2^2 \nu^2}{4} (|W_\mu^+|^2 + |W_\mu^-|^2) + \frac{\nu^2}{4} (g_1^2 + g_2^2) |Z_\mu|^2 \right) & & & & \text{Mass terms of} \\ & & & & & \text{W}^\pm \text{ and Z bosons} \\ & + \frac{g^2 \nu}{4} (|W_\mu^+|^2 + |W_\mu^-|^2) h + \frac{g^2}{8} (|W_\mu^+|^2 + |W_\mu^-|^2) h^2 & & & & \text{Coupling of the W}^\pm \text{ boson} \\ & & & & & \text{to the Higgs field} \\ & + \frac{\nu^2}{4} (g_1^2 + g_2^2) |Z_\mu|^2 h + \frac{1}{8} (g_1^2 + g_2^2) |Z_\mu|^2 h^2 & & & & \text{Coupling of the Z boson} \\ & & & & & \text{to the Higgs field} \\ & - \lambda \nu h^3 & - & \frac{\lambda}{4} h^4 & & \text{Self-interaction terms} \\ & & & & & \text{of the Higgs field} \\ & + \text{constant.} & & & & \end{aligned} \quad (2.19)$$

From the above equation, masses of the electroweak gauge bosons can be identified as:

$$m_{W^\pm} = \frac{1}{2}\nu g_2, \quad m_Z = \frac{1}{2}\nu\sqrt{g_1^2 + g_2^2}, \quad m_A = 0. \quad (2.20)$$

The massive excitation of the Higgs field gives rise to the scalar Higgs boson with mass $m_h = \nu\sqrt{2\lambda}$. Fermionic masses can be generated in a similar way by including additional Lagrangian terms that describe the coupling of the Higgs field with the fermionic fields. The more the fermions interact with the Higgs field, the more mass they acquire. The fermion masses are thus generated as $m_f = \frac{y_e\nu}{\sqrt{2}}$, where the Yukawa coupling, y_e , is a free parameter in the model.

2.2 Phenomenology of Proton–Proton Collisions

The LHC collides protons at tremendously high energies, and to study the proton–proton collisions, it is essential to first understand the structure of a proton. A proton is a composite particle primarily made up of two *up* and one *down* quarks, which are called the *valence* quarks. In the high energy collider environment, this structure of the proton is too simple to explain the observed aftermath of the collision.

The proton structure at high energies is better explained by the Parton Model [22] proposed by Richard Feynman. According to this model, in addition to the valence quarks, a high energy proton consists of a sea of quarks, anti-quarks and gluons, where each constituent particle is referred to as a *parton*. The momentum distribution of partons within the proton depends on the momentum carried by the proton. This information of the proton’s deep structure is encoded as probability density functions known as the Parton Distribution

Functions (PDFs), given by $f(x_i, Q^2)$ as shown in Figure 2.3. It defines the probability density of finding a parton of type i carrying a fraction x_i of the total momentum x of the proton when the proton is probed at a momentum transfer Q^2 .

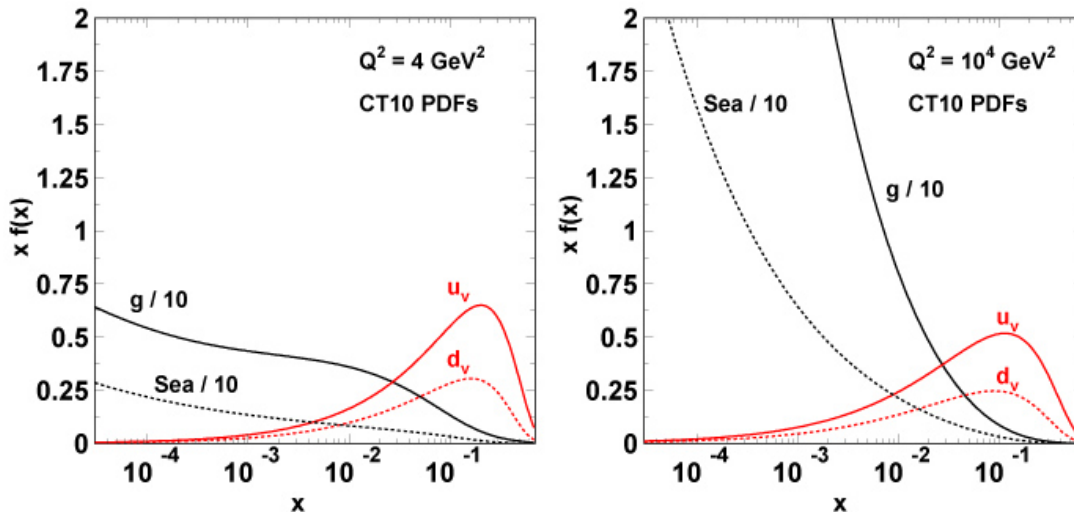


Figure 2.3: Parton distribution functions at $Q^2 = 4 \text{ GeV}^2$ and 10^4 GeV^2 [23].

In a high energy proton, there is no relative motion between the partons inside. This is because, from the proton’s reference frame, time is dilated according to the special theory of relativity and the partons are more or less “frozen”. Proton-proton collision at the LHC is essentially a parton–parton collision where a parton from one proton hits another from the other proton.

If the colliding partons are energetic enough to cause an inelastic collision, then the process is termed a *hard scatter*. The incoming partons and the outgoing particles can emit secondary radiation known as *Initial State Radiation* (ISR) and *Final State Radiation* (FSR) respectively. The remaining partons along with the non-interacting protons form the

underlying event. The parton remnant undergoes a process called *hadronization*, where the partons re-arrange themselves to form stable colorless hadrons. A diagrammatic view of a typical proton–proton collision at the LHC is shown in Figure 2.4.

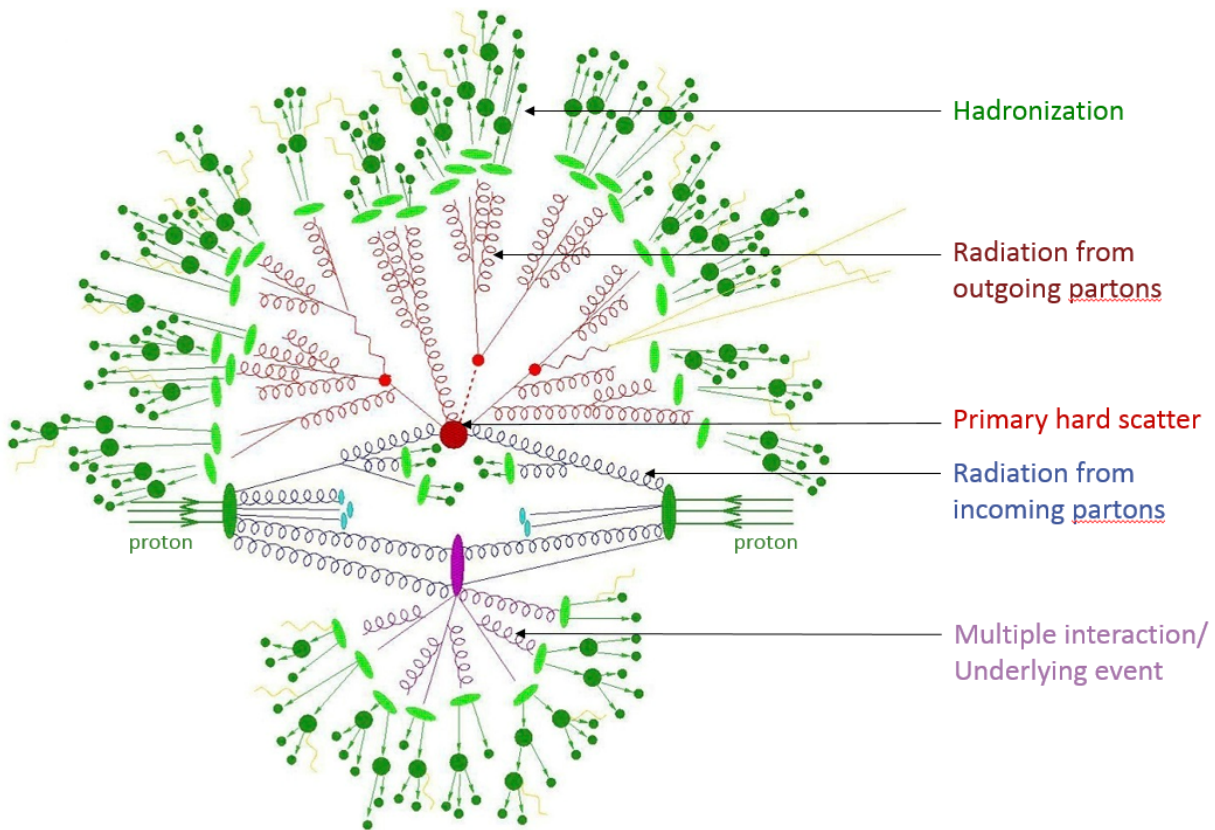


Figure 2.4: A graphic representation of a typical proton–proton collision at the LHC [24].

Cross-section

One of the principal quantities in particle physics studies is the interaction cross-section σ of a process. It is a physical quantity proportional to the probability for a given interaction to happen. A cross-section has the units of area and is usually expressed in *barns* (1 barn = 10^{-28}m^2).

To compute the cross-section of processes from hadronic collisions, the QCD factorization theorem is used. The factorization theorem allows the cross-section to be separated into perturbative partonic cross-section and parton distribution functions, which are determined empirically. In the proton–proton collisions at the LHC, the cross-section for any process $pp \rightarrow X$ can be expressed mathematically as:

$$\sigma_{pp \rightarrow X} = \sum_{a,b=q,\bar{q},g} \int_0^1 dx_a \int_0^1 dx_b f_a(x_a, Q^2) f_b(x_b, Q^2) \sigma_{ab \rightarrow X}, \quad (2.21)$$

where a and b denote the parton type in each of the colliding protons and $\sigma_{ab \rightarrow X}$ stands for the partonic cross-section of the process $ab \rightarrow X$. Perturbative QCD (pQCD) applies perturbation theory techniques to QCD. pQCD makes the partonic cross-section predictable as a result of the QCD asymptotic freedom. Partonic cross-section $\sigma_{ab \rightarrow X}$ computed using pQCD can be expressed as:

$$\sigma_{ab \rightarrow X} = \sigma_0 + \alpha_s(Q^2, \mu_R^2) \sigma_1 + \alpha_s^2(Q^2, \mu_R^2) \sigma_2 + \dots \quad (2.22)$$

where α_s is the strong coupling constant and μ_R is the renormalization scale. The first term, σ_0 , is the tree-level or the leading order (LO) partonic cross-section [25, 26]. It can be calcu-

lated by integrating over the momentum phase space the sum of all the tree-level Feynman diagrams for the process. The second term corresponds to the next-to-leading order (NLO) cross-section and the third term to the next-to-next-leading order (NNLO). These higher order terms in α_s are associated with radiative corrections as a result of gluon or quark emission.

A remarkable trait of cross-section is that it encapsulates all the properties of the interacting particles including spin. A particle’s spin is relevant as it is the foremost quantity that reveals its dynamics. In addition to cross-section measurement, this thesis also presents a preliminary study of particle spin measurement.

Spin

The spin of a particle determines how it interacts. The existence of a spin quantum number was first inferred experimentally by O. Stern and W. Gerlach [27] and the results were decisive in revolutionizing how we understood quantum physics.

The physics principle underlying a laboratory spin measurement is the fundamental angular momentum conservation law of quantum mechanics, which states that, for an isolated system of interacting particles, the total angular momentum must always be conserved. The total angular momentum, \vec{J} , of a system (or a particle) combines its orbital angular momentum, \vec{L} and its intrinsic spin, \vec{S} , denoted by

$$\vec{J} = \vec{L} + \vec{S}. \tag{2.23}$$

As mentioned earlier, the conservation of angular momentum is vital to any system. Therefore, the total angular momentum of the system must remain the same before and after an interaction (e.g. a particle decay) according to

$$\sum_{i=1}^n \vec{J}_{\text{initial}} = \sum_{i=1}^n \vec{J}_{\text{final}}. \quad (2.24)$$

This is the ground rule for calculating the spin of a system. Further details on the steps involved in measuring the spin in a collider environment are described in Chapter 10.

The collision phenomenology briefed in this section serves as the basis to quantify Z production at the LHC and to determine its intrinsic spin which are the objectives of this thesis. The following chapter discusses the theory of the production of the Z particle at the LHC in a nutshell. The chapter highlights some of the Z production mechanisms, decay, higher order corrections as well as a small introduction to how the process is modeled at the LHC.

Chapter 3

Z Boson Production at the LHC and Monte Carlo Generators

3.1 Z Boson Production

The Z boson is a massive neutral vector boson mediating the electroweak interaction. The particle was discovered in the early 1980s at the Super Proton Synchrotron (SPS), CERN [20, 28]. At present, the LHC is the largest Z factory in the world, delivering Z production cross-section in nanobarns! [see Figure 3.1]. At the LHC, a predominant mechanism for Z boson production is the direct parton-parton interaction during the collision through the Drell-Yan (DY) process. In a DY process, a quark and an anti-quark from the incoming protons annihilate to produce an intermediate vector boson, either a Z boson or a virtual off mass-shell photon γ^* or even a mixture of the two, which then decays leptonically. Both of the intermediate bosons have the same quantum numbers. Therefore, the quantum numbers of the incoming and the outgoing particles are conserved, if the mediator is a Z boson or a

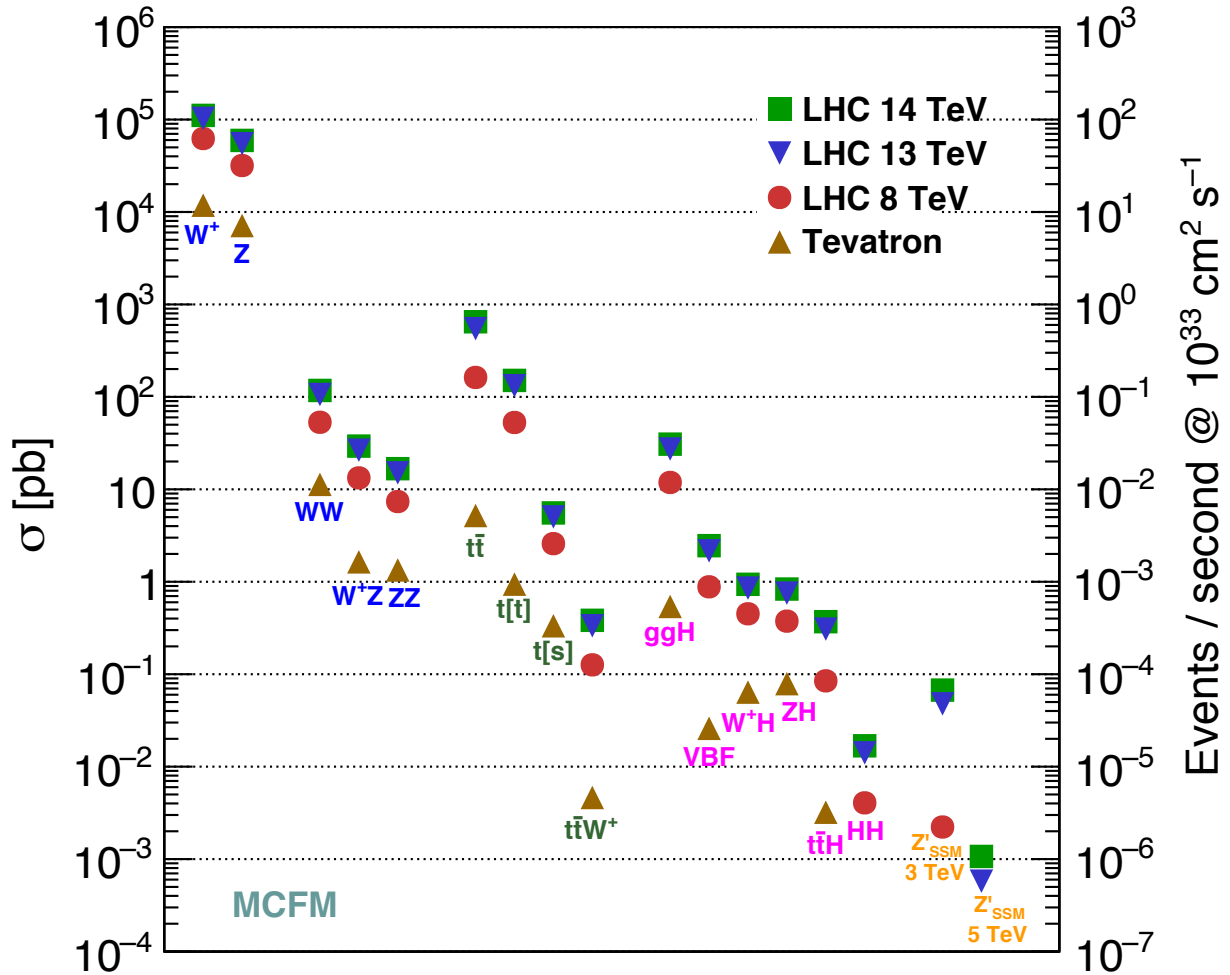


Figure 3.1: Cross-sections calculated using the MCFM generator for various particle production mechanisms in the Tevatron's $p\bar{p}$ collisions at $\sqrt{s} = 1.96$ TeV and in the LHC's pp collisions at $\sqrt{s} = 8, 13, 14$ TeV [29].

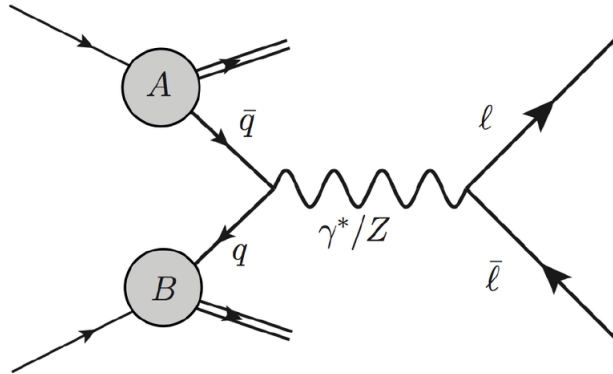


Figure 3.2: Drell-Yan process showing the production of a Z boson and its decay into two leptons [30].

γ^* . These particles are highly unstable and decays almost immediately into two leptons of opposite charges. A schematic diagram of a DY process at leading order is shown in Figure 3.2. From the momentum information of the outgoing leptons, the invariant mass of the DY mediator particle, M_{ll} , can be obtained [discussed in detail in section 7.3]. When the mediator is more likely to be a Z boson, the M_{ll} distribution exhibits a peak known as the Z resonance. Experiments have been studying the particle over the past three decades and till date, the most precisely measured value of the mass of the Z boson is $m_Z = 91.1876 \pm 0.0021$ GeV [7] and the decay width is $\Gamma_Z = 2.4952 \pm 0.0023$ GeV [7].

A tree-level diagram, like Figure 3.2, is too simple and uncluttered to be linked to the LHC collision environment. In fact, the interactions are rather complicated with higher order loops and radiation processes. A few of the higher order QCD corrections to the Drell-Yan process are shown in Figure 3.3. The total production cross-section of the Z boson is obtained by summing up all the possible Feynman diagrams. But the contributions of the higher order terms after NLO to the total cross-section become relatively insignificant as one

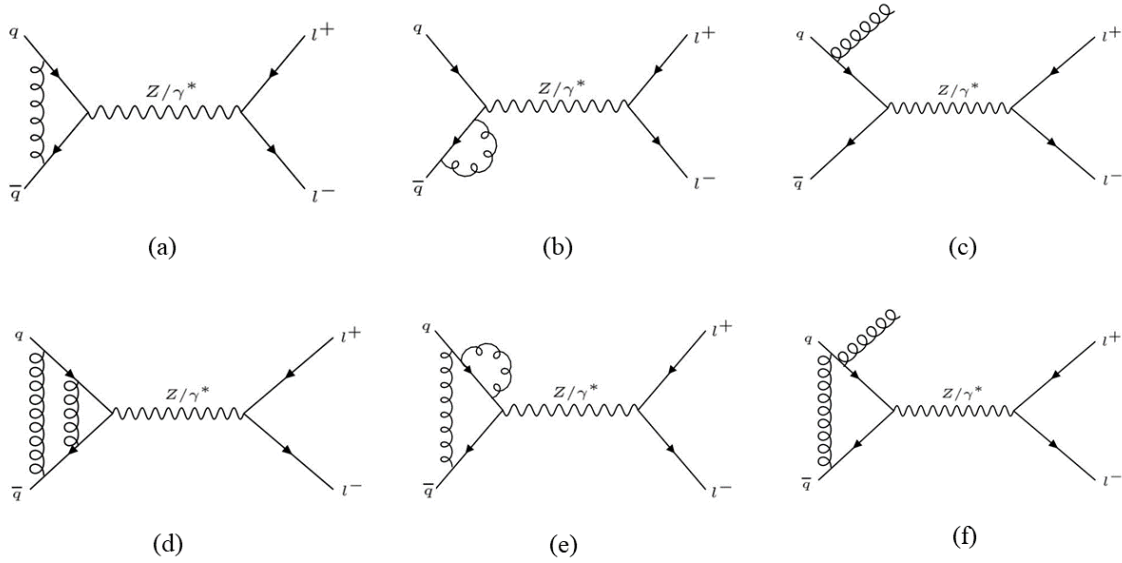


Figure 3.3: Some Feynman diagrams for the higher order QCD corrections to the Drell-Yan process are given. Diagrams (a)-(c) are at NLO and (d)-(f) are at NNLO.

can see from Figure 3.4 and can thus be neglected in this analysis.

After DY, the dominant mechanism for Z production is in association with a vector boson. The Z bosons are produced along with quarks and gluons as well. Figure 3.5 shows some such Z production mechanisms at the LHC. One must keep in mind that the quarks and gluons cannot be observed naked as they obey a QCD property known as *color confinement*, whereby color charged particles cannot exist isolated. Therefore, the quarks and gluons produced in association with the Z particle almost immediately hadronize to form a shower of stable colorless particles known as a *jet*, which is the final state detector observable for color charged particles.

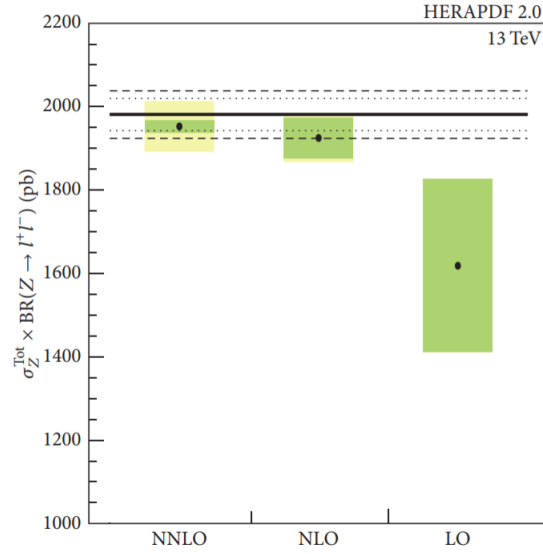


Figure 3.4: A summary of the production cross-section of the Z boson in the leptonic channel at LO, NLO and NNLO [31].

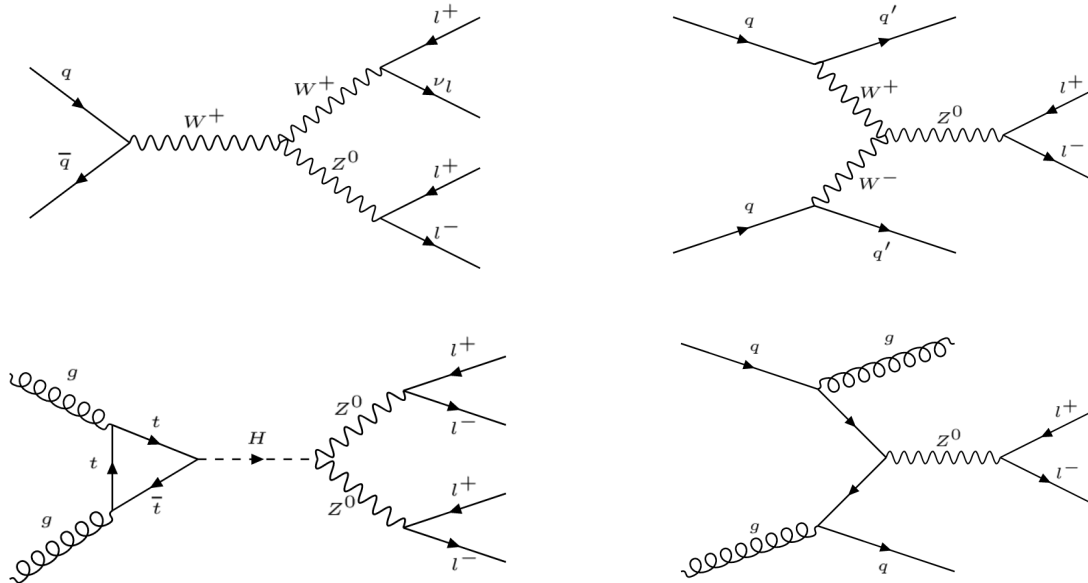


Figure 3.5: Feynman diagrams showing some of the Z production mechanisms at the LHC. The participating partons from the incoming protons can be a $q\bar{q}$, qg , $\bar{q}g$ or gg pair.

The material presented above in this section briefly describes some of the production mechanisms of the Z boson at the LHC. Before proceeding to the physics modeling techniques, it is essential to understand the decay channels of the Z as well. An important term useful to identify the favored decay channels of a particle is its branching ratio, denoted by BR . The branching ratios for the different decay channels of the Z boson are summarized in Table 3.1. It gives the probability of the Z particle to decay to a particular final state. In this thesis, Z production and its decay via the e^+e^- channel is studied. Even though the branching ratio of this process is fairly small, the e^+e^- channel leaves a relatively clean signature in the detector, which allows the process to be measured with a higher accuracy.

Decay Mode	Branching Ratio (%)
e^+e^-	3.363 ± 0.004
$\mu^+\mu^-$	3.366 ± 0.007
$\tau^+\tau^-$	3.370 ± 0.008
$\nu\bar{\nu}$	20.00 ± 0.06
hadrons	69.91 ± 0.06

Table 3.1: Branching ratios of the different decay modes of the Z boson [7].

3.2 Monte Carlo Event Generators

To study and understand a physics process, theoretical predictions are crucial. The theoretical prediction of any physics process is modeled using Monte Carlo (MC) techniques which serve as pivotal tools in high energy physics. The goal is to generate a sample of simulated events that follow a given theoretical model and all of its constraints, in a way that,

the probability of generating such a simulated event matches with the probability of occurring of an analogous actual event in nature. To achieve this, the MC method uses random numbers to simulate the event-to-event deviations to preserve the intrinsic probabilistic nature of the physics processes at the quantum level. To mimic the proton-proton collisions at the LHC and its aftermath, Monte Carlo event generators are used, which are software libraries employed to generate events based on MC methods. The generation of a proton-proton collision event [recall a typical collision event from Figure 2.4] is built on the following components [32]:

1. Hard process
2. Parton shower (radiation from partons)
3. Multiple interactions and beam remnants
4. Hadronization
5. Decays of unstable hadrons

POWHEG [33] is the generator used in this analysis to model the Z boson production and its decay into two electrons of opposite charges. POWHEG is a next-to-leading order generator which generates the hard process at NLO. The output from POWHEG is interfaced with a multipurpose parton showering and hadronization generator called PYTHIA 8 [34]. The final state particles generated are then subjected to a GEANT4 based software [35] to simulate the response of the different components of the ATLAS detector. At this step, the Monte Carlo sample can be compared with the collision data recorded by the detector. Further details on event generators and simulation software can be found in [33–35]. The MC sample used in this analysis is *mc15_13TeV.361106.PowhegPythia8EvtGen_AZNLOCTEQ6*

$L1_Zee.merge.DAOD_STDM3.e3601_s2576_s2132_r7725_r7676_p2952$ ¹ and is generated using the *CTEQ6L1* PDF set with the *AZNLO* tune following the *STDM3* derivation.²

$\underbrace{mc15_13TeV}_{Project\ name} . \underbrace{361106}_{Dataset\ identifier} . \underbrace{PowhegPythia8EvtGen}_{Event\ generators} . \underbrace{AZNLO}_{tune} \underbrace{CTEQ6L1}_{PDF\ set} - \underbrace{Zee}_{Physics\ process} . \underbrace{merge.DAOD}_{Data\ format} - \underbrace{STDM3}_{Derivation\ flavor} .$
 $\underbrace{e3601_s2576_s2132_r7725_r7676_p2952}_{Production\ tags}$

²*STDM3* derivation is an intermediate data format with appropriate trigger based selections. The ATLAS trigger system is explained in Section 5.4.

Chapter 4

The Large Hadron Collider

4.1 Introduction

Particle accelerators and colliders are the fundamental tools for probing the sub-structure of particles and they have always kept the scientific community on a cliffhanger because of the revolutionary changes they bring to the field of particle physics. They provide incredibly large amounts of energy making possible our access to distances as small as 10^{-20} m. The underlying physics relating momentum, p (or energy) and wavelength, λ , is originally given by de Broglie according to $\lambda = h/p$, where h is the Planck's constant. Therefore, larger momentum (or energy) corresponds to smaller wavelength or distance probed which serves as the motivation for "*high energy*" experiments.

The highest energies, at present, are generated at the CERN's accelerator complex by the Large Hadron Collider (LHC). The LHC is the world's largest and the most complex and powerful particle accelerator. It is situated in a 27 km circular tunnel, 100 m underground

at CERN near Geneva, Switzerland. Operational in 2008, it is the present final element in the accelerator complex at CERN. The LHC accelerates charged hadrons, mainly protons and Pb ions, and collides them head-on at various points along the ring where detectors are housed to record the collisions. This thesis focuses only on the proton-proton collisions taking place at one of the interaction points, located inside the ATLAS detector.

4.2 Accelerator Complex at CERN

CERN's accelerator complex is a sequence of machines which raises the energy of the particles before injecting them into the next machine in the chain. The entire accelerator framework is shown in Figure 4.1. The protons for collision are extracted from a small bottle of hydrogen gas from which electrons are stripped off under strong electric fields. The protons are then accelerated by LINAC 2, the first in the chain, to an energy of 50 MeV, followed by the Proton Synchrotron Booster (PBS) and the Proton Synchrotron (PS) which raise the energy to 25 GeV. The next in line is the Super Proton Synchrotron (SPS) which delivers an energy of 450 GeV before injecting the beam to the LHC. The LHC splits the beam into two and circulates them in two separate rings in opposite directions, taking each beam to a record energy of 6.5 TeV before colliding them in the ATLAS detector at a center of mass energy of 13 TeV.

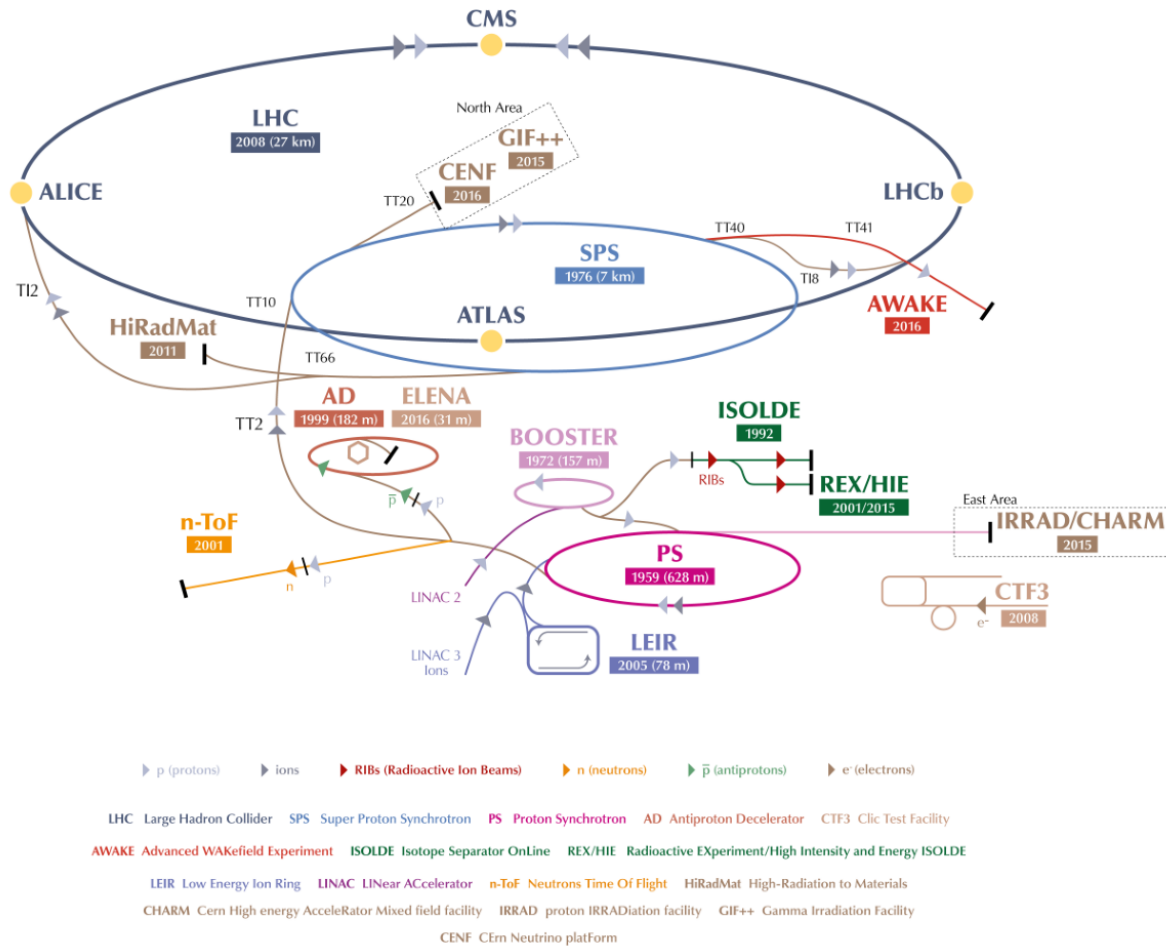


Figure 4.1: CERN Accelerator Complex [36].

4.3 Vacuum System

The performance and reliability of the LHC falls considerably if the protons in the beam pipe get a chance to interact with even some electrons from gas molecules. To operate the LHC in its full potential, it is essential to ensure a clean environment for the circulating pro-

tons. This is achieved by installing ultrahigh vacuum systems rendering a vacuum pressure of nearly 10^{-7} Pa in the beam pipe and less than 10^{-9} Pa at the collision point.

4.4 Magnetic System and Cryogenics

The magnetic system at the LHC is designed to maintain narrow, focused proton beams in circular tracks. To serve this purpose, the LHC employs magnetic dipoles and multipoles. The beam is guided in circular paths by the magnetic dipoles whereas, focusing the beam is achieved by the magnetic multipoles.

Nearly 1232 magnetic dipoles are stationed inside the collider to curve the beam. The dipole generates a magnetic field of 8 T in opposite vertical directions on the two beam pipes. Because the two proton beams travel in opposing directions inside the respective pipes, this causes the Lorentz force acting on the beams to be in the same direction, i.e. towards the center of the ring, thus maintaining the beam trajectory. This is illustrated in Figure 4.2.

Focusing the proton beams is achieved by about 400 quadrupole magnets such that the beams remain within the vacuum chamber. The quadrupole magnets work in pairs to focus the beam in two directions, one constricts the beam width and the other constricts the beam height, and deliver a narrow, focused beam. Figure 4.3 represents how the quadrupole magnets work in tandem to focus the beam. The beams are further squeezed before they collide inside the detector. Additional beam focusing and corrections are facilitated by magnetic multipoles, as described in detail in [38, 39].

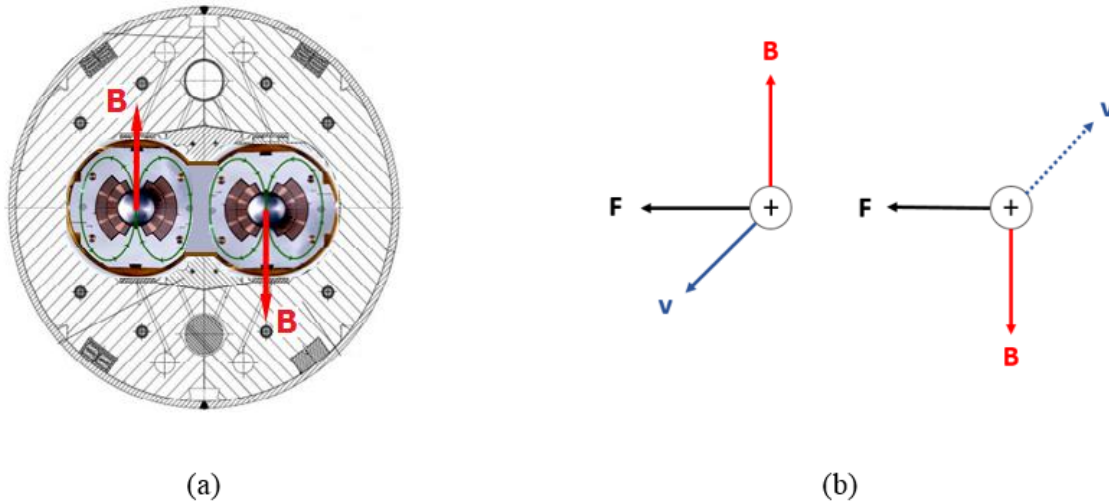


Figure 4.2: A cross-section of the LHC dipole showing the directions of the magnetic field acting the two beam pipes is given in (a). (b) shows the directions of the magnetic field, the proton beams and the Lorentz force acting on the beams. It is evident that the force acting on the two beams is in the same direction, thus curving both the beams in that direction [37].

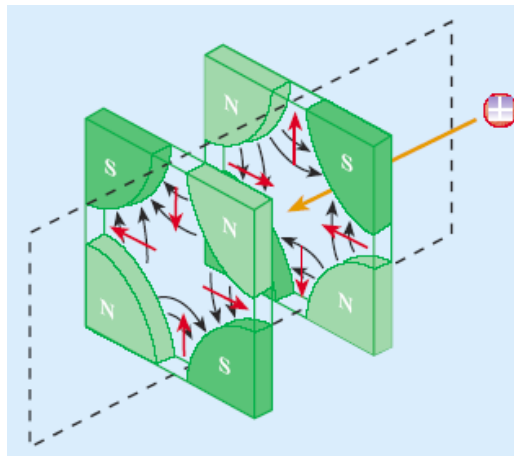


Figure 4.3: A graphic representation of the directions of the proton beam, the magnetic field and the Lorentz force is given. The yellow line shows the beam direction, the black lines show the magnetic field directions and the red lines show the magnetic force directions [40].

The magnets at the LHC are superconducting electromagnets. These electromagnets use a current of about 11,080 A to produce the intense magnetic fields required to keep the proton beams on track. Their coils enter a superconducting state under very low temperatures (nearly 2 K) and offer no resistance to the conduction of electric current, thus saving energy from being lost to electrical resistance. To cool the magnets and to preserve the cryogenic temperatures, the LHC tunnel is installed with a second ring of the same length called the *cryogenic ring* filled with liquid helium at 1.9 K. Liquid helium takes the heat away from the collider and maintains its operating temperature. Also, at this low temperatures, liquid helium exhibits *superfluid* property of remarkably high thermal conductivity which makes it excellent for the purpose.

4.5 Proton Bunching

Protons in their journey within the accelerator complex are grouped into *bunches* and a series of radio frequency cavities are used to accelerate the bunches. Each bunch in the LHC has nearly 10^{11} protons and each beam, at its full intensity, has 2808 bunches in it with a spacing of 25 ns in between. Collisions take place when two bunches from the opposite beams inter-penetrate which is termed as a *bunch crossing*. In the ATLAS detector, there are 40 million bunch crossings per second [41] but the probability of a proton in one bunch hitting another proton in the opposite bunch is very small and most protons miss each other. In the 2016 collision data, analyzed in this thesis, there occurs on average 25 proton-proton inelastic interactions for every bunch crossing. The collisions that occur in addition to an interesting collision in every bunch crossing is termed as *pile-up* (PU). In other words, it is the total number of interactions per bunch crossing and it represents the major background in the

detectors for any physics analysis. Figure 4.4 gives a summary of the pile-up interactions recorded by ATLAS in the recent years.

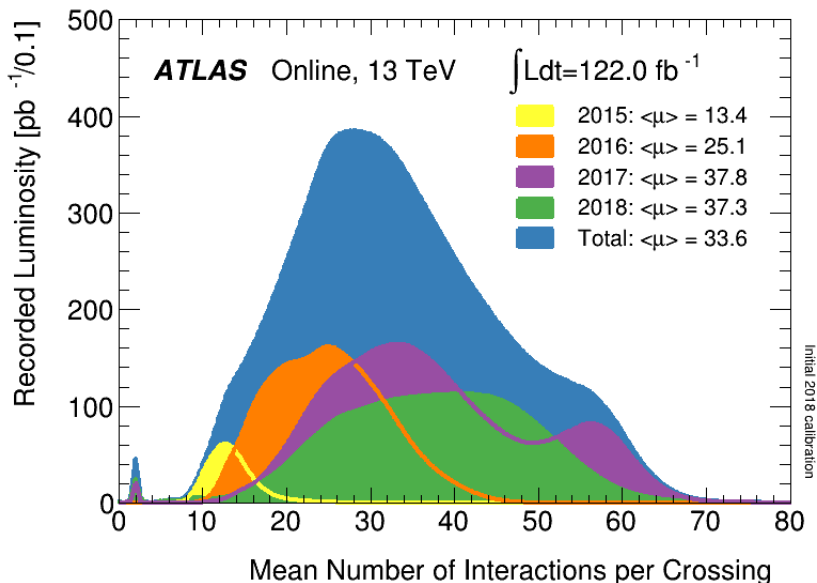


Figure 4.4: The number of pile-up interactions in the ATLAS detector in Run 2 [from 2015-2018] [42].

4.6 Luminosity

One of the important parameters used to assess the machine performance is called the luminosity. This parameter is expressed in two ways as described below.

4.6.1 Instantaneous Luminosity

The instantaneous luminosity, L , evaluates the rate at which collisions happen in the detector. It is a measure of the number of collisions produced per cm^2 per second and is

calculated as,

$$L = \frac{fN_1N_2}{4\pi\sigma_x\sigma_y}. \quad (4.1)$$

Here, f is the frequency of bunch crossing, N_1 and N_2 are the number of protons in the two colliding bunches, σ_x and σ_y are the horizontal and vertical components respectively of the geometric cross-section of the bunch at the interaction point. σ is rather the effective cross-section as the beam profile does not have a sharp edge.¹ Instantaneous luminosity is related to the rate at which any physics process can occur in the detector. If a physics process has a production cross-section σ , then the rate of production R of such a process is $R = L\sigma$. Considering the peak luminosity of $13.8 \text{ nb}^{-1}\text{s}^{-1}$ delivered to ATLAS in 2016, nearly 26 Z bosons are produced every second!

4.6.2 Integrated Luminosity

A more interesting term useful for physics analysis is the integrated luminosity \mathcal{L} , which is the instantaneous luminosity integrated over a period t defined as:

$$\mathcal{L} = \int_0^t L dt. \quad (4.2)$$

It determines the number of events produced in a given data taking period. For a physics process of cross-section σ , the total number of events produced is $N_{events} = \mathcal{L}\sigma$.

¹The beam is assumed to have a Gaussian shape in first approximation.

Chapter 5

The ATLAS Experiment

5.1 Introduction

The ATLAS (A Toroidal LHC ApparatuS) experiment [43–46] is one of the four main experiments at the LHC. Together with CMS [47], it serves as a general purpose detector, operating at the LHC’s highest luminosity conditions with a goal to record as many interesting physics events as possible. The detector is a long cylindrical barrel, sandwiched between two end-cap regions, having an overall length of 45 m and a diameter of 25 m. It is the largest detector in volume ever built for particle detection. The detector has four major components:

1. The Inner Detector
2. The Calorimeter
3. The Muon Spectrometer
4. The Magnet System

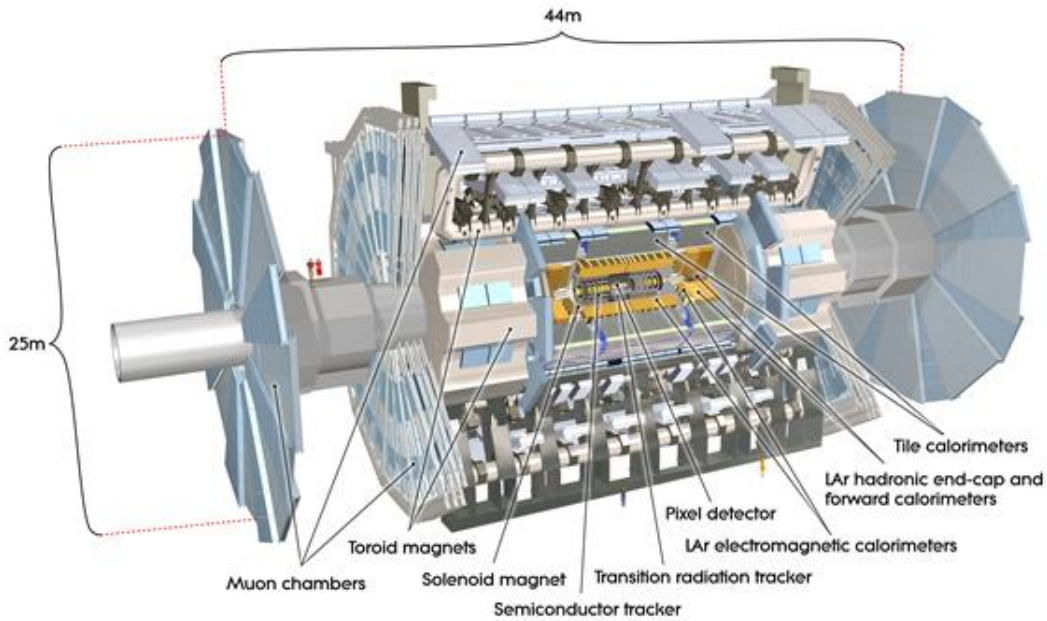


Figure 5.1: The ATLAS detector [48].

These sub-detectors are stacked onto each other in a concentric fashion around the collision point, along the beam axis. A schematic of the longitudinal view of the detector is shown in Figure 5.1.

5.2 Coordinate System

The ATLAS detector uses a right-handed Cartesian coordinate system, see Figure 5.2. The nominal interaction point is taken as the origin with the $+x$ -axis pointing to the center of the LHC ring, the $+y$ -axis pointing upwards, and the $+z$ -axis along the beam line. The $x-y$ plane can be described equivalently using $r-\phi$ cylindrical coordinates. $r = \sqrt{x^2 + y^2}$ gives the displacement from the beam axis in the transverse plane (or the $x-y$ plane), and the

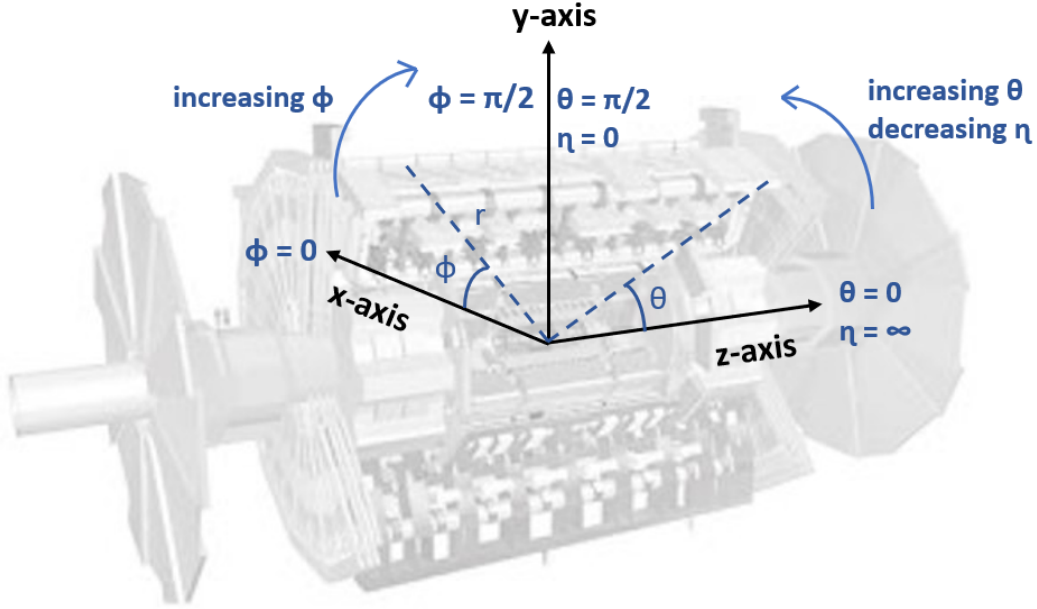


Figure 5.2: The ATLAS coordinate system. Base image taken from [48].

azimuthal angle ϕ , measured anti-clockwise from the $+x$ -axis, gives the hermetic coverage around the beam axis. The angle from the $+z$ -axis in the $y - z$ plane is described by the polar angle denoted by θ . In the collider environment, the laboratory frame is longitudinally Lorentz boosted as the relativistic incoming particles move along the z direction, but a difference in θ is not Lorentz invariant in the z direction. This makes the polar angle a less preferred variable as the momenta of the incoming particles differ from event to event. For this reason, the commonly used quantity is the pseudorapidity, η defined as,

$$\eta = -\ln \tan \left(\frac{\theta}{2} \right) = \frac{1}{2} \ln \left(\frac{|\vec{p}| + p_z}{|\vec{p}| - p_z} \right) \quad (5.1)$$

where \vec{p} is the total three-vector momentum and p_z is the longitudinal momentum component of the particle. Pseudorapidity is used for massless particles, in relativistic cases where mass

of the particle can be neglected or when the particle identity is unknown. For heavily massive particles like the Z boson, a more interesting quantity is the rapidity, y ,

$$y = \frac{1}{2} \ln \left(\frac{E + p_z}{E - p_z} \right) \quad (5.2)$$

which takes into account the total energy, E , when the particle mass is significant. A difference in η and y in the longitudinal direction is relativistically invariant which makes them the preferred geometric parameters used to describe the events [49].

5.3 Sub-Detector Systems

5.3.1 The Inner Detector

The Inner Detector (ID) is the first component of the multi-layered ATLAS detector, hence the layer closest to the beam pipe. It is 6.2 m long with a diameter of 2.1 m, and immersed in an axial magnetic field of 2 T. Due to the high number density of particles emerging from the collision point, the ID is designed to be highly sensitive to the particle influx. With high granularity, full ϕ coverage and $|\eta| < 2.5$, the ID precisely locates the interaction vertex and reconstructs the trajectories of charged particles. This task is accomplished by the three main sub-systems of the ID: the Pixel Detector (PD), the Semiconductor Tracker (SCT) and the Transition Radiation Tracker (TRT).

The Pixel Detector [50,51] is the first layer of the Inner Detector, consisting of 1,744 modules, each having 47,232 silicon pixels with an overall 46,080 readout channels¹ per module.

¹Certain pixels have common readout channels. This is why readout channels are lesser in number when compared to the silicon pixels.

When a particle deposits energy in a pixel, it is recorded as a *hit*. Each pixel has a size of $50 \times 400 \mu\text{m}^2$ in $\phi - z$, offering a spatial resolution of $10 \mu\text{m}$ in $r - \phi$ and $115 \mu\text{m}$ in z per hit in the barrel region. At the end-caps, the resolution is $10 \mu\text{m}$ in $r - \phi$ and $115 \mu\text{m}$ in r per hit. When the hits are combined, the *track* of the particle trajectory can be determined. From the track information, the intersecting point from which all the tracks emerge can be found, which is identified as the interaction *vertex*. The PD has been upgraded in 2014 to install an additional layer called the insertable B-layer (IBL) which is now the closest layer to the beam pipe [52]. The insertion of this layer is to improve the tracking and the vertexing efficiencies which get challenging with increasing luminosity.

Surrounding the PD lies the silicon Semiconductor Tracker [53, 54] consisting of 4,088 two-sided modules arranged in 4 cylindrical layers in the barrel region and 9 planar discs on either side of the barrel, with more than 6 million readout strips. It offers a spatial resolution of $17 \mu\text{m}$ in $r - \phi$ and $580 \mu\text{m}$ in z (in r) in the barrel (at the end-cap) for a single hit.

The next layer encircling the SCT is the Transition Radiation Tracker [55, 56]. It consists of straw drift tubes with transition radiation material embedded in between. There are 50,000 straw tubes in the barrel and 250,000 in the end-cap regions with over 351,000 readout channels. The TRT can only render the $r - \phi$ information and not the z . Each straw in the TRT provides a precision of $130 \mu\text{m}$ for a hit. A typical track passes through 3 pixels, 4 SCT modules and 36 (or 22) straw tubes in the TRT's barrel (or end-cap) region.

5.3.2 The Calorimeter

The ATLAS calorimeter system is designed to perform a disruptive measurement of the total energy possessed by the incoming particles by bringing them to a halt. Depending on the type of interacting particles, the calorimeter system is classified as the Electromagnetic Calorimeter (ECal) and the Hadronic Calorimeter (HCal). The ECal measures most of the energy of photons and electrons that interact electromagnetically, while the HCal measures most of the energy of hadrons through their strong and electromagnetic interactions. Both the calorimeters are of *sampling* type in construction, with alternating layers of absorber and active materials. When an incoming particle interacts with the absorber material, a shower of secondary particles is generated and the energy deposited in the process is read out from the sampling layers. The measured signal along with the shower development profile provide an estimate of the energy of the incident particle.

The ECal [57] consists of a barrel and two end-cap calorimeters covering the region $|\eta| < 3.2$. It has an accordion geometry with liquid-argon read-out material interleaved with lead absorber plates. $1.37 < |\eta| < 1.52$ corresponds to the barrel/end-cap transition region and the calorimeter performance is not optimal in this region. The HCal consists of a barrel tile calorimeter and two hadronic end-cap calorimeters (HEC). The tile calorimeter [58] uses a steel absorber and an active scintillator medium covering an $|\eta| < 1.7$, while the HEC [59] is a copper/liquid-argon calorimeter located at $1.5 < |\eta| < 3.2$. To cover the forward regions, a liquid-argon based Forward Calorimeter (FCal) [60] is used. Located at $3.1 < |\eta| < 4.9$, the FCal is designed to be radiation hard² as it sits closer to the beam pipe. It consists of one electromagnetic and two hadronic layers. The electromagnetic FCal uses copper and the

²resistant to damage or malfunction due to high energy radiations

hadronic layers use tungsten as the absorbers. The ATLAS detector is also equipped with cryostats where the calorimeters are housed to maintain low operating temperatures.

The fractional energy resolution offered by the ATLAS calorimeter system is given by the formula:

$$\frac{\sigma(E)}{E} = \frac{a}{\sqrt{E}} \oplus \frac{b}{E} \oplus c, \quad (5.3)$$

where a is the stochastic term, b and c are the noise and the constant terms respectively. A summary of the energy resolution for different calorimeter layers is given in Table 5.1

Calorimeter system	Resolution
ECal	$\sigma_E/E = 10\%/\sqrt{E} \oplus 0.7\%$
HCal	$\sigma_E/E = 50\%/\sqrt{E} \oplus 3\%$
FCal (electromagnetic)	$\sigma_E/E = 28.5\%/\sqrt{E} \oplus 3.5\%$
FCal (hadronic)	$\sigma_E/E = 94\%/\sqrt{E} \oplus 7.5\%$

Table 5.1: The fractional energy resolution for the various calorimeter systems is given. Noise term is not considered here. The electromagnetic layers are tested using electron beams. The HCal and the hadronic FCal are studied using jets and pion beams respectively [46, 60].

5.3.3 The Muon Spectrometer

The Muon Spectrometer (MS) [61] is the outermost layer of the detector, surrounding the calorimeters. Muons are minimally ionizing and can easily pass through the calorimeters. The MS is placed the furthest to provide high resolution measurements of the position and the momentum of muons for $|\eta| < 2.7$. The MS is split into four sub-detector systems. The Monitored Drift Tubes (MDTs) and the Cathode Strip Chambers (CSCs) provide the track

and momentum measurements of high energy muons. The Resistive Plate Chambers (RPCs) and the Thin Gap Chambers (TGCs) are used as triggering systems.

5.3.4 The Magnet System

The detector has a superconducting magnet system with a central solenoid surrounded by eight large toroidal magnets [62] to bend the charged particles for momentum measurement. The central solenoid [63] provides a magnetic field of 2 T along the beam axis for the inner detector. The toroidal magnets are split as the barrel toroid (BT) [64] and two end-cap toroids (ECTs) [65]. The BT and the ECTs provide 0.5 T and 1 T respectively to the central and end-cap regions of the muon spectrometer. The entire magnet system is 26 m in length and 20 m in diameter, and is maintained at cryogenic temperatures.

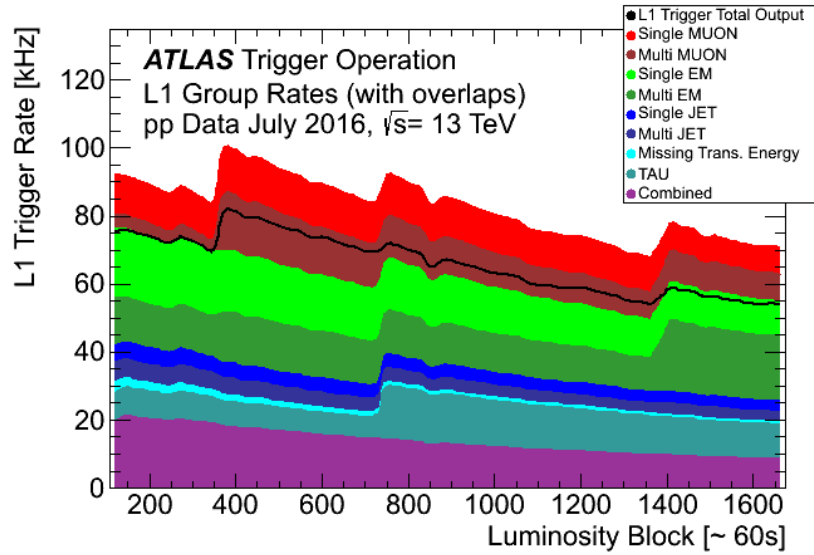
5.4 Trigger and Data Acquisition

The LHC delivers data at an astounding rate with millions of collisions per second but the number of “*interesting*” events produced are not at all comparable with this rate. In fact, only two Z bosons that decay into electrons are produced every second. Rare events like Higgs boson production occur only once every 10 seconds³ [66,67]. Since it is technically impossible to store all the collision data, ATLAS uses an extensive trigger system to save only the interesting events and rejects the rest [68]. This task is delegated between a hardware-based Level-1 (L1) trigger [69] and a software-based high-level trigger (HLT) [70]. The L1 trigger receives signal from the calorimeter and the muon detectors, selecting only objects⁴

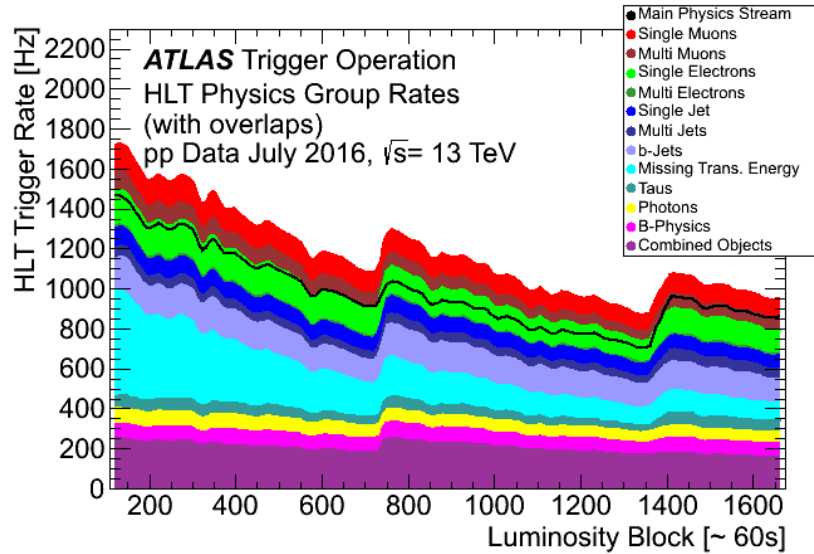
³The rates mentioned are predicted for a centre of mass energy of 14 TeV and a luminosity of $1 \text{ nb}^{-1}\text{s}^{-1}$.

⁴An object is any physically detectable quantity in the detector like an energy deposit in the calorimeter or a reconstructed track.

with differentiating characteristics, thus reducing the event rate from 40 MHz to 100 kHz. L1 trigger employs a generic object definition and the objects meeting the selection criteria fire the trigger. The events passing the L1 trigger are directed to the HLT, which analyzes the selected events in greater detail, reducing the rate further down to 1 kHz. This can be better understood from Figure 5.3, which summarizes the ATLAS trigger rates in an LHC fill taken in July 2016. The selected events are then passed onto the storage system for offline analysis. From the raw data, the particles and the various kinematic parameters are identified and the *reconstructed* data is used for physics analysis.



(a) Level 1 trigger rate.



(b) High-level trigger rate

Figure 5.3: The ATLAS trigger rates for the Main Physics Stream for an LHC fill is given. The L1 trigger rates are shown in (a). Events passing the L1 trigger are directed to the HLT which applies more stringent object definitions reducing the rate even further as given in (b). The sudden rises in the rates correspond to new triggers being enabled and the slow exponential falls are results of the decreasing luminosity during the fill [71].

Chapter 6

Electron Reconstruction

The primary goal of the analysis is to detect a Z boson which has decayed into a pair of electrons of opposite charges.¹ The Z boson has a known mean life time of 3×10^{-25} s restricting its range to less than a proton's radius. This is a consequence of the mass of the boson which makes it nearly a *zero-lived* particle. Hence, a direct detection is impossible. But, from the physically observable objects, electrons in this case, the Z boson can be reconstructed by working backwards. The motivation for choosing this channel is due to the relatively clean signature the electrons leave in the detector.

6.1 Electron Reconstruction

Electromagnetic cluster reconstruction

An electron is an electromagnetically interacting charged particle. Therefore, the signature for an electron event is a track in the inner detector, originating from its production

¹Hereafter in this thesis, the electron pair is collectively referred to as “*electrons*”

vertex and often terminating in the electromagnetic calorimeter, accompanied by an energy deposit in the latter. The ID covers $|\eta| < 2.5$ and the central region of the ATLAS detector is defined by $|\eta| < 2.47$. The analysis presented here takes into account only central electrons, therefore, only the calorimeter information at $|\eta| < 2.47$ is necessary for electron identification. The trigger decision at the L1 level for electromagnetic showers in the calorimeter is made by the L1 Calorimeter (L1_Calo) trigger. Electron and photon objects are identified by the L1_EM trigger, one of the components of L1_Calo using a sliding window algorithm. The algorithm searches for clusters of size $\Delta\eta \times \Delta\phi = 0.025 \times 0.025$ with a total transverse energy deposit above 2.5 GeV. Once the cluster is located, the trigger is fired [72].

Track reconstruction

The next step in the reconstruction procedure is to tag the track of an electron as it traverses the inner detector material. One can recall the number of hits a charged particle must leave in the inner detector for a track to be reconstructed from Section 5.3.1. An electron candidate is identified by matching the electromagnetic cluster with a well aligned track in the inner detector which distinguishes it from a photon. Since a photon is electrically neutral, it leaves no trace of its trajectory in the inner detector. However, the numerous tracks left behind by charged pions make the identification of electron tracks a difficult task. A pion suffers from minimal energy loss, while a high energy electron undergoes significant energy loss due to Bremsstrahlung. Studying the energy loss patterns associated with the tracks is a useful tool to recover the electron tracks. ATLAS uses a series of track fitting algorithms to identify the electron tracks including the Kalman Filter, the Global χ^2 Track Fitter and the Gaussian Sum Filter, described in detail respectively in [73–75]. Once the electron track is identified and correctly matched with the associated cluster in

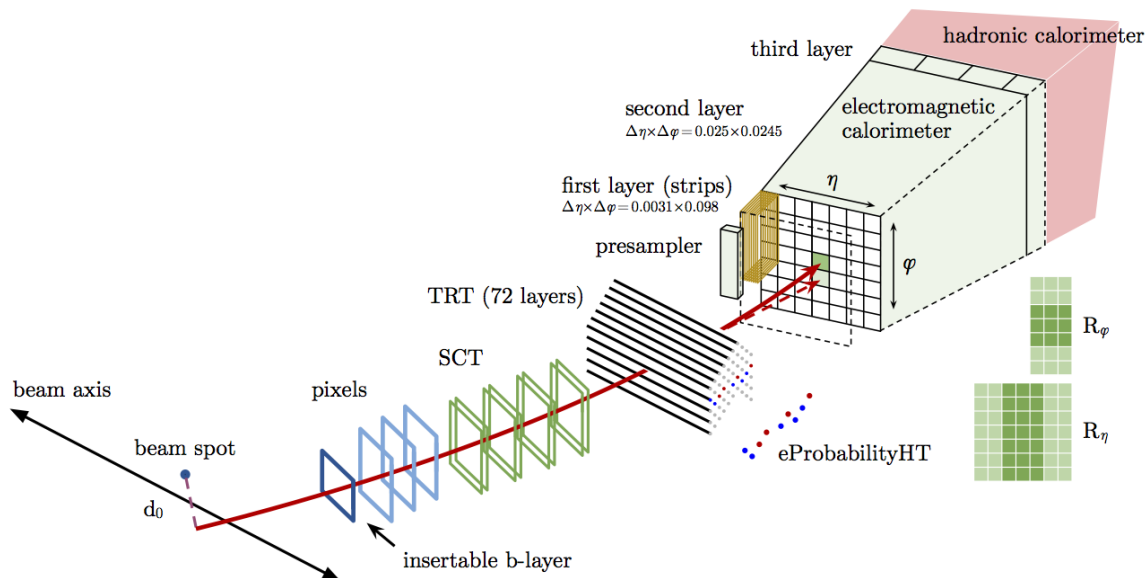


Figure 6.1: A schematic of the electron reconstructed in the ATLAS detector is shown. The hits on the inner detector layers are connected to trace the trajectory of the electron which is then matched with a corresponding energy deposit in the electromagnetic calorimeter [76].

the electromagnetic calorimeter, the electron reconstruction is complete. The combined information from the cluster and the track is used to evaluate the momentum of the electron. The charge on the electron is determined from the direction of the radius of curvature of the track under the magnetic field in the inner detector. Figure 6.1 shows a schematic of the reconstructed electron in the ATLAS detector.

6.2 Electron Background

After reconstruction, the next step is to carefully identify the electrons of interest to the physics process under study. To separate the signal electrons from the background, a thorough understanding of all the particles and the processes that can mimic an electron

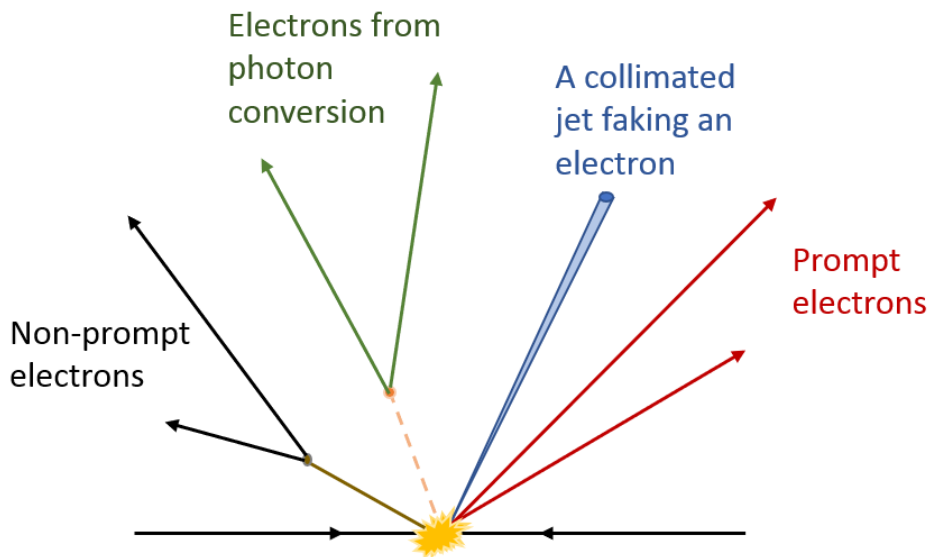


Figure 6.2: A representation of prompt signal and background electron events is given.

signature is crucial.

The reconstructed electrons can be categorized as *prompt* and *non-prompt* electrons. Prompt electrons are produced directly in a hard scatter from Higgs or weak gauge bosons, which have a very short lifetime. As a result, production vertex of prompt electrons are at the primary interaction vertex.² On the other hand, non-prompt electrons emerge from a vertex that is displaced from the primary interaction vertex of the hard scatter. One of the principal contributors to non-prompt electron background is jets, especially the heavy flavour jets which have relatively longer lifetimes. The $\pi^0 \rightarrow e^+ + e^- + \gamma$ Dalitz decay and photon conversion $\gamma \rightarrow e^+ + e^-$ also contribute significantly to the production of non-prompt

²An interaction vertex is chosen as the primary vertex (PV) in an event if the vertex has at least two associated tracks in the ID, each with a transverse momentum $p_T > 400\text{MeV}$. If there is more than one such vertex, then the vertex which contribute to the highest track Σp_T^2 is selected. The identification of a primary vertex from pile-up vertices and its reconstruction procedure in detail can be found in [77].

electrons. A graphic illustration of prompt and non-prompt electrons is shown in Figure 6.2.

To reject the non-prompt electron background, two important tracking parameters are used: transverse impact parameter (d_0) and longitudinal impact parameter (z_0). d_0 is defined as the distance of the closest approach of the particle's track from the primary vertex in the transverse plane and z_0 is the distance in the z – direction between the primary vertex and the point at which d_0 is defined. Figure 6.3 explains how the impact parameters are defined in ATLAS. In simpler terms, d_0 can determine the minimum displacement of a track in the transverse plane while $|z_0 \sin \theta|$, where θ is the polar angle of the track, can evaluate the same displacement in the longitudinal plane. Distributions of d_0 and $|z_0 \sin \theta|$ for non-prompt leptons will exhibit long tails as they originate from displaced vertices, and can be used to veto events.

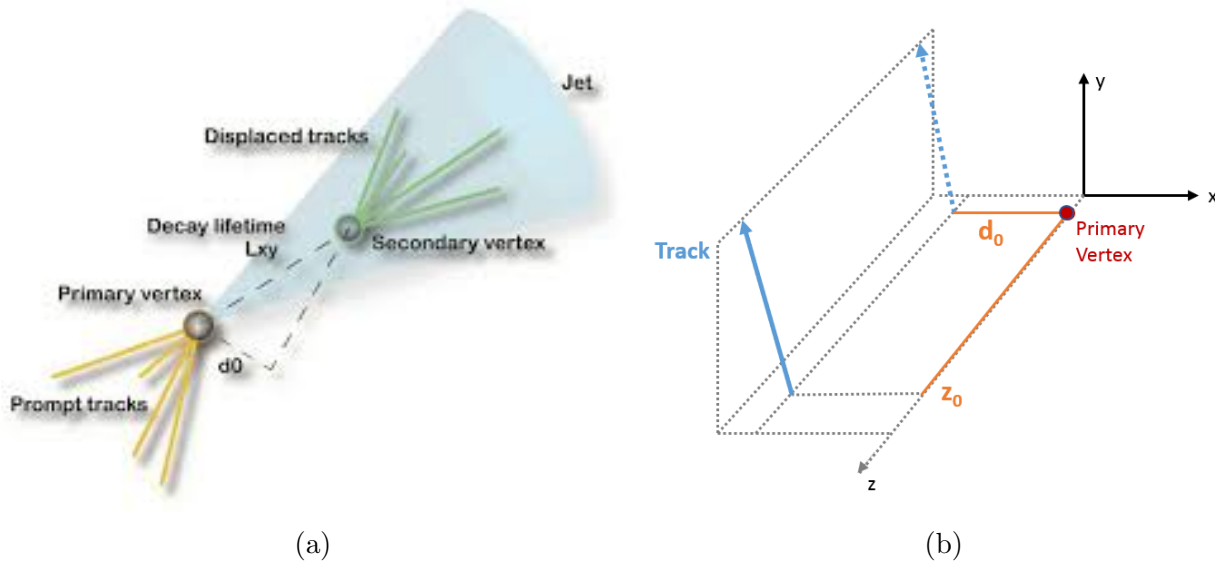


Figure 6.3: Definitions of the impact parameters, d_0 and z_0 are shown [78].

In addition to the non-prompt electron background, the signature of prompt electrons are sometimes imitated by some highly collimated jets. With the calorimeter level information, one can distinguish an electron from a jet. A jet generates a hadronic shower which interacts both with the electromagnetic and the hadronic calorimeters, while the electron's shower typically does not leak much into the hadronic calorimeter. Moreover, one can identify a jet from its wide showering pattern in the hadronic calorimeter compared to a narrow shower generated by an electron in the electromagnetic calorimeter.

6.3 Electron Identification

ATLAS employs dedicated identification algorithms to determine whether the reconstructed electron is signal-like or background-like. The algorithms use the principle of likelihood-ratio test based on Neyman-Pearson Lemma [79], which rejects the null hypothesis with the greatest statistical power when the alternate hypothesis is true. In other words, the likelihood-based (LH) method evaluates an overall probability for the electron to be signal-like or background-like by considering various properties of the electron, and identifies an *operating point* with a better background rejection. Several operating points (LOOSE, MEDIUM, TIGHT) are provided based on the increasing order of background rejection. Each operating point uses the same set of variables for electron identification but the requirements become rigorous with increasing *tightness* of the operating point. An electron passing the MEDIUM likelihood-based identification selection will certainly pass the LOOSE selection, but may or may not pass the TIGHT. Strictly speaking, an electron in a tight menu will be a subset of a less tight menu, and the data quality or signal to background efficiency, improves with increasing tightness. A clear example of how one of

the discriminants, used in LH based electron identification selections, cuts events for various operating points is given in Figure 6.4.

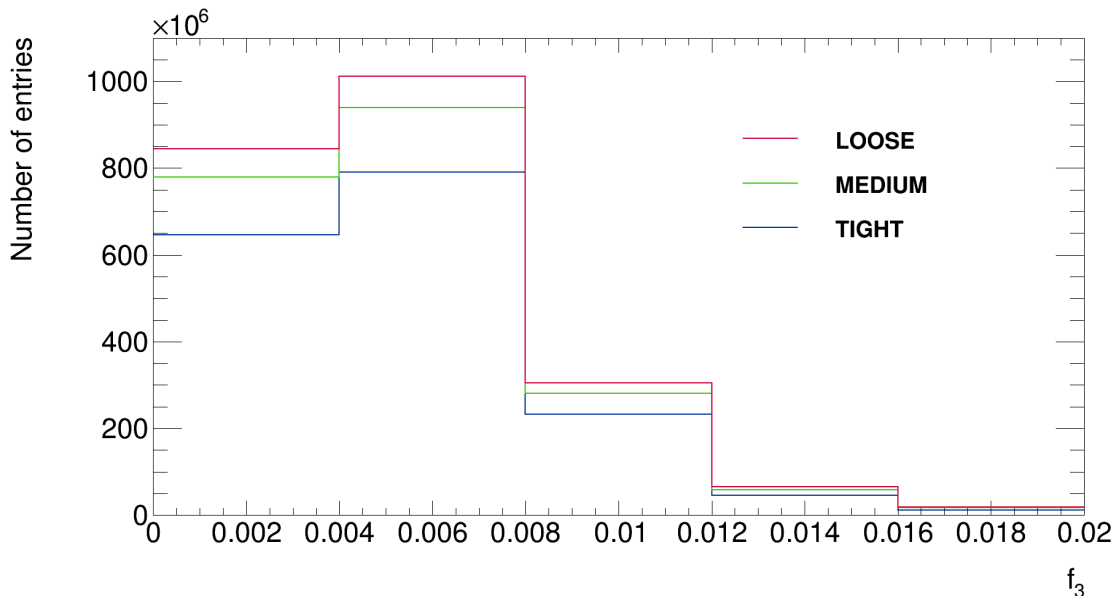


Figure 6.4: An electron LH discriminant variable, f_3 , is plotted for the operating points, LOOSE, MEDIUM, and TIGHT. f_3 gives the ratio of the energy deposited in the back layer to the total energy deposited by an electron in the electromagnetic calorimeter.

6.4 Electron Isolation

To facilitate further background rejection and to separate the electron signal, isolation variables are used at the track and at the calorimeter levels. In track-based isolation, a cone of ΔR is defined around the electron in the inner detector. If the scalar sum of the transverse momentum of all the tracks,³ that satisfy some track quality cuts and fall within ΔR , exceeds a threshold of 0.4 GeV, then the electron is considered to pass the isolation requirement at the track level. In calorimeter-based isolation, a similar approach is followed,

³excluding the electron track

but ΔR is defined in the calorimeter cells and a threshold cut is placed on the transverse energy deposit in the calorimeter [80].

The above mentioned procedures of reconstruction, identification and isolation are the precursory steps in selecting the electrons for reconstructing a Z boson. To reconstruct the Z particle, more stringent conditions are to be met. The next chapter elucidates all the requirements an event must satisfy in order to qualify as containing a Z signal.

Chapter 7

Event Selection and Signal Extraction

To extract the signal of interest from the collision data and reduce background, a set of criteria must be satisfied. The selection criteria are applied at the event level and at the object level. This chapter focuses on the selection cuts employed to reconstruct a Z boson from electrons, based on the procedure followed by ATLAS as detailed in [81]. The dataset used in this analysis is *data16_13TeV.periodL.physics_Main.PhysCont.DAOD_STDM3.grp16_v01_p2950*,¹ which belongs to *Period L* taken for *Physics Main Stream* runs² in October 2016.

7.1 Selection Criteria

Preliminary ATLAS selections

- The event must pass the derivation for *STDM3* [refer to Section 3.2].

¹ $\overbrace{data16_13TeV}^{\text{Project name}} \cdot \underbrace{periodL}_{\substack{\text{Data taking} \\ \text{period}}} \cdot \underbrace{physics_Main}_{\text{Stream name}} \cdot \underbrace{PhysCont}_{\substack{\text{Container} \\ \text{type}}} \cdot \underbrace{DAOD}_{\substack{\text{Data} \\ \text{format}}} \cdot \underbrace{STDM3}_{\substack{\text{Derivation} \\ \text{flavor}}} \cdot \underbrace{grp16_v01_p2950}_{\text{Tags}}$

²A run is a unit of data taking, from the injection of the beam until the beam is dumped in preparation for the next injection.

- The event must pass the *HLT_2e17_lhvloose_nod0* high-level trigger definition which chooses events with at least two electrons,³ each with a threshold transverse energy of 17 GeV, passing the data quality criteria for the operating point VERY LOOSE, with no cut on d_0 .
- The event must belong to a run that meets the ATLAS standards of data quality, e.g, all the sub-detector systems and trigger are operational, in stable beam conditions.
- The event must pass additional detector flags, which reject incomplete events as well as bad events due to detector imperfections.
- The event must have at least one primary vertex.

These are some generic selection cuts on events that make the data suitable for use by various ATLAS groups. Additional cuts, specific to the analysis described in this thesis, are stated as follows.

Analysis-specific selections

Event-level selections:

- The event must contain exactly two electrons. All other events are rejected.

Note: Events having at least two electrons have been studied as well and only a 0.3% increase in the number of events has been observed. Due to the statistical limitation in combinatorial background estimations, only two electrons events are analyzed.

³objects passing the electron reconstruction criteria as mentioned in Section 6.1 without any selection cut on the electric charges.

Object-level selections:

- The electrons must be *trigger-matched*, which means that the offline electrons match with the online triggered electrons.
- Both the electrons in the selected events must satisfy the data quality criteria for MEDIUM operating point [refer to Section 6.3].
- The electrons must pass isolation cuts as described in Section 6.4.
- The electrons must possess opposite signs of unit electric charge.
- The electrons must be in the central region of the detector falling within $|\eta| < 2.47$.
- The electrons must have a minimum p_T of 25 GeV.

Statistics are presented later in Table 7.1. Before proceeding to reconstructing a Z boson, one must have a comprehensive understanding of the electrons used for the purpose and their distribution in the detector. This is described in the following section.

7.2 Electron Distribution

Geometric distribution

This thesis uses only electrons falling in the central region of the detector [see Section 6.1], which is $|\eta| < 2.47$, according to ATLAS definition.⁴ As both the inner detector and the electromagnetic calorimeter offer full ϕ coverage, no cut is applied on the azimuthal angle. Figure 7.1 gives the η and the ϕ distributions of the selected electrons in the detector.

⁴ $\eta = 2.47$ corresponds to a polar angle of 9.7° from the beam axis.

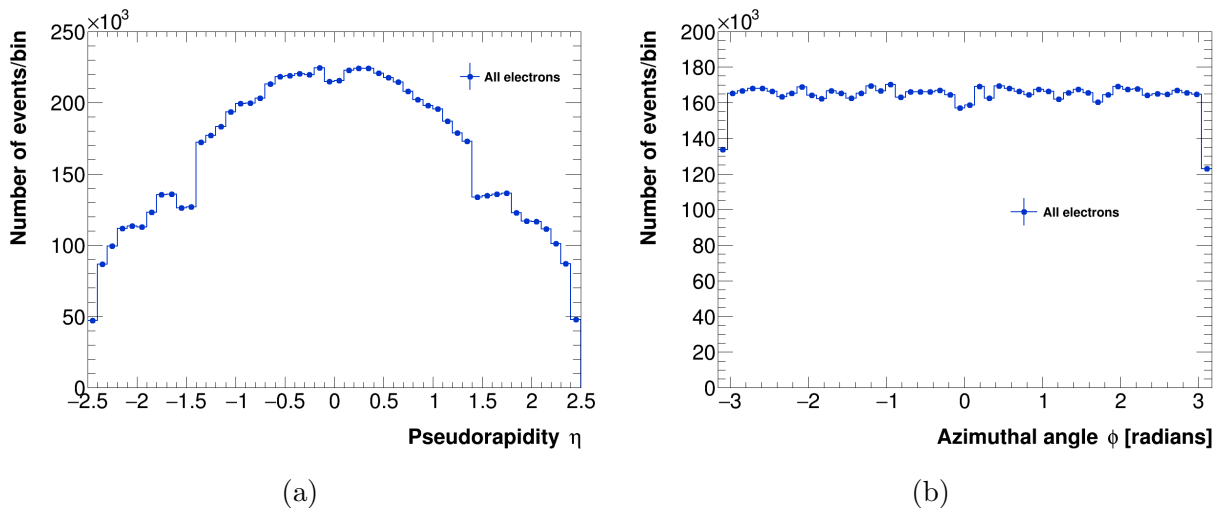


Figure 7.1: The η and the ϕ distributions of the selected electrons in the central region of the detector are given respectively in (a) and (b). From (a), it is clear that most of the electrons are produced transversely and the distribution falls with increasing $|\eta|$. The abrupt drop in the number of events in $1.37 < |\eta| < 1.52$ is due to the poorer calorimeter performance in the barrel/end-cap transition region. (b) presents a flat distribution of electrons in ϕ . The drop at the extreme ends is a result of binning.

Kinematic distribution

The electron kinematics are studied from its transverse energy, E_T . Due to its negligible mass, the transverse momentum of the particle, p_T , is taken to be same as its E_T . Hereafter, p_T is the used kinematic variable to refer to E_T as well.

The HLT used in this analysis is fired only for di-electron events, where both the electrons have a minimum p_T of 17 GeV. The electron with the higher p_T of the two is called the *leading* electron and the other is called the *sub-leading* electron. As the quality of the data depends totally on the trigger system, it is crucial to understand how efficient the trigger in use is. The trigger efficiency is usually defined with respect to the objects reconstructed offline,

according to Equation 7.1,

$$\epsilon_{trigger} = \frac{N_{trigger}}{N_{offline}}. \quad (7.1)$$

Here, $N_{trigger}$ is the number of events that pass the HLT and the offline reconstruction, for a threshold electron p_T of 17 GeV, in the MEDIUM operating point. $N_{offline}$ is the number of events that pass the offline reconstruction, for the electron threshold p_T at the same operating point. An ideal trigger would give a step function at the threshold p_T with a plateau [or region of maximal efficiency] at an efficiency of one but in reality, the trigger slowly *turns on* as a function of p_T . This can be seen from Figure 7.2a, which plots the trigger efficiency as a function of the sub-leading electron p_T . One can see from the figure that the efficiency reaches a plateau around 25 GeV and applying a p_T cut of 25 GeV also ensures a good electron kinematic range. The p_T distribution of the two electrons is given in Figure 7.2b and a two-dimensional representation of the trigger efficiency with respect to the transverse momentum of the leading and the sub-leading electrons is given in Figure 7.3.

Note: The geometric and the kinematic cuts applied on the electrons define a *fiducial* phase space where the signal is expected to be the strongest. This enables the rejection of backgrounds in regions where it is difficult to estimate accurately.

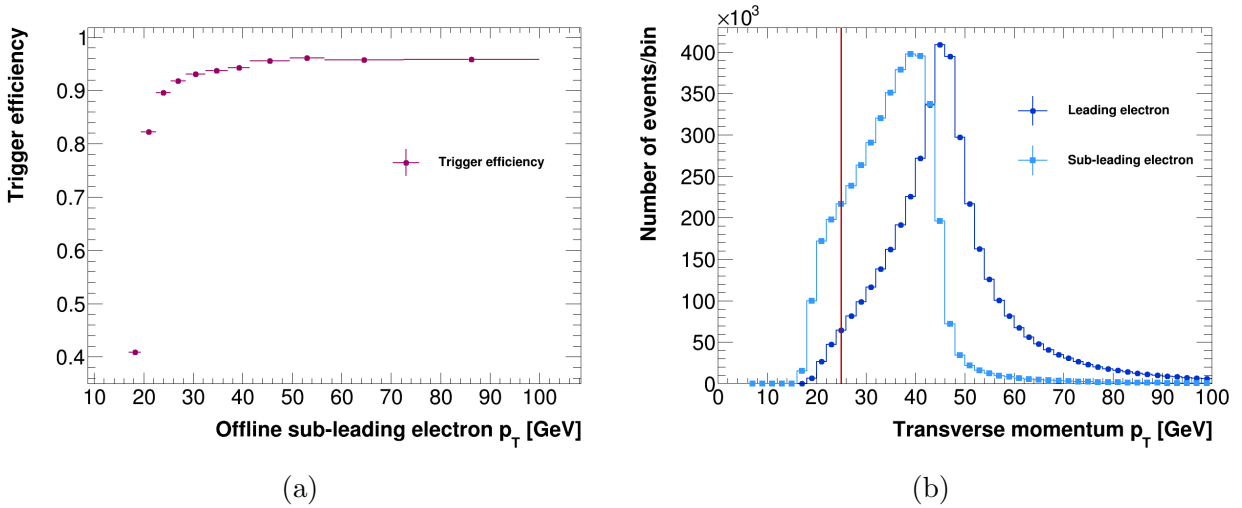


Figure 7.2: The offline trigger turn on curve as a function of the sub-leading electron p_T is given in (a). The threshold p_T is 17 GeV and the trigger turns on to reach the plateau. (b) shows the p_T distribution of the leading and the sub-leading electrons. The red line at 25 GeV represents the p_T cut applied.

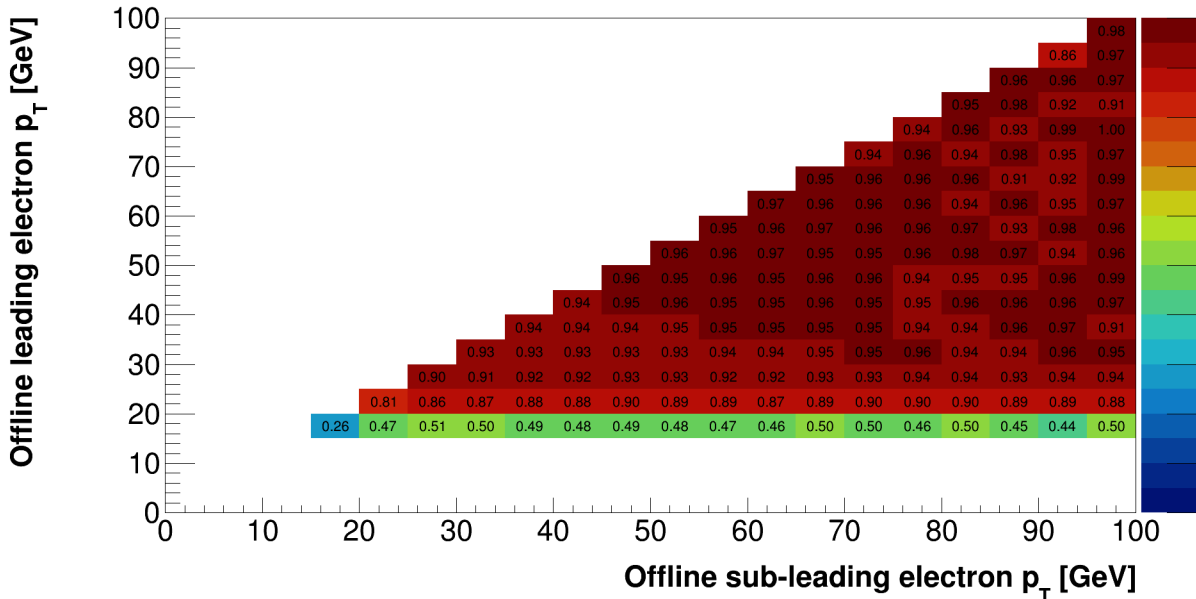


Figure 7.3: A two-dimensional plot of the trigger efficiency calculated is given as functions of the transverse momenta of the leading and the sub-leading electrons. The electron kinematic cut of 25 GeV vetoes events where the trigger efficiency is low.

7.3 Reconstruction Method

As mentioned in the previous chapter, the Z boson cannot be directly observed due to its very short lifetime. Therefore, to reconstruct the Z , one has to work backwards from its observed decay products, two electrons in this case. The concept behind reconstructing a Z boson relies on the simple physics that the rest mass of the particle remains invariant in all frames of reference. One can compute the rest mass, a.k.a. the invariant mass of the Z from the four-momenta of the two electrons to which it has decayed into, as given by Equation 7.2.

$$\begin{aligned} M_{e^+e^-} &= |p_{e^+} + p_{e^-}| \\ &= \sqrt{(E_{e^+} + E_{e^-})^2 - (\vec{p}_{e^+} + \vec{p}_{e^-})^2} \end{aligned} \quad (7.2)$$

Here, $M_{e^+e^-}$ is the reconstructed invariant mass of the di-electron system. E is the energy, p is the four-momentum and \vec{p} is the three momentum of the decay particle.

The measurement of the reconstructed mass on a statistical basis follows a probability distribution according to a Breit-Wigner function [83], as given in Figure 7.4. A Breit-Wigner distribution is used to model resonances, such that the peak of the distribution corresponds to the resonance mass or in other words, the most probable mass a particle can take when it is produced on-shell.

The full width of the distribution at its half

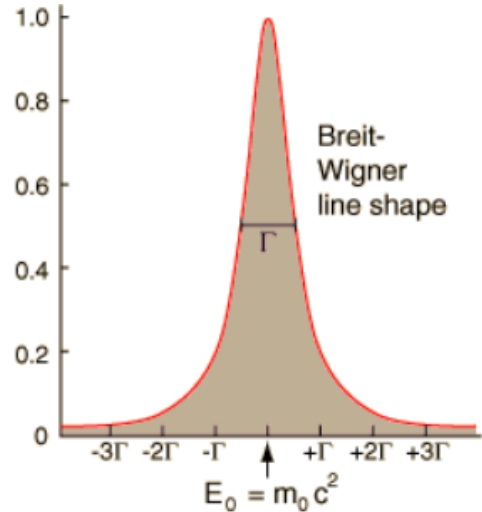


Figure 7.4: A graphic representation of a Breit-Wigner distribution is given [82].

maximum gives the particle decay width, Γ , which is related to its mean lifetime, τ , as $\tau = 1/\Gamma$. The invariant mass of the di-electron system reconstructed according to Equation 7.2 needs not necessarily correspond to a Z boson in all the events. Remember that the mediator can be a Z boson or a γ^* [see Section 3.1]. In the lower mass range, the mediator is likely to be a γ^* while in a higher mass window, the mediator is usually a mixed state of the two bosons. Therefore, it is essential to choose a mass range, where the mediator is more likely to be a Z boson, which is near the Z resonance. The mass range chosen for this analysis is 66-116 GeV. Events where $M_{e^+e^-} \in [66, 116]$ GeV are selected and all other events are vetoed. Table 7.1 summarizes all the event selection criteria used in this analysis [refer to Section 7.1] and the number of events that pass them. The number of events remaining after each criterion is represented graphically in Figure 7.5.

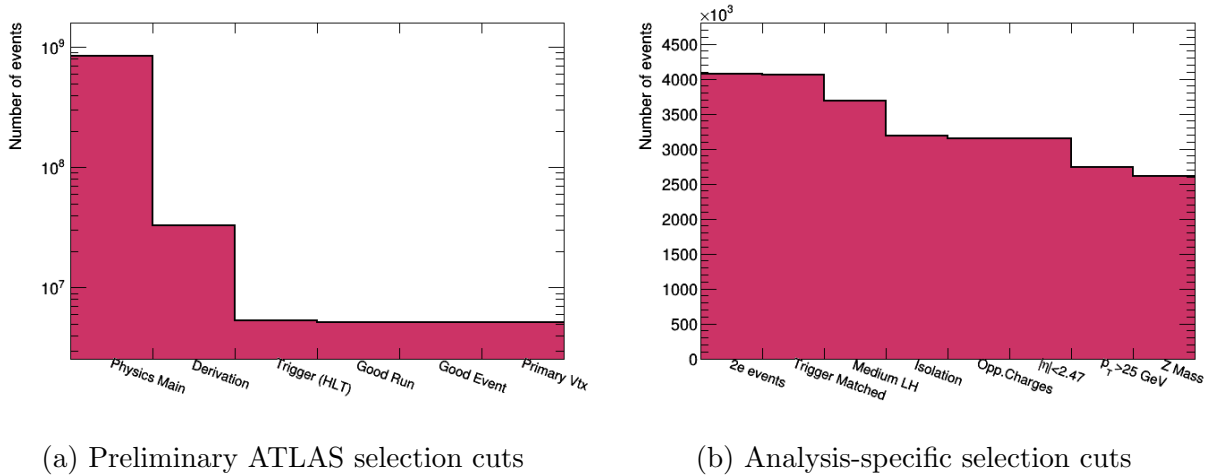


Figure 7.5: Cutflow plots showing the number of events remaining after each event selection criterion.

Variable Name	Description	Number of events	Fraction of events
Physics Main	Events recorded for Physics Main Stream runs in Period L.	838,918,836	100%
Derivation	Events that pass the STD3 derivation.	33,030,863	3.94%
Trigger (HLT)	Events that pass the high-level trigger.	5,300,470	0.63%
Good Run	Events that belong to runs meeting the ATLAS data quality standards.	5,131,777	0.61%
Good Event	Events that pass the additional detector flags.	5,131,777	0.61%
Primary Vtx	Events with a primary vertex.	5,131,777	0.61%
2e events	Events with exactly two reconstructed electrons.	4,066,701	0.48%
Trigger Matched	Events where the electrons are trigger matched.	4,061,121	0.48%
Medium LH	Events where the electrons belong to MEDIUM likelihood operating point.	3,683,459	0.44%
Isolation	Events where the electrons pass isolation requirements.	3,184,990	0.38%
Opp. Charges	Events where the electrons have opposite sign electric charges.	3,151,625	0.38%
$ \eta < 2.47$	Events where the electrons fall within $ \eta < 2.47$.	3,149,100	0.38%
$p_T > 25$ GeV	Events where the electrons have a $p_T > 25$ GeV.	2,733,497	0.33%
Z Mass	Events where the reconstructed invariant mass of the di-electron system belongs to the Z mass window.	2,614,942	0.31%

Table 7.1: A summary of all the selection cuts used in this analysis is presented. The cut is applied one after the other according to the order given. The total number and the fraction of events remaining after each cut are also tabulated.

Chapter 8

Z Boson Reconstruction

The previous chapter describes the selection criteria an event must satisfy to qualify for signal extraction. It also highlights how Z bosons can be reconstructed from di-electrons. In this chapter, the ATLAS data is examined to reconstruct the Z particle and the results of the analysis are presented.

8.1 Invariant Mass Reconstruction

Following the reconstruction procedure mentioned in Chapter 7 [refer to Section 7.3], the invariant mass of the di-electron system is calculated for every event in the data that pass the event selection criteria. The same selection and reconstruction procedures are performed on the MC sample as well and the results are compared, to verify how accurately the prediction matches with the experimental observation. As the simulated pile-up conditions need not necessarily match with that observed in the data, every event in the MC is re-weighted to emulate the data pile-up for the analysis, using the ATLAS so-called *Pileup Reweighting* tool according to the ATLAS requirements given in [84]. Furthermore, the number of gen-

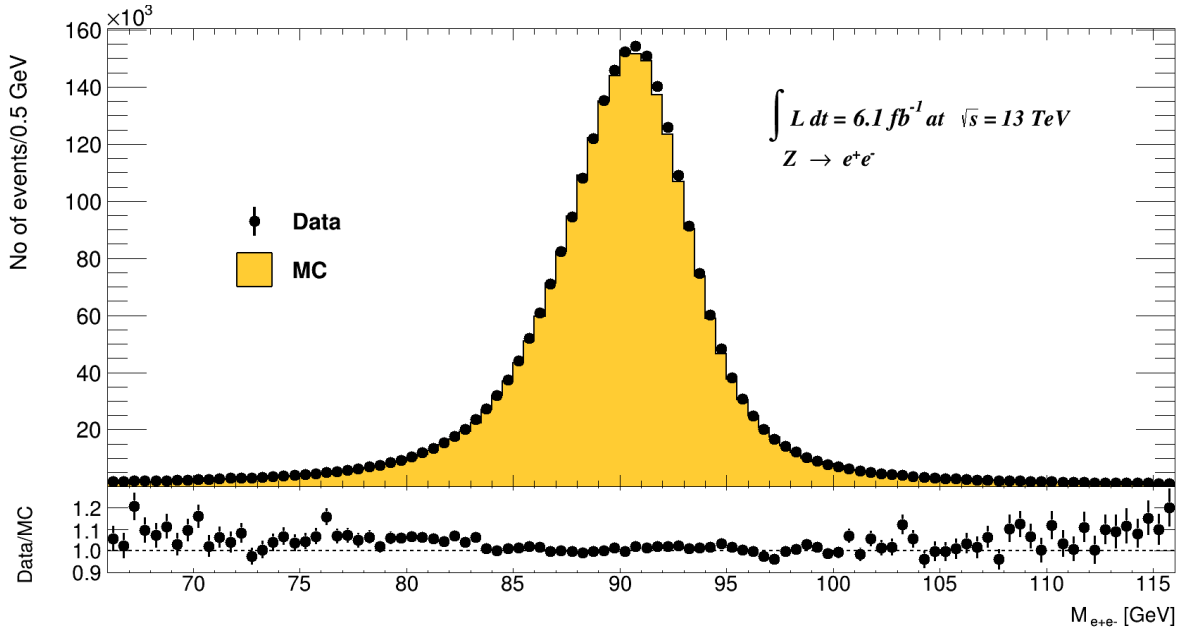


Figure 8.1: The reconstructed invariant mass distribution of the di-electron system is plotted in the chosen Z mass window. The data (in black) is compared with the MC (in yellow). A ratio plot to better understand the bin by bin agreement between the data and the MC is also given. Only statistical errors are shown.

erated events in the MC sample is normalized to the total recorded data events before any comparison is made. The invariant mass distribution for both data and MC at the detector or reconstruction level is shown in Figure 8.1. A very good agreement between the data and the MC can be observed.

At the reconstruction level, the measured electron parameter, say energy, is not the *actual* energy of the electron as the detector is not ideal. The energy recorded as the electron energy by the detector is the “*smearred energy*” which is a function of the calorimeter resolution (tracking resolution in the case of electron momentum). The broader peak in the plot, rather than a narrow resonance peak as one expects [from Figure 7.4], is a manifestation of

this effect. Moreover, if the reconstructed electrons undergo Bremsstrahlung radiation, the measured electron energy is an underestimation of its actual energy. As a consequence, instead of a sharp resonance peak in the invariant mass distribution, one can observe enhanced tails on both sides of the peak, with the low end tail being more prominent in this case, as expected. Also, one cannot neglect the background events. Hence, it is obvious that at the reconstruction level, a Breit Wigner function is not sufficient to describe the observed invariant mass distribution, and apart from background, one must consider the smearing and the radiation effects. To model energy losses due to detection, one of the most commonly used probability density functions in high energy physics is a Crystal Ball function. It consists of a central Gaussian with a power-law low end tail attached to it [85, 86]. To interpret the data, a convolution of Breit Wigner and Crystal Ball functions is used to describe the signal and a constant function is used to estimate the background. The sum of the two functions is fitted on the invariant mass distribution as shown in Figure 8.2.

Background Estimation

Out of the 2,614,942 events that pass all the event selection criteria [refer to Table 7.1], 2,567,638 are estimated as the signal events and 47,304 as the background events. The background constitutes only 1.8% of the total events, making the di-electron process one of the cleanest events at the LHC. The chief background process is the $t\bar{t}$ production followed by diboson events [81] which are some of the predominant processes at the LHC [recall Figure 3.1 for the production rates of these events]. $Z \rightarrow \tau^+\tau^-$ events, where the taus subsequently decay into electrons also add to the background. Electrons from all other processes, including photon conversions, decays from heavy quarks, and misidentified hadrons, sum up to only a

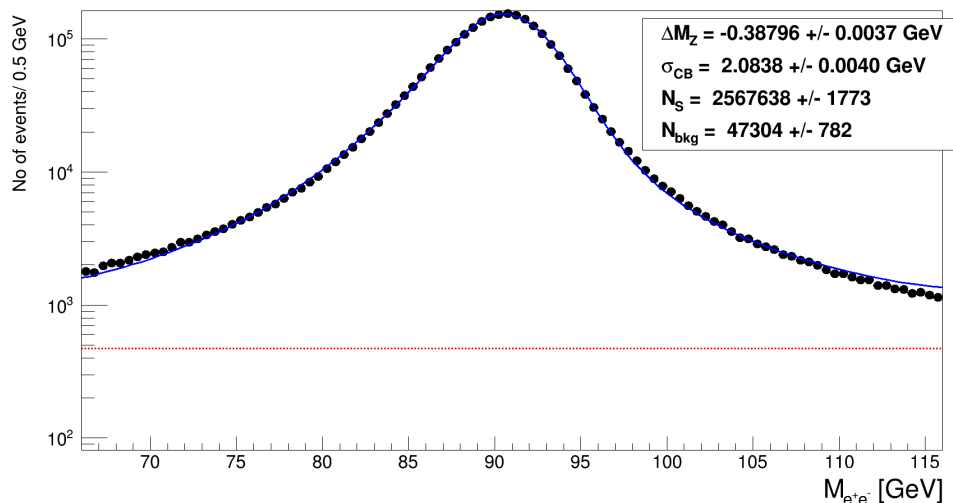


Figure 8.2: A convolution of Breit Wigner and Crystal Ball functions summed with a constant is fitted on the reconstructed invariant mass distribution. The data points are denoted by the black markers and the total fit function is denoted by the blue solid line. The red dashed line denotes the constant used to describe the background. The number of events is given in log scale as the background events are heavily suppressed in linear scale. ΔM_Z indicates the deviation of the Z mass, estimated from the fit, from value recorded by the Particle Data Group (PDG)¹ and σ_{CB} represents the width of the Crystal Ball function. The fit assumes the PDG value [see Section 3.1] for resonance width to compute σ_{CB} .

tiny fraction. Figure 8.3 shows the contribution of the significant background processes in the $Z \rightarrow e^+e^-$ channel.

Mass and Width Sensitivity to Background

One can roughly estimate the sensitivity of the reconstructed mass and width to the background if Gaussian probability density functions are assumed to describe resonance and smearing effects. Considering the background events, one gets a Z mass value of 90.80 GeV and the width of the convoluted function is calculated to be 3.25 GeV. If the background

¹The Particle Data Group is an international collaboration that documents all the public results related to particles and interactions. Hereafter, the values recorded by the PDG will be referenced as *PDG values*.

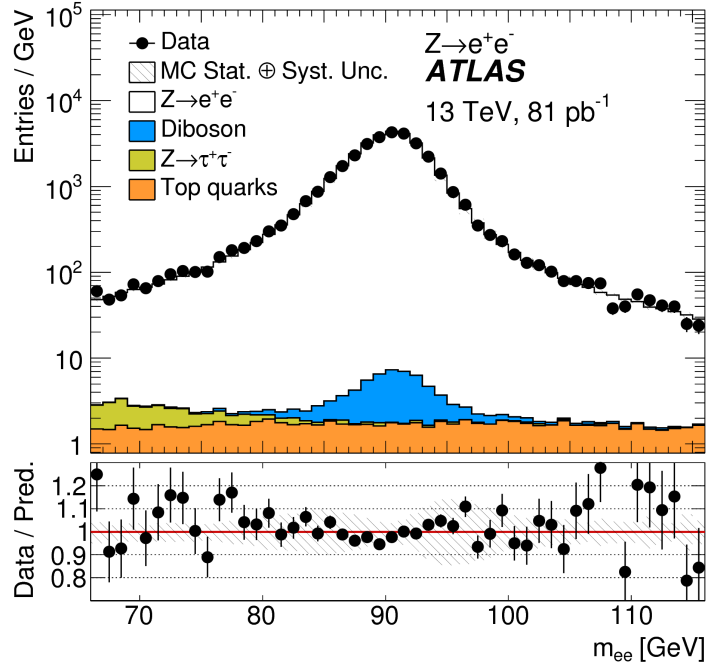


Figure 8.3: A plot of the reconstructed invariant mass of the di-electron system in the Z mass window is shown [81]. It gives a graphic estimate of the contribution of background to the $Z \rightarrow e^+e^-$ process.

is neglected, the mass is 90.75 GeV and the smeared width is 3.3 GeV. In conclusion, the background can affect the mass and the width at most by 0.05% and 1.5% respectively, which is trivial for the purposes of this analysis.

Note: The background events are neglected in the rest of the analysis as its contribution is relatively insignificant.

8.2 Unfolding

Measurements made at the detector level cannot evaluate the “*true physics*” process under study. This is because the reconstructed level information is convoluted by detector and measurement inefficiencies. One can directly access only the reconstructed level information from the data, unlike in MC where both the generator (parton level) and the reconstructed level (detector level) information are directly accessible. To trace back to the parton level from the detector level in the data, one must *unfold* the data, for which the following two terms are introduced.

Acceptance

Out of all the Z-like events produced at the LHC, not all qualify to the final selection step to be analyzed due to the stringent selection criteria. The chosen events fall in the fiducial phase space (both geometric and kinematic) where the signal to the background ratio is expected to be the highest. The fraction of events that pass the fiducial requirements defines the acceptance of the detector and is calculated using MC at the generator level according to Equation 8.1.

$$\text{Acceptance factor } (A) = \frac{\text{Number of events passing the fiducial cuts at the generator level before FSR}}{\text{Number of generated events}} \quad (8.1)$$

It corrects for the theoretical effects including generator dependency and PDFs. With the acceptance factor, one can extrapolate from the fiducial phase space to the total phase space of the detector.

Correction

The correction factor is a term used to account for the detector inefficiencies. It corrects for electron identification, reconstruction, trigger inefficiencies as well as Bremsstrahlung loss. The correction factor is defined using the MC as,

$$\text{Correction factor } (C) = \frac{\text{Number of generated events passing all the final selection requirements at the reconstruction level}}{\text{Number of events passing the fiducial cuts at the generator level before FSR}} \quad (8.2)$$

The FSR in the above equation corresponds to the photon radiation emitted by the decay electrons. From the acceptance and the correction factors, one can define the Z boson finding efficiency as $A \cdot C$.

8.3 Mass and Width Measurements

The reconstructed invariant mass distribution, in Figure 8.1, is unfolded by dividing it by the acceptance and the correction factors event-by-event to obtain the parton level information. The distribution is then fitted with a Breit Wigner function and the resonance mass and width are determined. The same fit is applied on the MC sample at the generator level as well to check its validity. The fit is applied on two different mass ranges: 86-96 GeV (peak region) and 66-116 GeV (Z mass window) and the results are tabulated in Table 8.1. The Z boson in the MC has been generated with the exact mass and width as recorded in the PDG but the values measured from the fit differ slightly. In the 86-96 GeV range, the reduced χ^2 , a parameter used to test the goodness of a fit, on the data and the MC is 1.03 and 1.15 respectively. The fit seems to describe the data and its modelling very well at the peak and the measured parameters agree with the PDG values within uncertainties. In the

66-116 GeV range, the reduced χ^2 is 4.47 on the data while it is 16.85 on the MC. The large values of reduced χ^2 are attributed to the tails of the distribution and clearly explain why the measured parameters deviate from the PDG values. Overall, the values still show a good agreement with the expected ones.

	Resonance Mass (M_Z)	Resonance Width (Γ_Z)
PDG	91.1876 ± 0.0021 GeV	2.4952 ± 0.0023 GeV
Fit Range: 86 – 96 GeV		
Data	91.1714 ± 0.0030 GeV	2.4985 ± 0.0075 GeV
MC	91.1600 ± 0.0012 GeV	2.5091 ± 0.0029 GeV
Fit Range: 66 – 116 GeV		
Data	91.1724 ± 0.0030 GeV	2.5744 ± 0.0067 GeV
MC	91.1593 ± 0.0012 GeV	2.5757 ± 0.0025 GeV

Table 8.1: The resonance mass and width along with the statistical uncertainties on the measurements are tabulated. A Breit Wigner function is fitted on the invariant mass distribution of the unfolded data and the MC sample at the generator level. The parameters obtained from the fit are recorded and compared with the PDG values.

Note: The ECal is calibrated with the precise knowledge of the Z mass from the $Z \rightarrow e^+e^-$ channel. The measurements of the mass and the width made in this thesis are therefore an exercise to cross-check the results.

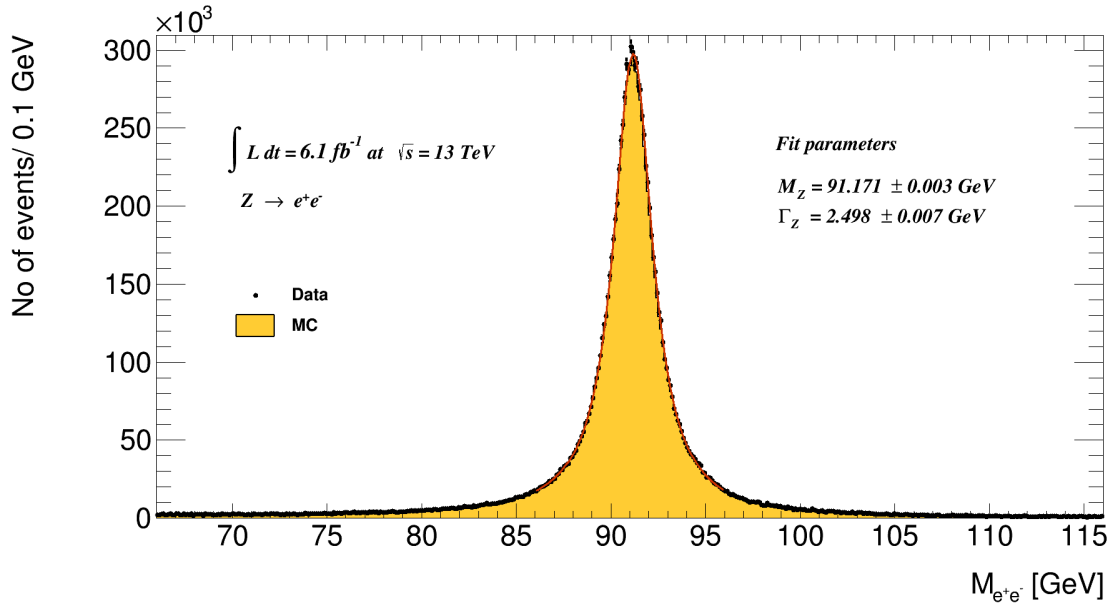


Figure 8.4: The invariant mass distribution of the di-electron system in the unfolded data is compared with the MC at the generator level. The Breit Wigner fit (in red) shown in the figure is applied on the data in the **mass range 86-96 GeV**.

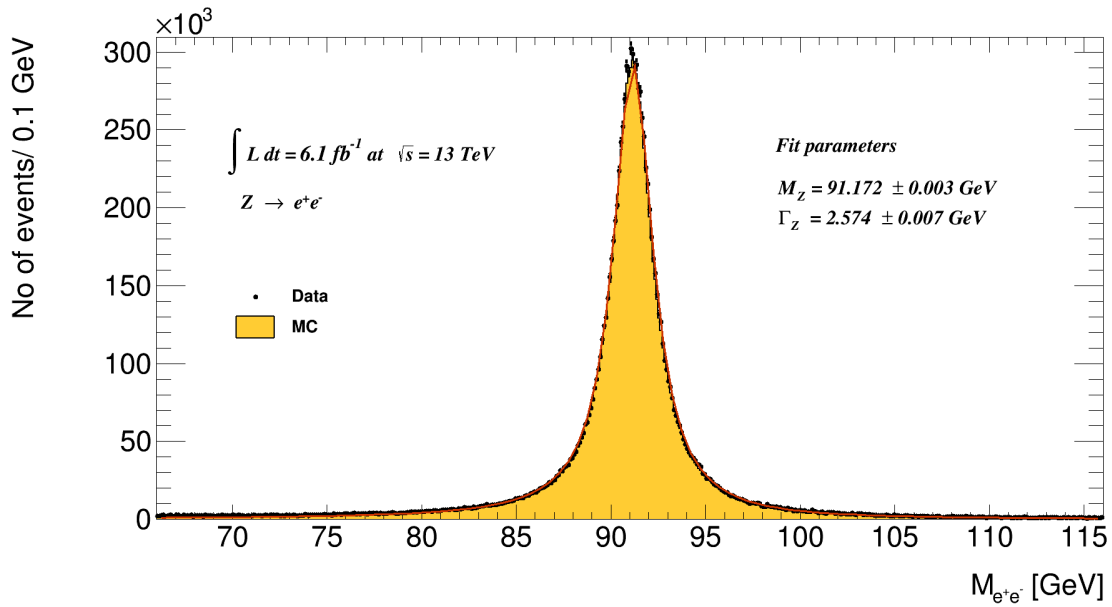


Figure 8.5: The invariant mass distribution of the di-electron system in the unfolded data is compared with the MC at the generator level. The Breit Wigner fit (in red) shown in the figure is applied on the data in the **mass range 66-116 GeV**.

8.4 Geometric and Kinematic Distributions

After reconstruction, the first step is to understand the Z boson distribution in the detector, both kinematic and geometric, before cross-section is calculated. A two-dimensional representation of the Z distribution as a function of its transverse momentum and rapidity can be seen in Figure 8.6a. It is evident that most of the Z bosons are produced at central values of y and have very low p_T .

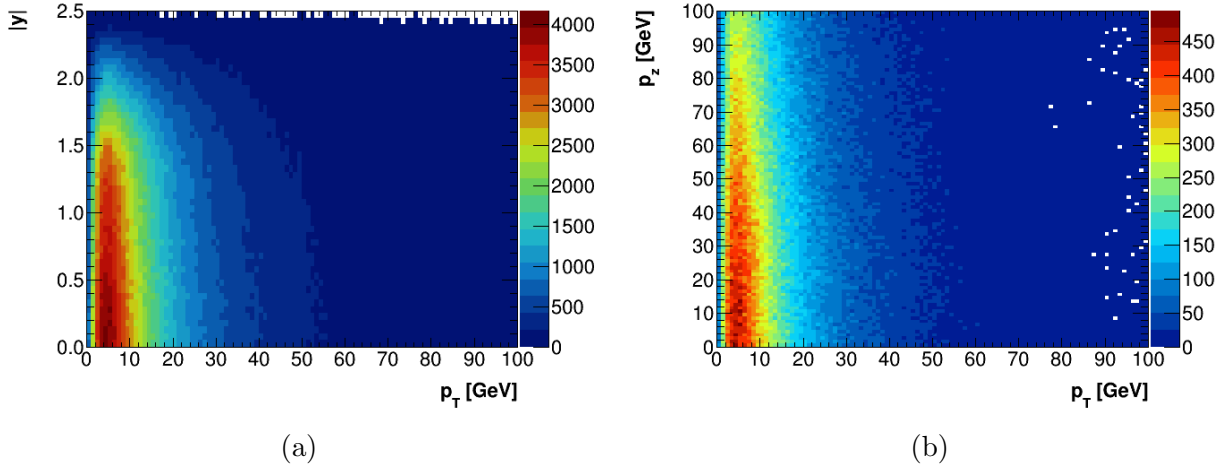


Figure 8.6: Two-dimensional representation of the distribution of the reconstructed Z bosons as functions of 1) p_T and $|y|$ is shown in Figure 8.6a and 2) p_T and p_z is shown in Figure 8.6b.

It is quite interesting as well to look at the longitudinal momentum distribution, p_z , of the Z particle, Figure 8.6b. There is a big concentration of events at low p_T covering a wide range of p_z . The low p_T events are usually generated by $q\bar{q}$ annihilation processes. If the Z particle produced is longitudinally boosted, then it is more likely that the quark involved in the $q\bar{q}$ annihilation is the valence quark of the incoming proton. One must recall from Chapter 2 that the valence quarks are more probable to carry a greater fraction of the incoming

proton's momentum compared to the anti-quarks emerging from the sea [recall Figure 2.3]. As a result, the Z bosons produced thereby carry significant longitudinal momentum. There is also a possibility that both the incoming quark and the anti-quark carry almost the same momentum. In such cases, the Z bosons are transversely produced. In the high p_T regime, there is also an enhanced likelihood that the Z particles are produced from $qg \rightarrow Z + jet$ processes, where the jet in the final state results from the hadronization of the outgoing quark or gluon. As a result, the bosons undergo high momentum recoil from the associated jets produced.

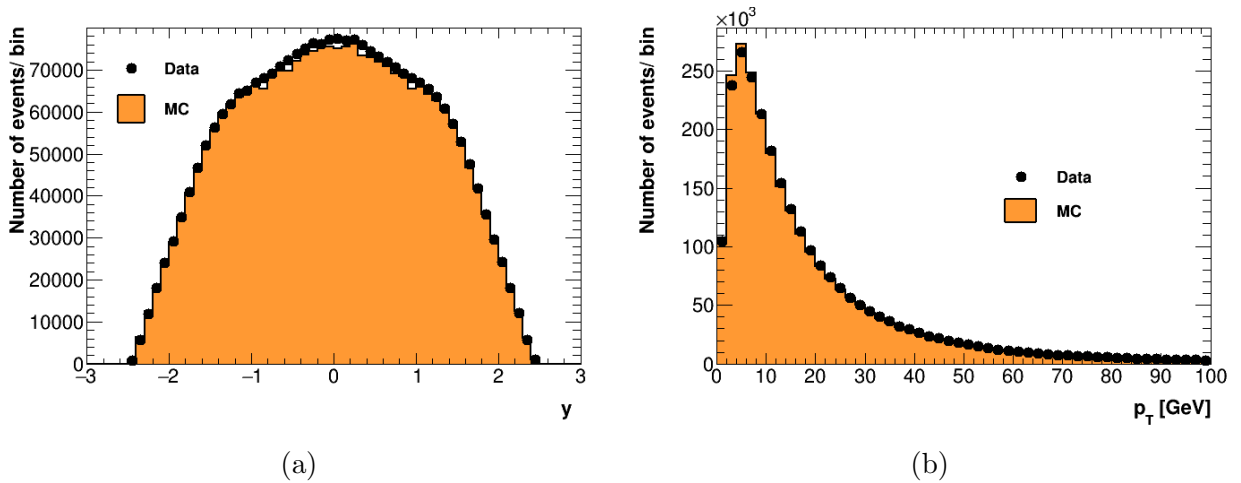


Figure 8.7: The rapidity distribution of the reconstructed Z bosons is shown in Figure 8.7a for all p_T . Figure 8.7b plots the transverse momentum spectra of the reconstructed Z for all values of y .

The distribution of the Z boson as a function of p_T and y , both the variables being Lorentz invariant, are of interest to this thesis. Figure 8.7a and Figure 8.7b show respectively the rapidity and the transverse momentum distributions of the Z boson. One can notice that the reconstructed Z bosons cover a wide range of p_T and fall within a rapidity range of $|y| < 2.5$. A more careful examination of the distributions can be made from Figure 8.8 which plots the

Z p_T in different ranges of $|y|$ for both data and MC. The results show good agreement with the predictions and the small deviations at low p_T arise from possible background events and poor modelling of non-perturbative corrections.

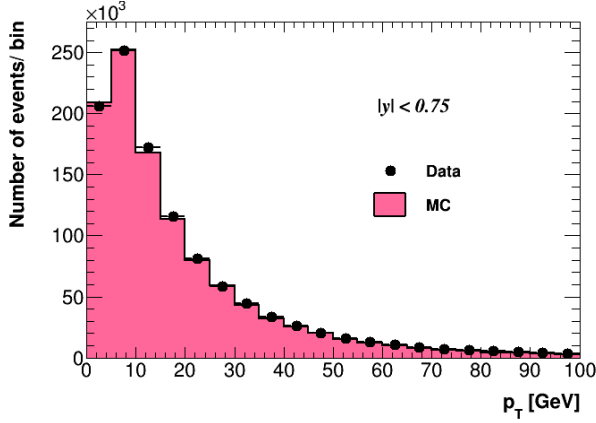
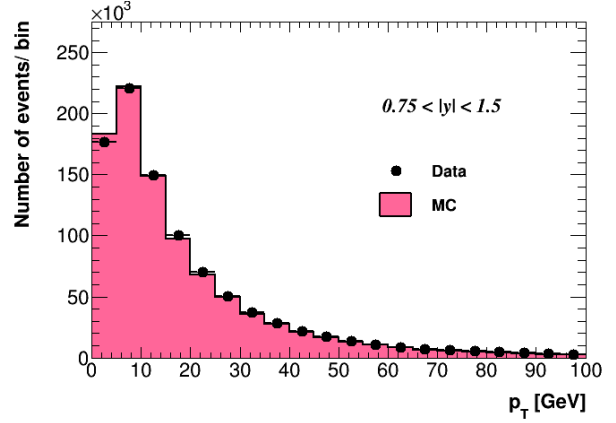
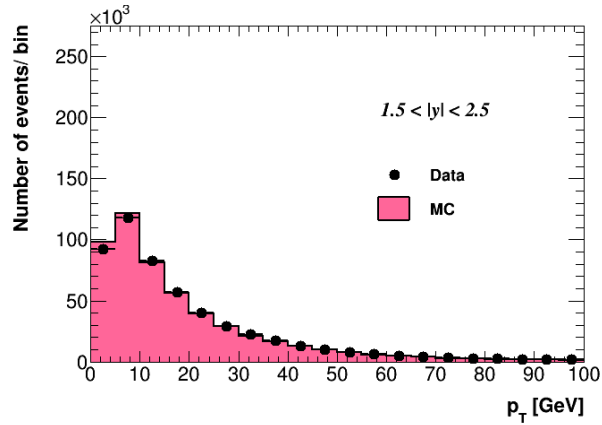
(a) For $|y| < 0.75$ (b) For $0.75 < |y| < 1.5$ (c) For $1.5 < |y| < 2.5$

Figure 8.8: The transverse momentum spectra of the reconstructed Z bosons in different ranges of $|y|$.

Part II

Cross-Section Measurement

Chapter 9

Results

9.1 Total Cross-Section Measurement

The measurement of the production of the Z boson is one of the fundamental and the most important studies at ATLAS to test the Standard Model. One can recall from Section 4.6.2 that the number of $pp \rightarrow Z$ events, N , produced at the LHC in a given period is the corresponding luminosity delivered, \mathcal{L} , times the Z production cross-section, $\sigma_{pp \rightarrow Z}$. $\sigma_{pp \rightarrow Z}$ is the total inclusive cross-section for Z production, as in Equation 9.1.

$$\sigma_{pp \rightarrow Z} = \frac{N_{pp \rightarrow Z}}{\mathcal{L}}, \quad (9.1)$$

Since the analysis presented here uses the di-electron channel to reconstruct the Z particle, the cross-section formula can be re-written as,

$$\underbrace{\sigma_{pp \rightarrow Z} \times BR(Z \rightarrow e^+e^-)}_{\sigma_{pp \rightarrow Z \rightarrow e^+e^-}} = \frac{N_{pp \rightarrow Z \rightarrow e^+e^-}}{\mathcal{L}}. \quad (9.2)$$

Hereafter in this thesis, cross-section refers to $\sigma_{pp \rightarrow Z \rightarrow e^+e^-}$, the left-hand side of Equation 9.2.

One has to keep in mind that, when dealing with events at the reconstruction level, the detector corrections must be applied [refer to Section 8.2]. The production cross-section calculated in the fiducial phase space can be defined as the fiducial cross-section and is given by Equation 9.3

Fiducial cross-section:

$$\sigma_{fid} = \frac{N_{sig} - N_{bkg}}{\mathcal{L} \cdot C} \quad (9.3)$$

Here, N_{sig} and N_{bkg} denote the number of reconstructed signal and background events, respectively, and C is the correction factor [**Note:** N_{bkg} is neglected in this analysis, refer to Section 8.1]. The fiducial cross-section can be extrapolated to the entire detector phase space to obtain the total cross-section by accounting for the detector acceptance, A [see Equation 9.4].

Total cross-section:

$$\sigma_{tot} = \frac{N_{sig} - N_{bkg}}{\mathcal{L} \cdot A \cdot C} \quad (9.4)$$

	value \pm stat
N_{sig}	2614942 \pm 1617
A	0.3911 \pm 0.0003
C	0.5795 \pm 0.0005
\mathcal{L} [fb ⁻¹]	6.1
σ_{fid} [nb]	0.7343 \pm 0.0008
σ_{tot} [nb]	1.878 \pm 0.002

Table 9.1: The measured values of the number of signal events, N_{sig} , acceptance factor, A , and correction factor, C , and the calculated cross-sections in the di-electron channel are tabulated. σ_{fid} and σ_{tot} denote the fiducial and the total cross-sections respectively in nanobarns. The uncertainties quoted are the statistical uncertainties.

9.1.1 Uncertainties

Statistical Uncertainties

Statistical uncertainties on any measurement arise as a result of the finite size of the sample used in the study. This uncertainty can be reduced with more data. The measured cross-sections for the di-electron channel and the respective statistical uncertainties are recorded in Table 9.1. The integrated luminosity used is 6.1 fb⁻¹. The uncertainties on the acceptance and the correction factors are determined from the Bayesian errors on the ratio of two Poisson processes, and Poisson error is used for N_{sig} .

Systematic Uncertainties

In any measurement, one cannot stop with the statistical uncertainty but needs to account for the systematic uncertainties as well. All uncertainties in the measurement that

arise not as a result of the statistics available in the data can be attributed as systematic uncertainties.¹ For any source of uncertainty, the respective variable is altered and the effect on the measured parameter is calculated. For example, to study how the uncertainty on the electron energy resolution affects the cross-section measurement, the electron energy is altered by the uncertainty on the ECal resolution in both directions (up and down) from the nominal energy value and the effect on the measured cross-section is calculated. In this analysis, six sources of systematics associated with electrons have been studied.

1. Energy Resolution
2. Energy Scale
3. Reconstruction Efficiency
4. Identification Efficiency
5. Isolation Efficiency
6. Trigger Efficiency

The Monte Carlo simulations cannot fully emulate the energy resolution as observed in the data. Therefore, the electron energy in the simulated sample is smeared and the uncertainty involved in the smearing procedure amounts to the systematics due to energy resolution. With the precise knowledge of the Z mass distribution from di-electron events, the electron energy in the MC can be scaled to match the mass distribution. The uncertainty in the scaling method is evaluated as the energy scale systematics. The remaining uncertainties come from the MC simulations of the electron reconstruction, identification, isolation and trigger efficiencies. Systematic uncertainty is one of the inevitable challenges in any measurement

¹It must be noted that some systematic uncertainties can result from statistical limitations as well.

and its contribution is not negligible. To have a general understanding of its role in any measurement, one can look at Figures A.1-A.6 in Appendix A, which shows graphically how the electron systematics affect the reconstructed Z mass distribution.

In the cross-section measurement, the electron systematics affect only the correction factor and its overall effect on the cross-section is recorded in Table 9.2. The uncertainty associated with the electron identification efficiency is the highest, which is a consequence of the significant background contamination involved in the electron identification procedure followed in ATLAS [further information can be found in [80]]. Another source of systematic uncertainty is the background omission in this analysis. An uncertainty of 2.2% on the integrated luminosity based on the ATLAS recommendations is also considered [87, 88]. The systematic uncertainty on the acceptance factor arises from the theoretical uncertainties associated with the modelling of Z production and the PDFs. This uncertainty is not accounted for as it falls beyond the scope of this thesis. Table 9.3 summarizes all the systematic uncertainties studied in this thesis. One can notice that the uncertainty associated with the integrated luminosity measurement is the largest contributor to the overall systematic uncertainties and efforts are constantly ongoing in ATLAS for improved results. The uncertainty associated with background omission affects the cross-section only in the lowering direction as the cross-section can never improve with the presence of background. The results of the measured cross-section, the statistical uncertainty, and the systematic uncertainty, are presented in Table 9.4. Due to the large uncertainty on luminosity measurement, its associated uncertainty on the cross-section is quoted separately. The MC generator, Powheg+Pythia8 in this case, predicts a total cross-section of 1.901 nb [89] at NLO and the measured value agrees well with the prediction within the uncertainties.

Electron Systematics	Uncertainty on σ_{fid}	Uncertainty on σ_{tot}
Energy Resolution	+0.0012, -0.0000	+0.003, -0.000
Energy Scale	+0.0012, -0.0000	+0.003, -0.000
Reconstruction Efficiency	+0.0039, -0.0000	+0.010, -0.000
Identification Efficiency	+0.0168, -0.0149	+0.043, -0.038
Isolation Efficiency	+0.0039, -0.0039	+0.010, -0.010
Trigger Efficiency	+0.0000, -0.0000	+0.000, -0.000
Total	+0.0178, -0.0154	+0.045, -0.039

Table 9.2: The systematic uncertainties on the measured fiducial and total cross-sections due to the systematic uncertainty associated with the electrons are tabulated. The total uncertainty given corresponds to the uncertainties associated with each source added in quadrature.

Systematics associated with	Uncertainty on σ_{fid}	Uncertainty on σ_{tot}
Electrons	+0.0178, -0.0154	+0.045, -0.039
Background Omission	+0.0000, -0.0133	+0.000, -0.034
Integrated Luminosity	+0.0162, -0.0162	+0.042, -0.042

Table 9.3: The systematic uncertainties on the measured fiducial and total cross-sections due to the systematic uncertainty associated with the electrons, background omission and measured integrated luminosity are tabulated.

Cross-section	value	\pm stat	\pm syst	\pm lumi
σ_{fid} [nb]	0.7343	± 0.0008	$^{+0.018}_{-0.020}$	± 0.016
σ_{tot} [nb]	1.878	± 0.002	$^{+0.045}_{-0.052}$	± 0.042
σ_{pred} [nb]	1.901 [89]			

Table 9.4: The values of the fiducial and the total cross-sections measured in nanobarns and the uncertainties on the measurements are given. The uncertainties on the cross-section presented arise from the statistical uncertainty (stat), the systematic uncertainty associated with electrons and background omission (syst) and the systematic uncertainty associated with the integrated luminosity measurement (lumi). The values quoted for syst are the uncertainties related to electrons and background omission, given in Table 9.3, added in quadrature. The cross-section predicted by the MC generator, denoted by σ_{pred} , is also tabulated.

9.2 Differential Cross-Section Measurement

The measurement of the differential cross-section of Z production serves as an important test of the predictions of the Standard Model as it explores in more detail all regions of phase space and is very sensitive to the presence of new physics. Many processes beyond the Standard Model predict heavy particles that decay into high p_T Z bosons. In addition, the di-lepton distributions serve as important background processes in many searches for new physics where high p_T leptons can mimic the signatures of the predicted particles. If such processes exist in nature, it will be reflected in the differential measurements. In a differential cross-section measurement, one can study the cross-section as a function of various kinematic and geometric variables. Mathematically, differential cross-section, $\sigma(x)$, as a function of a variable x can be defined as:

$$\sigma(x) = \frac{d\sigma}{dx}, \quad (9.5)$$

such that the total cross-section is,

$$\sigma = \int \frac{d\sigma}{dx}. \quad (9.6)$$

In this thesis, the y distribution and the p_T spectrum of the Z boson are studied, both the variables being Lorentz invariant, and the results are presented.

9.2.1 Transverse Momentum Distribution

The production cross-section of the Z particle measured differentially with respect to its p_T in the total detector phase space is plotted in Figure 9.1. The cross-section is the largest at low values of Z p_T and exhibits a falling trend, which is in agreement with the previous results from ATLAS and CMS given in Figure B.1 in Appendix B. When the distribution

is integrated over the entire p_T spectrum, the measured total cross-section of 1.878 nb is retrieved. The data and the MC exhibit deviations at high p_T . This is attributed to the poor modelling of higher order corrections at high p_T in the MC. Better agreement is gained with computations that include jets in the events [90]. One can take a closer look at the double differential cross-section of Z production in Figures C.1-C.3 in Appendix C, which plots the cross-section as a function of p_T in different slices of rapidity.

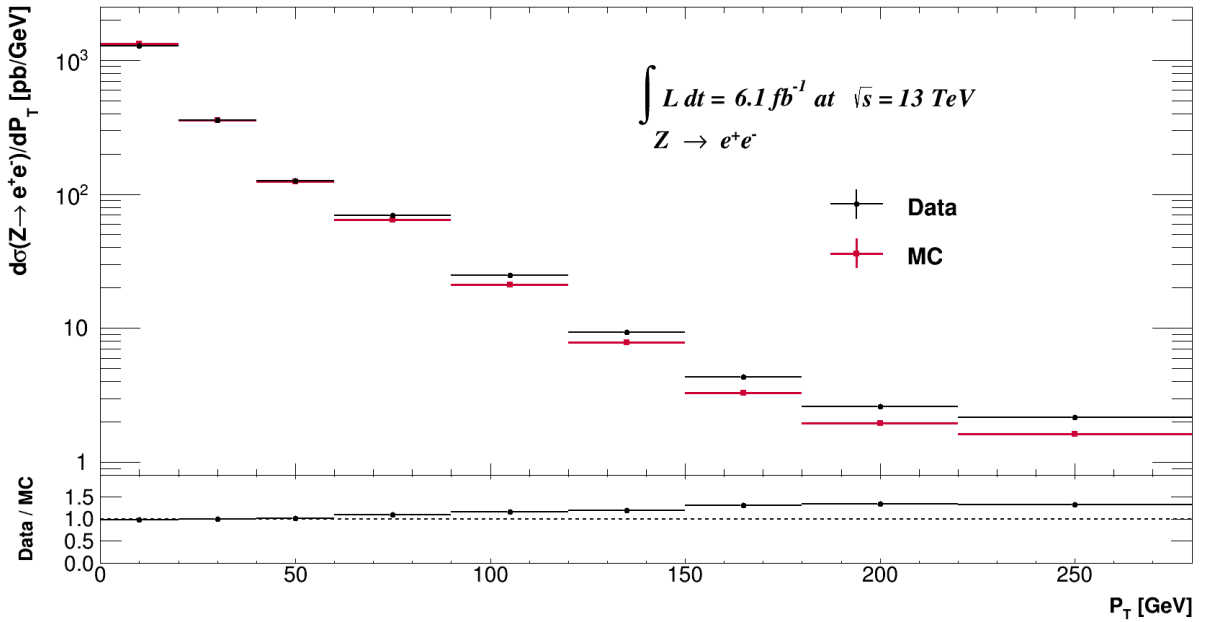


Figure 9.1: The differential cross-section of Z production as a function of the transverse momentum extrapolated to the total detector phase space is plotted. The cross-section is the highest in the very low p_T range. The unfolded data (corrected for acceptance and reconstruction) shows good agreement with the prediction.

9.2.2 Rapidity Distribution

The distribution of the Z cross-section in the fiducial phase space (data corrected only for reconstruction) as a function of its rapidity is shown in Figure 9.2. The measured fiducial

cross-section is obtained when the distribution is integrated over the entire rapidity range. It can be noticed from the figure that there are no Z boson events at large rapidities in the fiducial region.

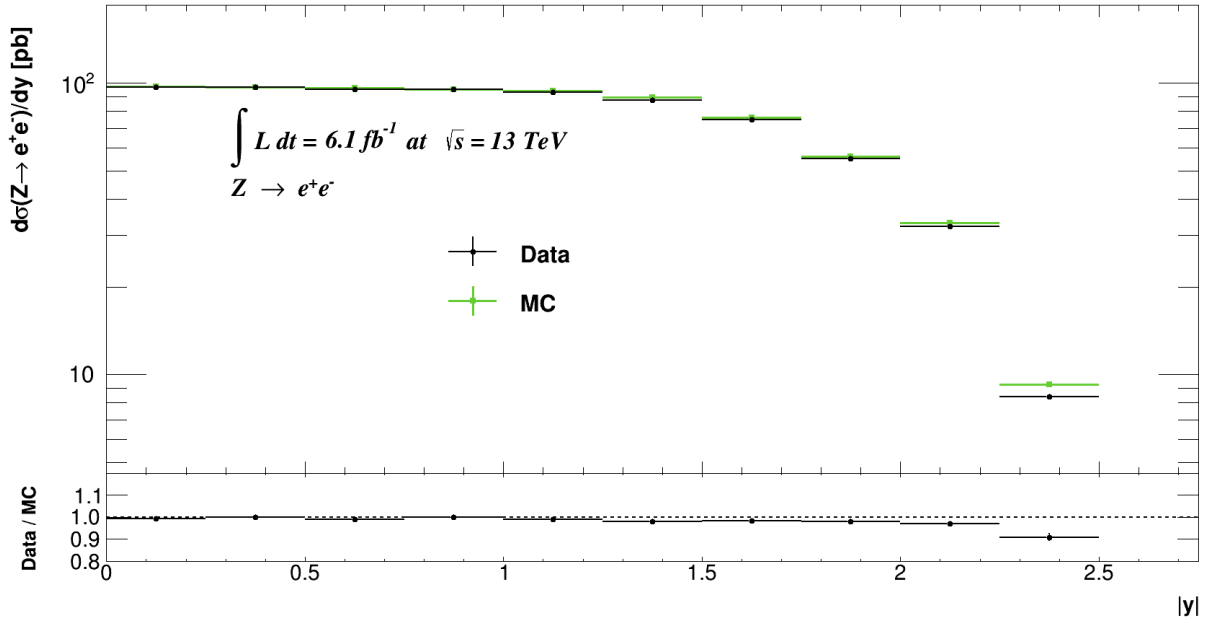


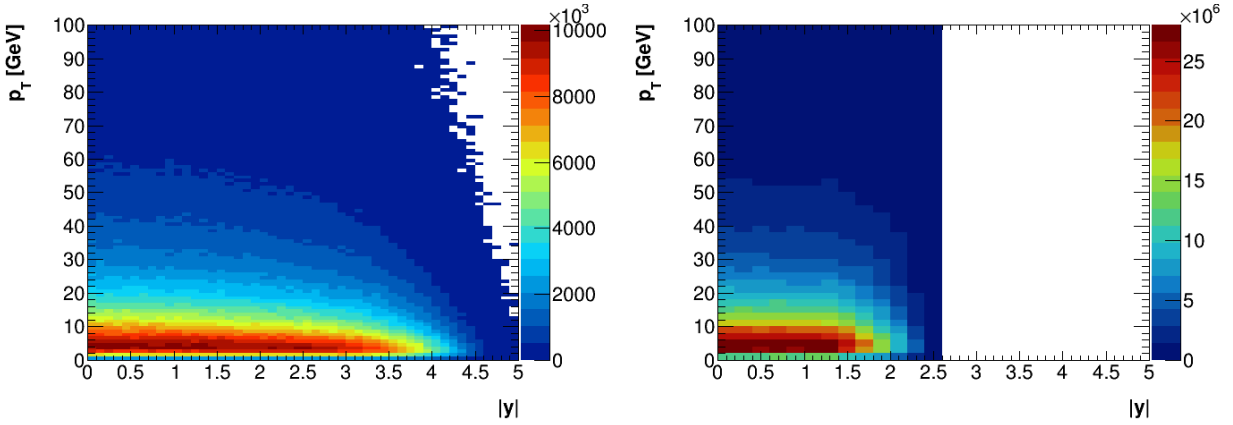
Figure 9.2: The differential Z production cross-section as a function of the rapidity measured in the fiducial phase space is plotted. There are no events in $|y| > 2.5$.

The cross-section measurement as a function of the Z rapidity is initially studied only in the fiducial region because of the zero detector acceptance for $|y| > 2.5$ at the reconstruction level. This is explained in detail below.

Unrepresented phase space

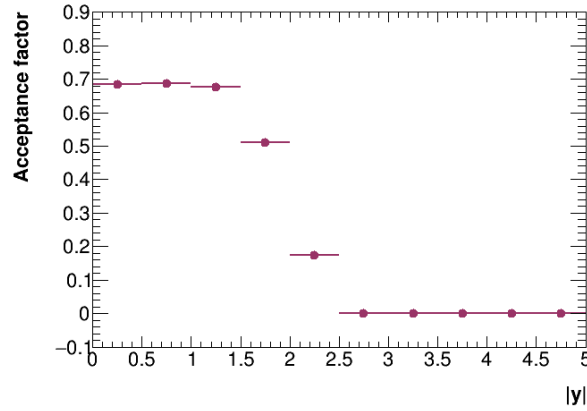
Out of all the Z events generated in the MC sample, none of them passes acceptance and reconstruction for $|y| > 2.5$. From Figure 9.3, one can see that even though there are generated events in the high rapidity range, the detector acceptance is zero due to the cuts

on electrons. With a zero value of acceptance factor, the cross-section information in the fiducial region cannot be extrapolated to the total phase space. Furthermore, no generated events pass reconstruction in the MC sample in this range [see Figure 9.4]. As a result, the cross-section remains undefined in the unrepresented region of large rapidities.



(a) Generated Z events

(b) Generated Z events passing acceptance



(c) Acceptance factor

Figure 9.3: Figure 9.3a plots the number of generated Z boson events in the MC as a function of the transverse momentum and the rapidity of the boson. Figure 9.3b plots the number of generated events that pass the detector acceptance as a function of the transverse momentum and the rapidity of the generated Z. The acceptance factor as a function of the rapidity of the generated Z is shown in Figure 9.3c.

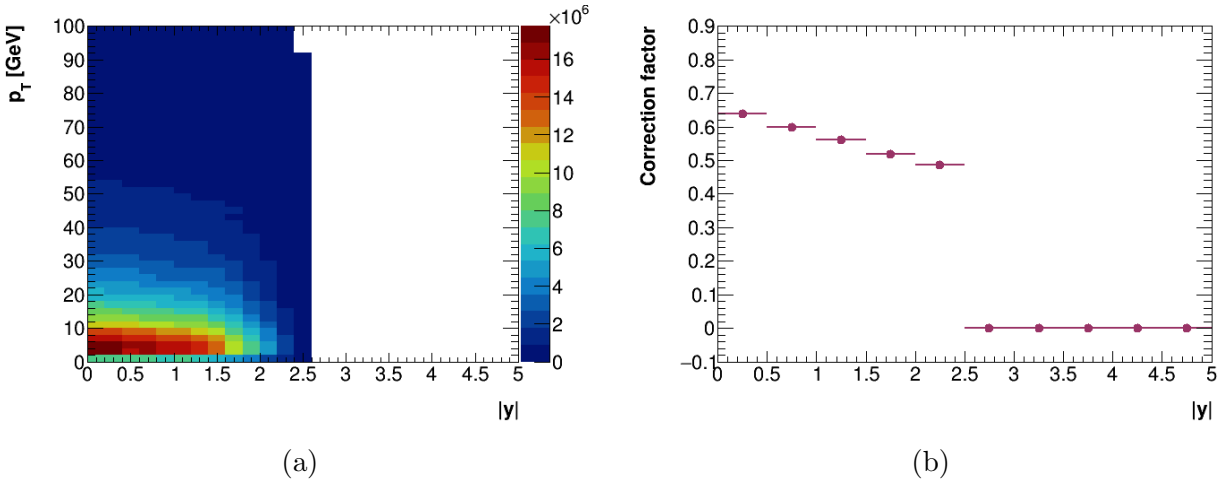


Figure 9.4: Figure 9.4a plots the number of generated events that pass reconstruction as a function of the transverse momentum and the rapidity of the generated Z bosons. The correction factor as a function of the rapidity of the generated Z is shown in Figure 9.4b.

Note: All the generated events that pass acceptance and reconstruction cover the entire Z p_T range even if they fall into $|y| > 2.5$. This is why the differential cross-section measurement as a function of p_T remains unaffected by the unrepresented geometric phase space. In other words, the simulated events at large rapidities fall within the fiducial phase space, thus unfolding covers this rapidity region. For better understanding of the case, a toy example is given in Appendix D.

Due to the limited information at large rapidities, one can only unfold the data up to $|y| = 2.5$. Figure 9.5 shows the cross-section as a function of rapidity with the data unfolded in the accessible Z rapidity range. The Z boson production cross-section integrated in this range is measured to be 1.31 nb, which accounts only for 69% of the total cross-section. The data and the MC show good agreement in the central values of y with slight deviations at the extremes. The distribution is comparable with the previous ATLAS [91] and CMS [92]

results [refer to Figure B.2 in Appendix B]. The cross-section as a function of the rapidity of the Z particle is studied in different slices of p_T , in Figures C.4-C.6 in Appendix C, to better understand the agreement of the data with the predictions. In ATLAS, Z bosons are reconstructed up to $|y| < 2.5$ using central electrons and reconstruction up to $|y| < 3.5$ is possible using the Forward Calorimeter information, which is beyond the scope of this thesis.

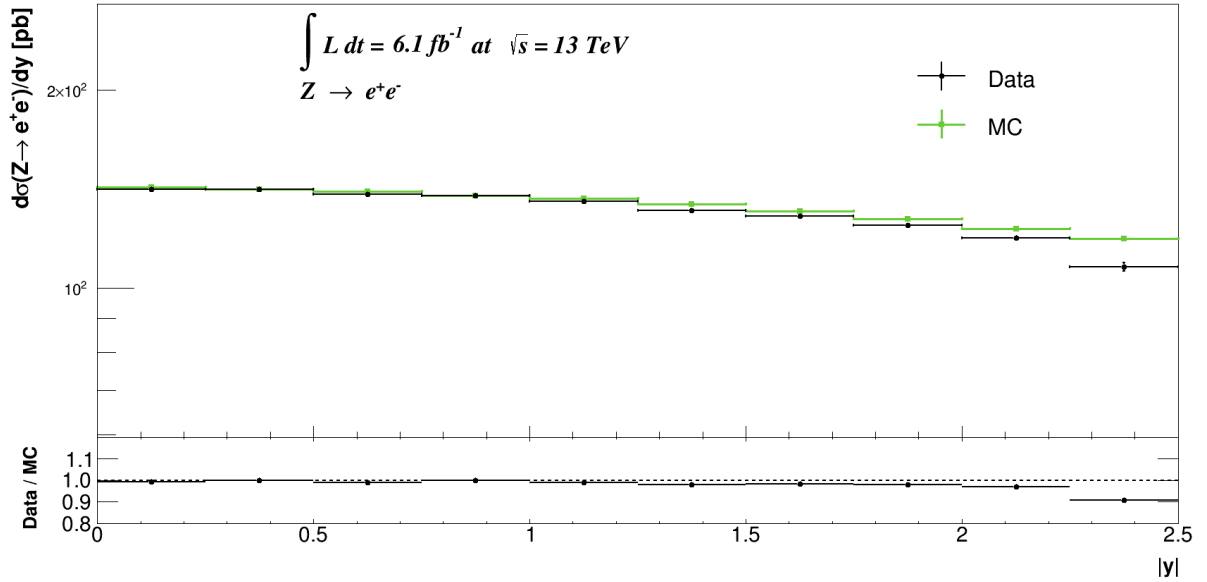


Figure 9.5: The differential cross-section of Z production as a function of rapidity measured within $|y| < 2.5$. The unfolded data (in black) agrees well with the prediction (in green).

Estimate of the total cross-section

As rapidity information from data is missing at high rapidities, to make an estimate of the total cross-section, one can perform an extrapolation depending totally on the MC. Out of the 11,674,598 generated events, only 8,193,450 events fall within $|y| < 2.5$ giving a ratio

of 0.702 which serves as the MC correction to represent the missing phase space and an approximate total cross-section is retrieved [see Equation 9.7].

$$\begin{aligned}\sigma_{tot} &= \frac{\text{Measured total cross-section for } |\mathbf{y}| \text{ upto } 2.5}{\text{MC correction}}, \\ &= \frac{1.31 \text{ nb}}{0.702}, \\ &= 1.87 \text{ nb}.\end{aligned}\tag{9.7}$$

To do a similar estimation from the differential cross-section plotted as a function of $|\mathbf{y}|$, the last bin in Figure 9.5 can be changed to include all the higher rapidities as shown in Figure 9.6, thus getting rid of the impossibility of extrapolation due to empty bins. The number of events in the final bins of both plots are the same but in Figure 9.6, the total cross-section at rapidities above 2.0 is extrapolated using pure MC information, yielding an integrated cross-section of 1.87 nb which is consistent with the measured value within uncertainties. But one must keep in mind that this extrapolation into high rapidities relies totally on the Monte Carlo being correct.

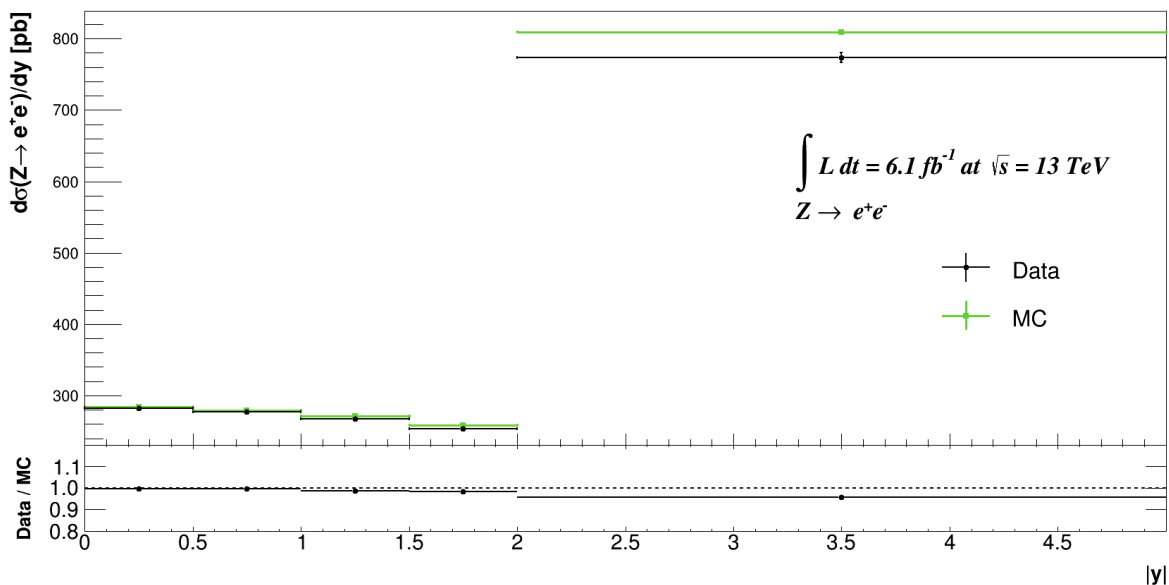


Figure 9.6: The differential cross-section of Z production is plotted as a function of rapidity. The final bin covers a rapidity range of $|y| \geq 2.0$. The higher cross-section in this bin is due to the larger rapidity range.

9.3 Summary

The total and the differential cross-sections of Z production in the di-electron channel have been measured. The total cross-section matches well with the prediction within the uncertainties. The differential cross-section measured as a function of the transverse momentum exhibits a falling trend and agrees with the Standard Model predictions. The distribution represents the entire p_T kinematic range of the Z boson and the total cross-section can be retrieved from the measurement. In the cross-section measured differentially as a function of the rapidity, the data can be unfolded only up to $|y| < 2.5$, therefore the total cross-section cannot be defined from this measurement. But one can recover the fiducial cross-section when the differential measurement is made within the fiducial phase space and the results

are in agreement with the predictions. To verify the consistency of the results, an estimate of the total cross-section from the Z rapidity information has been made by correcting for the missing phase space by relying purely on the MC and the value show good agreement with the measured cross-section within uncertainties.

Part III

Spin

Measurement

Chapter 10

Collins Soper Frame

The previous chapters described how to quantify the Z production at the LHC. The second objective of this thesis is to determine the spin of the Z boson. The principle behind measuring the spin was introduced briefly in Chapter 2. This chapter focuses primarily on detailing the steps involved to determine the spin of the Z boson in a collider environment. As bosons carry an integral spin, the goal is to check if the Z boson possesses a spin of 0, 1 or 2.¹

One knows that the total angular momentum is a conserved quantity. Therefore, when the Z decays into a pair of electrons, the total angular momentum of the decay products, \vec{J}_1 and \vec{J}_2 , must add up to the total angular momentum of the Z boson, \vec{J} :

$$\vec{J} = \vec{J}_1 + \vec{J}_2. \tag{10.1}$$

Unlike the electrons, the Z boson is not directly observed in the detector. Therefore, the easiest method to calculate its spin is to study the Z when it is at rest or in other words, its

¹Self-consistent quantum field theories cannot be constructed for higher spins

orbital angular momentum, \vec{L} , is zero, such that Equation 10.1 becomes,

$$\vec{S} = \vec{J}_1 + \vec{J}_2. \quad (10.2)$$

Because both electrons have the same spin quantum numbers, one can gauge the spin information of the Z from the relative distribution of the electrons, which originates from their orbital angular momentum quantum numbers. This procedure of determining the spin in the Z 's rest frame seems easy and straightforward but there are some inherent complications underlying this method.

Challenges

- The Z bosons are not necessarily produced at rest in the detector. In other words, the rest frame of the Z generally does not coincide with the detector's frame of reference. This is evident from Figure 10.1 which gives the momentum distribution of the reconstructed Z bosons in the laboratory frame. In processes where the Z is produced in association with high p_T jets [refer to Section 8.4], it suffers significant recoil which contribute to the long tails seen in Figure 10.2. Therefore, the laboratory frame is incompatible for an efficient spin study and one has to inevitably switch to the rest frame of the Z boson.

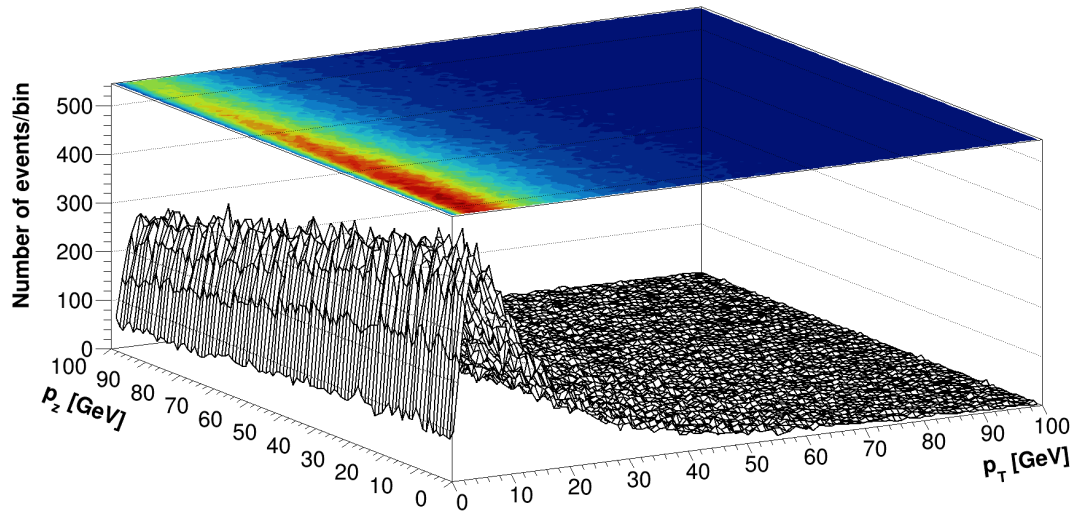


Figure 10.1: A surface plot showing the transverse and the longitudinal momentum distribution of the reconstructed Z bosons. The colored image on the top face gives the projection of p_T and p_z on a two-dimensional plane. This plot is a repetition of Figure 8.6b which had only the two-dimensional projection. Clearly, there is a big concentration of events at low momenta.

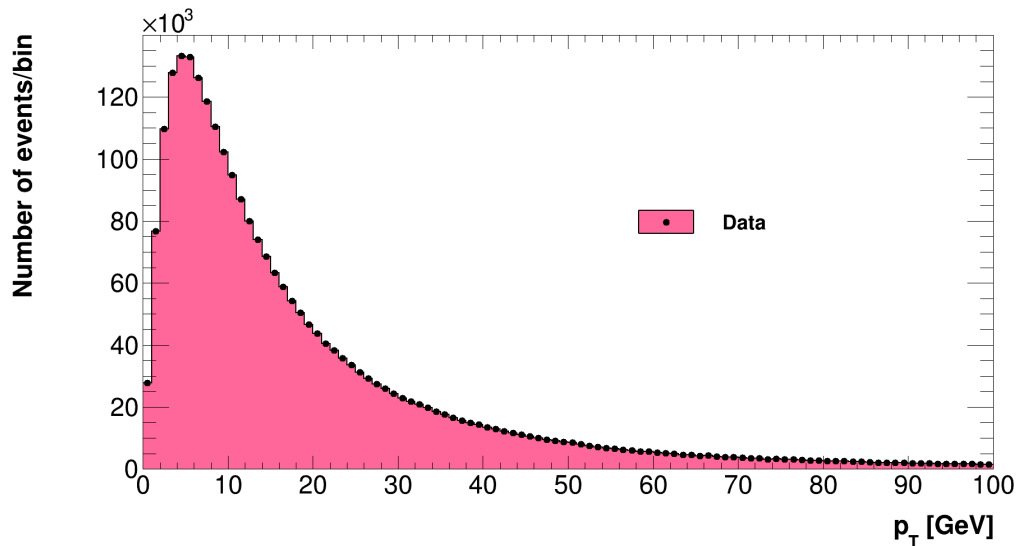


Figure 10.2: A plot showing the transverse momentum distribution of the reconstructed Z bosons. The distribution dies off at high p_T . The data is the one-dimensional projection of Figure 10.1 and shows the long tail.

-
- The angular distribution of the electrons is determined by measuring the polar angle² θ of the electron track.³ As the incoming proton beams move along the z direction, the beams possess zero transverse momentum and the colliding partons are assumed to move collinearly along the beam direction. In such cases, the polar angle of the leptons can be uniquely identified as illustrated in Figure 10.3 for a typical $q\bar{q}$ annihilation. However, this does not hold true for all the events. When the incoming quarks (q , \bar{q} or both) undergo ISR (eg. gluon radiation), they possess a non-zero p_T before collision occurs and are therefore no longer collinear. This is one of the contributing reasons to the observed significant transverse momentum of the Z [Figure 10.2]. In such cases, θ of the lepton track measured in the laboratory will not amount to a correct measure of the angular distribution as there is an ambiguity in the definition of the z -axis.⁴ This can be understood from Figure 10.4 which clearly demonstrates such cases.

²The azimuthal angle, ϕ , gives a symmetric distribution [see Figure 7.1b] and is not the most useful parameter in spin studies.

³Measurement of the polar angle of the electron track is the convention followed in ATLAS. One is free to choose the positron track as well.

⁴This is because one does not know if the quark(s) has undergone gluon radiation.

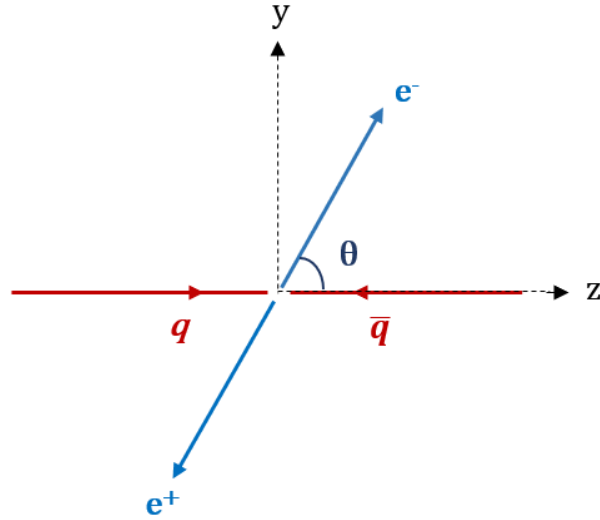


Figure 10.3: A figurative illustration of θ determination of lepton track in a typical $q\bar{q}$ annihilation, when the incoming quarks have zero p_T .

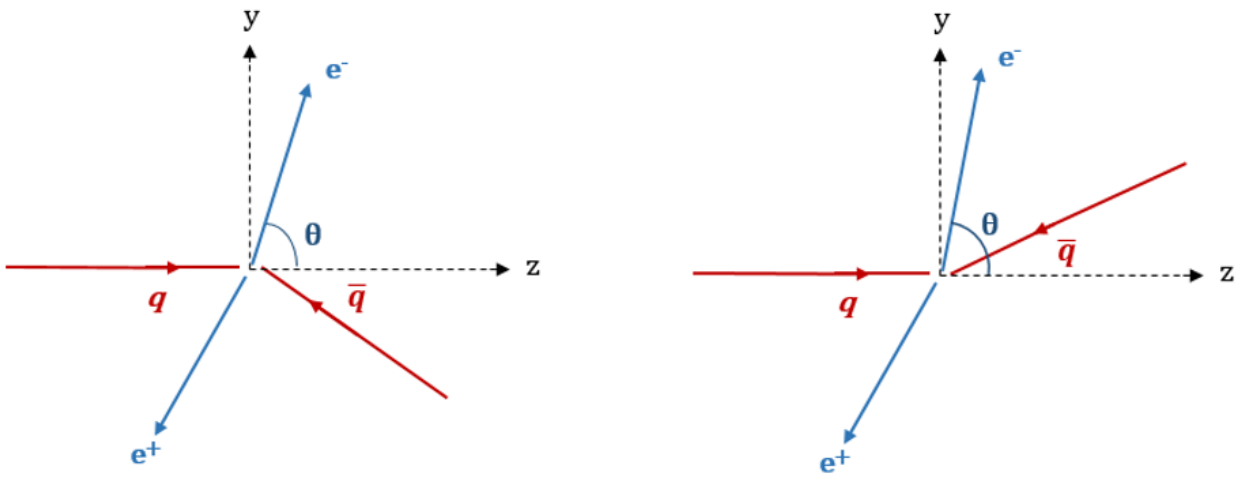


Figure 10.4: A figurative illustration of θ determination of lepton track in a typical $q\bar{q}$ annihilation, when one of the incoming quarks has a non-zero p_T . Such cases for both the incoming quarks are also possible.

-
- Changing to the Z 's rest frame from the laboratory frame poses difficulties because ATLAS uses only a limited number of variables for an inclusive geometric coverage. Therefore, all the parameters required to study the distribution of electrons in the Z 's rest frame may not have the possibility to be measured in the detector. Moreover, the measurable laboratory variables need not be Lorentz invariant in the Z 's rest frame.

A solution to these challenges was brought forth by J.C. Collins and D.E. Soper in the late twentieth century by introducing a new reference frame called the *Collins-Soper frame* (CS frame) [93].

Collins-Soper frame

A Collins-Soper frame is simply the rest frame of the di-lepton system, that is reached when the laboratory frame is Lorentz transformed by a measure of the momentum carried by the Z boson. To switch to the CS frame, first the laboratory frame is boosted longitudinally, followed by a boost in the transverse direction, such that the reconstructed Z is at rest in the new frame (or the CS frame). Figure 10.5 represents schematically how such a transformation is achieved. In the CS frame, the polar axis, denoted by z_{CS} , is defined in such a way that the momenta of the incoming protons have the same angle α with respect to z_{CS} . In other words, the z_{CS} -axis bisects the angle between the momentum of one of the proton beams and the reverse momentum of the other. Such a choice of the polar axis minimizes the effect arising out of the ambiguity in inferring the partons having non-zero transverse momenta. The y_{CS} -axis is chosen as the normal to the plane spanned by the incoming proton beams and the x_{CS} -axis is set so as to satisfy a right-handed Cartesian coordinate system. An elaborate description of the frame can be found in [93, 94].

To measure the angular distribution of the leptons, the general procedure followed by ATLAS is to compute the cosine of the polar angle in the Collins-Soper frame [95], denoted by $\theta_{(\text{CS})}$.

$$\cos \theta_{(\text{CS})} = \frac{p_z(e^+e^-)}{|p_z(e^+e^-)|} \frac{2}{m\sqrt{m^2 + p_{\text{T}}^2}} (P_1^+ P_2^- - P_1^- P_2^+) \quad (10.3)$$

where,

$$P_i^\pm = \frac{1}{\sqrt{2}} (E_i \pm p_{z,i})$$

Here, E_i and $p_{z,i}$ stand respectively for the energy and the longitudinal momentum of the electron ($i = 1$) and the positron ($i = 2$). The longitudinal momentum of the di-electron system is represented by $p_z(e^+e^-)$. m and p_{T} denote respectively the mass and the transverse momentum of the reconstructed Z. The salient characteristic of the CS frame is that the definition of $\cos \theta_{(\text{CS})}$, as given in Equation 10.3, employs only laboratory frame variables. Furthermore, all the variables in the equation are invariant under longitudinal boosts.

To determine the spin of the Z boson, the angular distribution of the di-electron system is studied by measuring $\cos \theta_{(\text{CS})}$ and compared with the predictions for different spins. The results are presented and discussed in the following chapter.

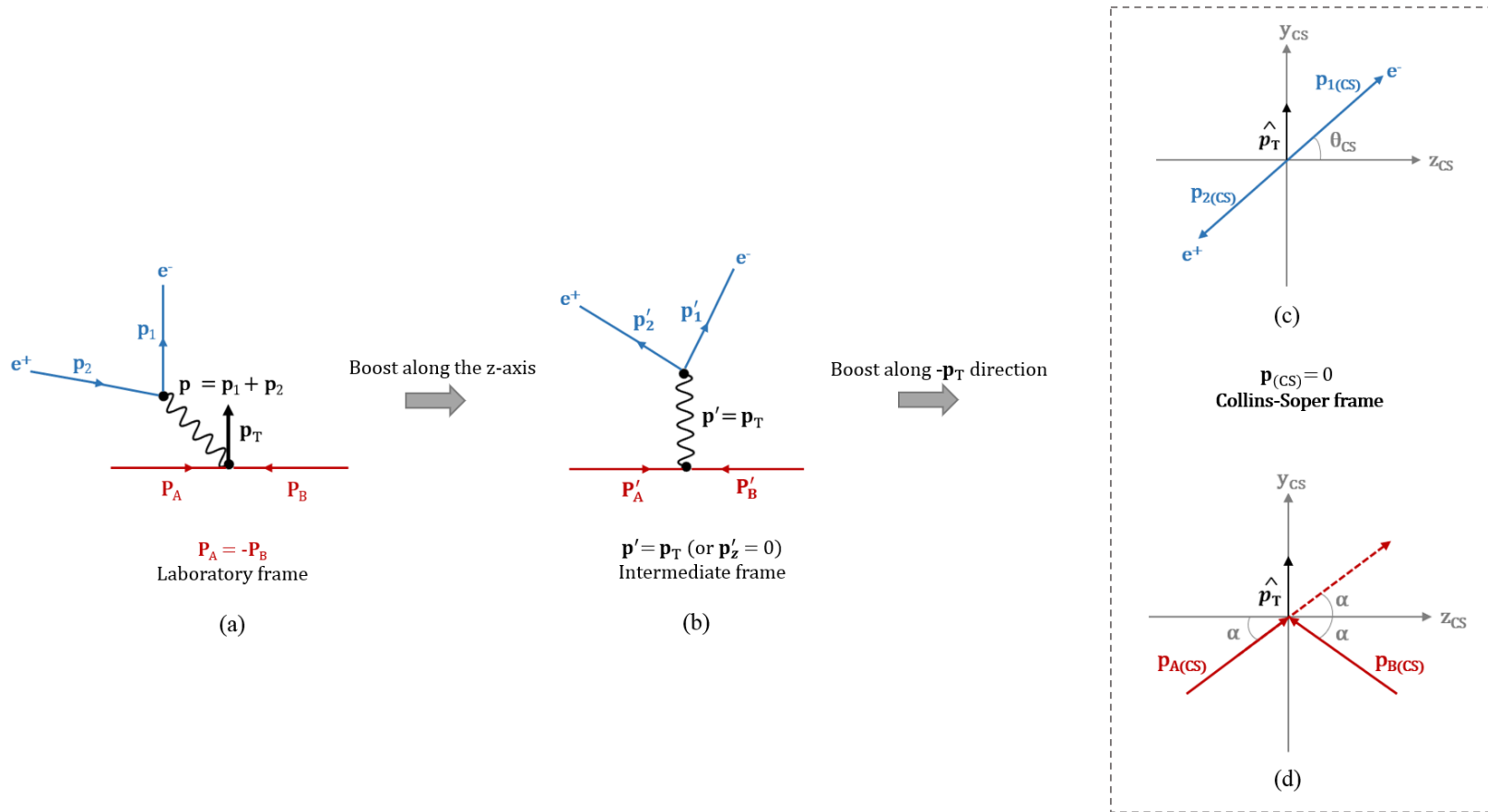


Figure 10.5: An illustration of the transition from the laboratory frame to the Collins-Soper frame is given. The laboratory frame is shown in (a) and the colliding protons are denoted by P_A and P_B . Boosting the laboratory frame along the z direction results in an intermediate reference frame, as represented in (b). This intermediate frame is again boosted in the direction of $-p_T$ to reach the Collins-Soper frame, shown in (c) and (d).

Chapter 11

Results

This chapter presents the results of the measured cosine of the polar angle of the di-electron system in the Collins-Soper frame, see Equation 10.3, to study the spin of the Z boson. It is clear from the previous chapter that the spin of the Z particle is manifested in the distribution of its decay electrons. The measurement of the polar angle in the Collins-Soper frame carefully preserves the spin information of the Z boson due to the Lorentz invariant nature of the variables defining the polar angle. As this thesis presents only a preliminary study of the spin measurement, only the shape of the electron distribution is considered. The observed distribution of the di-electrons in the data is compared with the MC predictions for distributions originating from spin 0, 1 or 2 parent Z particles.

The MC sample used for spin 1 parent particle is the same as used for cross-section measurement. Spin 0 and spin 2 samples have been generated using PYTHIA by retaining all the properties of a $Z \rightarrow e^+e^-$ decay but with the spin altered. The analysis employs all the selection cuts mentioned in Chapter 7 with an additional criterion of choosing events

where the reconstructed Z has a p_T less than 20 GeV, which is 67% of the events used in cross-section measurement [see Figure 8.7b]. This is to avoid the generator dependencies of higher order corrections at high p_T .

The di-electron distribution in the data compared with the predictions for spin 0, 1 and 2 samples are given respectively in Figures 11.1, 11.2 and 11.3. It is evident that the data shows the best agreement with the predictions for a spin 1 nature of the Z boson.

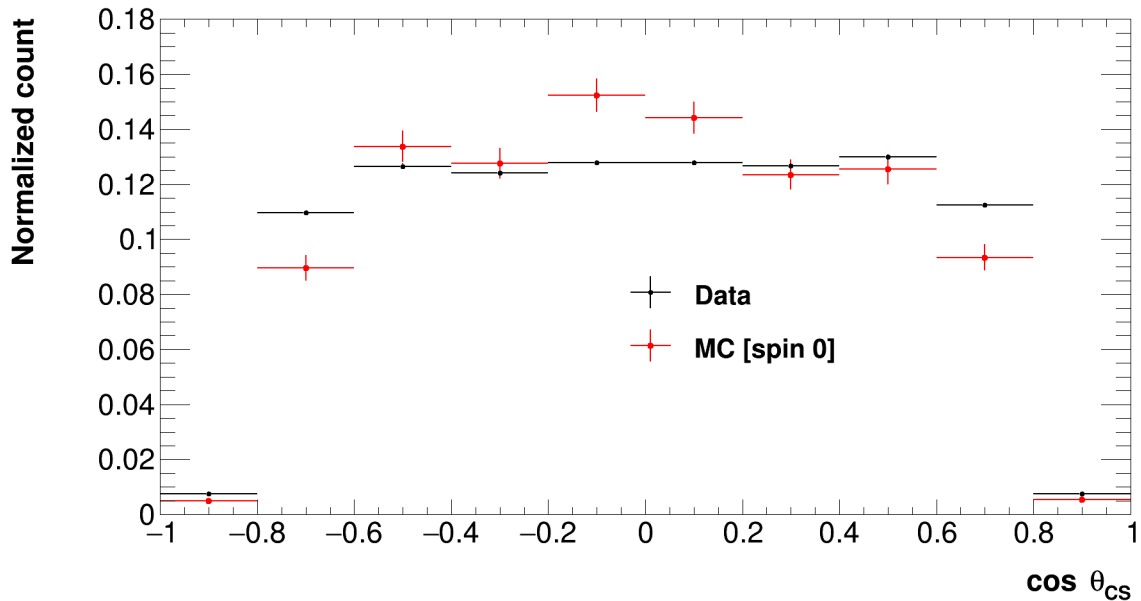


Figure 11.1: The measured $\cos \theta$ of the di-electron system in the CS frame originating from a reconstructed Z boson is plotted and compared with the MC. The observed data is denoted in black and the MC is given in red. The MC describes the expected $\cos \theta$ if the electrons emerge from a hypothetical “spin 0 Z boson”. The area enclosed by both the data and the MC are normalized to unity for shape comparison. The observed measurement and the MC do not agree, remaining outside the statistical uncertainties.

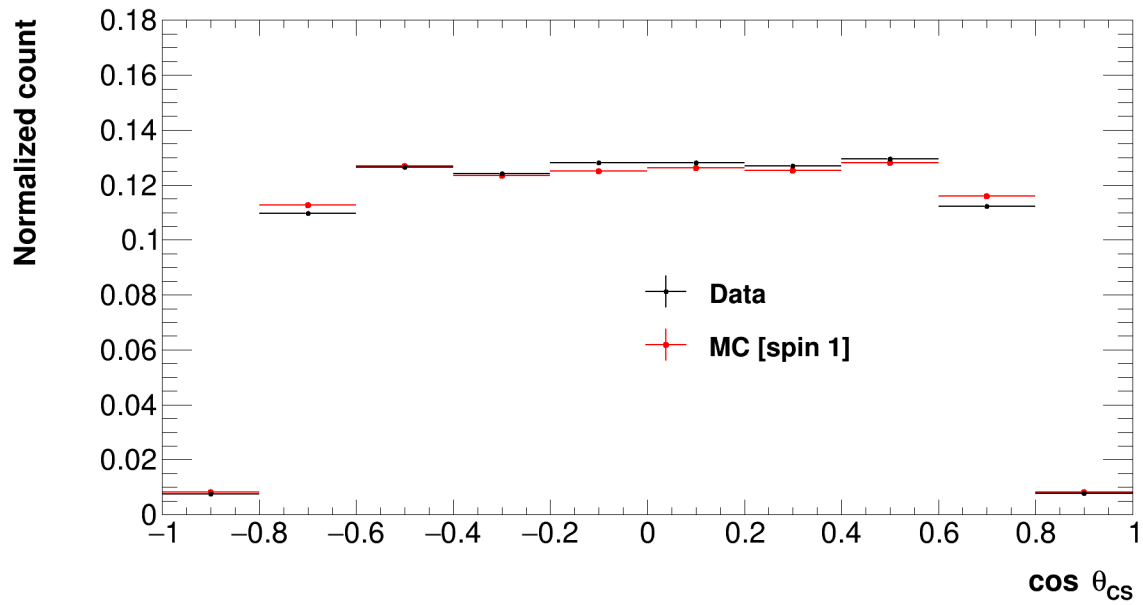


Figure 11.2: The measured $\cos \theta$ of the di-electron system in the CS frame originating from a reconstructed Z boson is plotted and compared with the MC. The observed data is denoted in black and the MC is given in red. The MC describes the expected $\cos \theta$ for the electrons emerging from a spin 1 Z boson according to the predictions of the Standard Model. The area enclosed by both the data and the MC are normalized to unity for shape comparison. The observed measurement and the SM prediction show fairly good agreement.

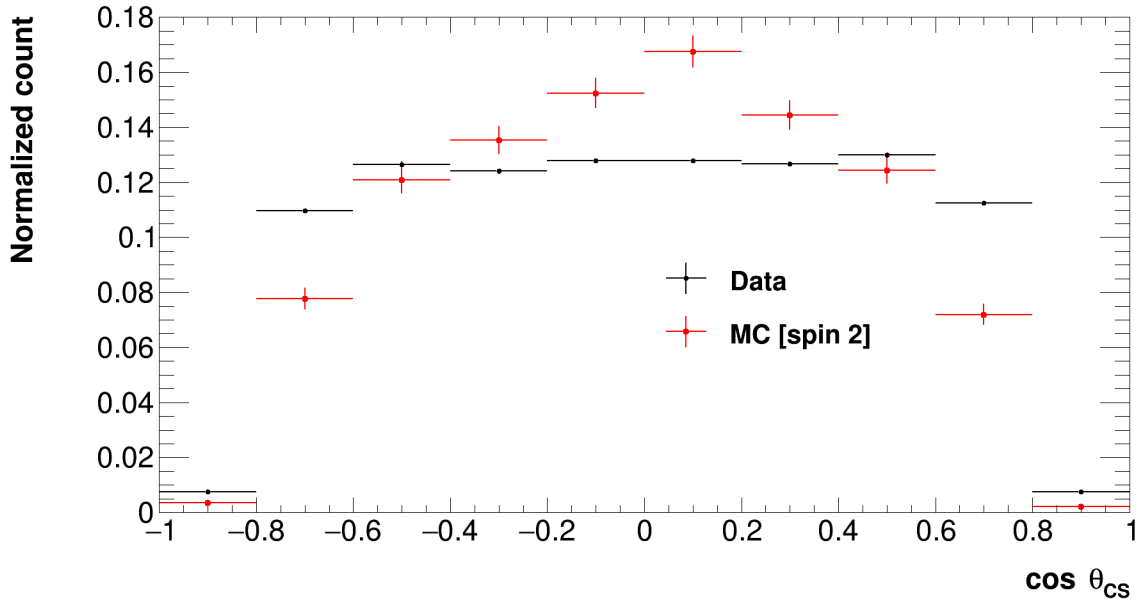


Figure 11.3: The measured $\cos \theta$ of the di-electron system in the CS frame originating from a reconstructed Z boson from the data (in black) is compared with the MC (in red). The MC describes the expected $\cos \theta$ for the electrons emerging from a hypothetical “spin 2 Z boson”. The area enclosed by both the data and the MC are normalized to unity for shape comparison. The observed measurement and the MC show significant deviations, ruling out a spin of 2 for the Z boson.

Statistical Test

To understand the statistical agreement between the data and the prediction for each spin nature, a simple chi-squared test, according to Equation 11.1, is also performed on the $\cos \theta_{(CS)}$ distributions seen in Figures 11.1-11.3 and the results are recorded in Table 11.1. For this comparison, the respective MC samples are arbitrarily normalized to 3000 events. The value of the reduced χ^2 confirms the agreement of the observed data with a Z spin of 1.

$$\chi^2 = \sum \left(\frac{Data - MC}{Error\ on\ MC} \right)^2 \quad (11.1)$$

Predicted spin of the Z boson	Reduced χ^2
Spin 0	7.9
Spin 1	1.7
Spin 2	39.0

Table 11.1: The results of the chi-squared test on the $\cos\theta_{(\text{CS})}$ distributions between the observed data and the MC samples for spin 0, 1 and 2 are tabulated.

Summary

The distribution of the electron-positron pair originating from the reconstructed Z boson is studied in the fiducial phase space. The observed distribution agrees fairly well for a Z spin of 1, as predicted by the Standard Model. The data demonstrates relatively large deviations from the predictions for spin 0 or 2, thus ruling them out. It has to be noted that the spin measurement presented in this thesis is a preliminary measurement and was done as an extension to the cross-section studies. Therefore, higher order corrections and uncertainties are not considered.

Part IV

Summary

Chapter 12

Conclusion and Outlook

This thesis presents the results of the measurement of the total and the differential production cross-sections of the Z boson in the di-electron channel at the LHC as well as the determination of the spin of the particle. The analysis uses 6.1 fb^{-1} proton-proton collision data collected by ATLAS in October 2016. The results of the study using events with exactly two electrons are presented and the measurements agree with the predictions of the Standard Model.

In the first analysis, the total production cross-section of the Z boson is measured to be $1.878 \pm 0.02 \text{ (stat)} \begin{smallmatrix} +0.045 \\ -0.052 \end{smallmatrix} \text{ (syst)} \pm 0.042 \text{ (lumi)} \text{ nb}$ and agrees with the predicted value of 1.901 nb within uncertainties. The differential cross-sections studied as functions of the transverse momentum and the rapidity also exhibit good agreement with the predictions. One can retrieve the total cross-section from the transverse momentum distribution but the entire phase space information is not available from the rapidity distribution as part of the information is lost at the reconstruction level. The data can be unfolded only up to $|y| < 2.5$

and the cross-section measured in this rapidity range is 1.31 nb. An estimate of the total cross-section is also made, to check the consistency of the results, by extrapolating into the higher missing phase space using only MC information. The estimated cross-section of 1.87 nb matches fairly well with the measured as well as the predicted values.

In the second analysis, the angular distribution of the electron-positron pair is studied in the Collins-Soper frame to determine the spin of the Z particle. The observed distribution matches fairly well with the expectations for a Z spin of 1, in accordance with the Standard Model, and is in clear disagreement with spin values of 0 and 2.

This thesis work could be extended to make further measurements as well. The cross-section measurement can also be performed in the muon channel, for combined results from both the electron and the muon channels. The ratio of the cross-sections in the two channels can test the validity of lepton universality in the Standard Model. The latest Z production cross-section studies at ATLAS and tests of the Standard Model can be found in [81]. Other decay channels of the Z particle are experimentally more challenging for precision measurements.

With the knowledge of Z production, the presented approach of spin measurement could be extrapolated to evaluate the complete set of angular coefficients of the Z boson, a key to investigate the underlying QCD dynamics of Z production. Measurements have been made previously in ATLAS with 8 TeV data from proton-proton collisions [95]. From the angular coefficients, one can verify the spin of the gluon [96] from the Lam-Tung [97–99] relation

which holds true up to NLO. At higher orders, the relation breaks which serves as a tool to probe the transverse momentum of partons [100].

Appendix A

Systematic uncertainty associated with electrons on the di-electron invariant mass

A graphic illustration of the effect of the systematic uncertainties associated with electrons on the reconstructed invariant mass of the di-electron system [refer to Section 9.1.1] is shown in Figures A.1-A.6.

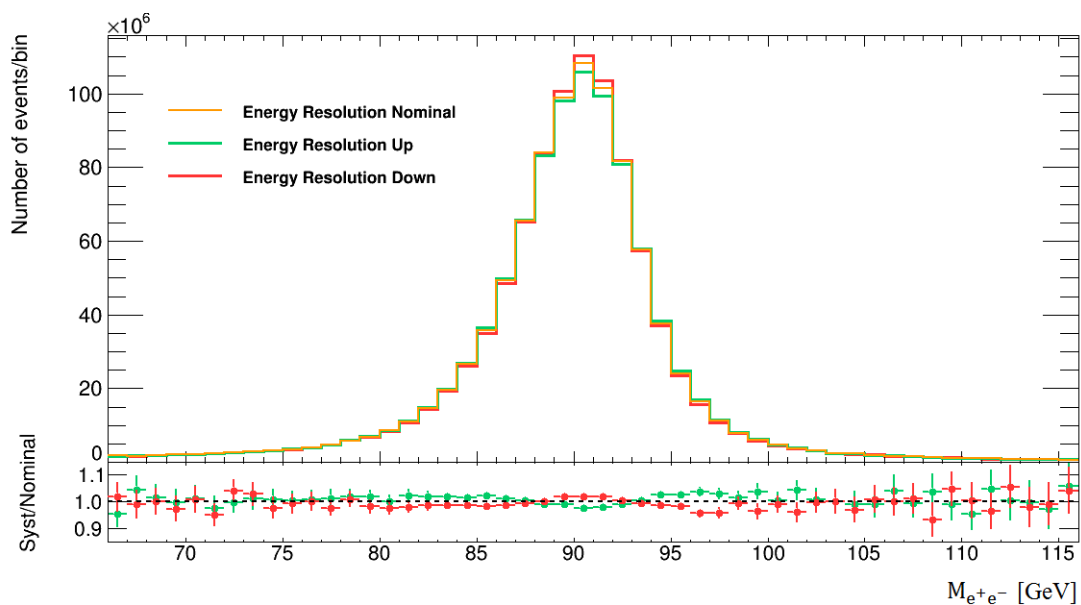


Figure A.1: Energy Resolution

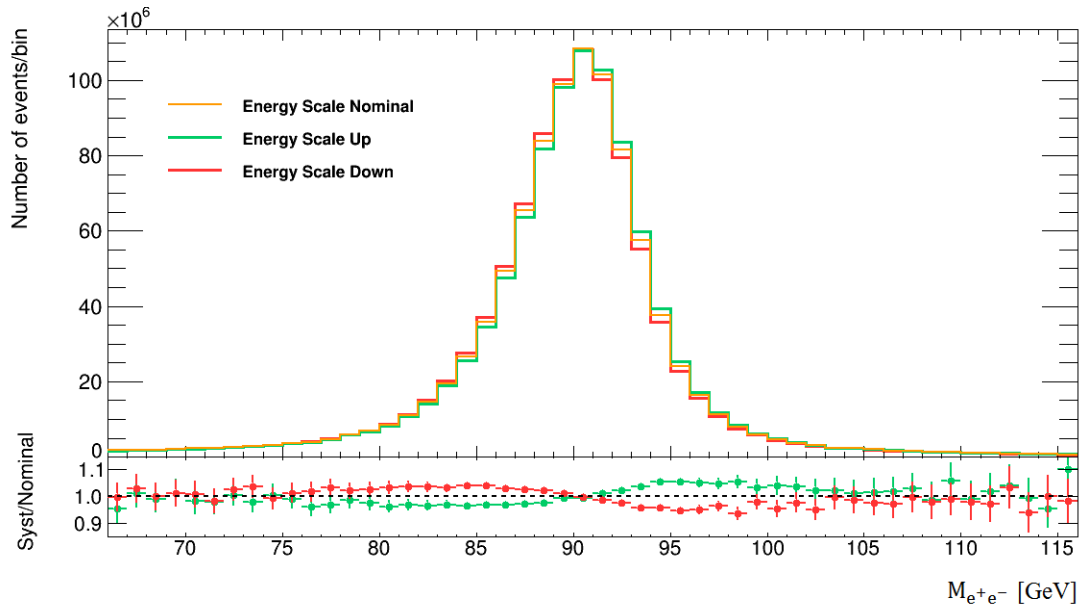


Figure A.2: Energy Scale

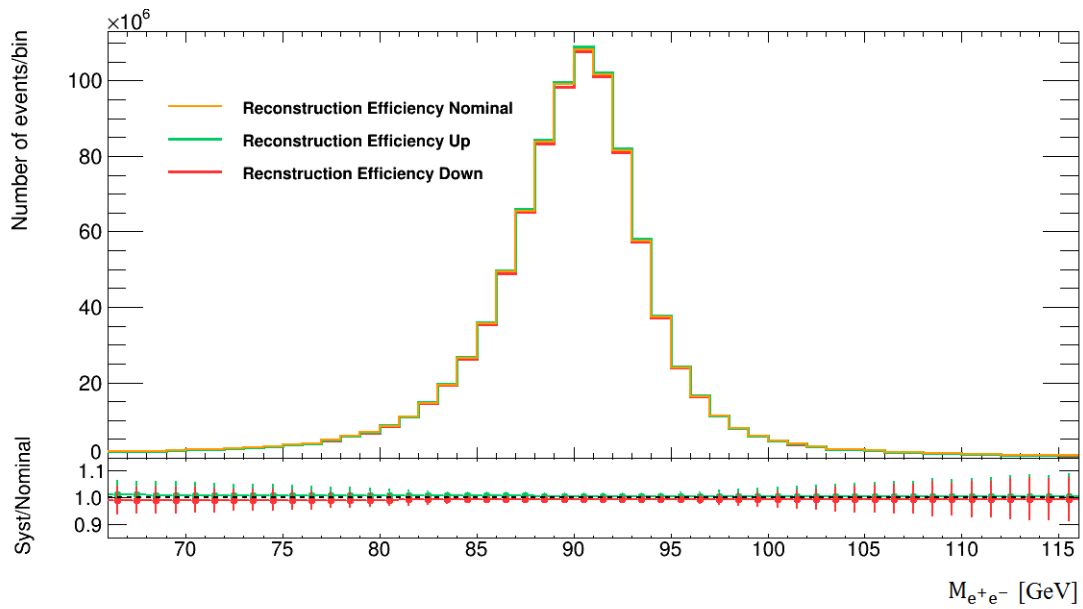


Figure A.3: Reconstruction Efficiency

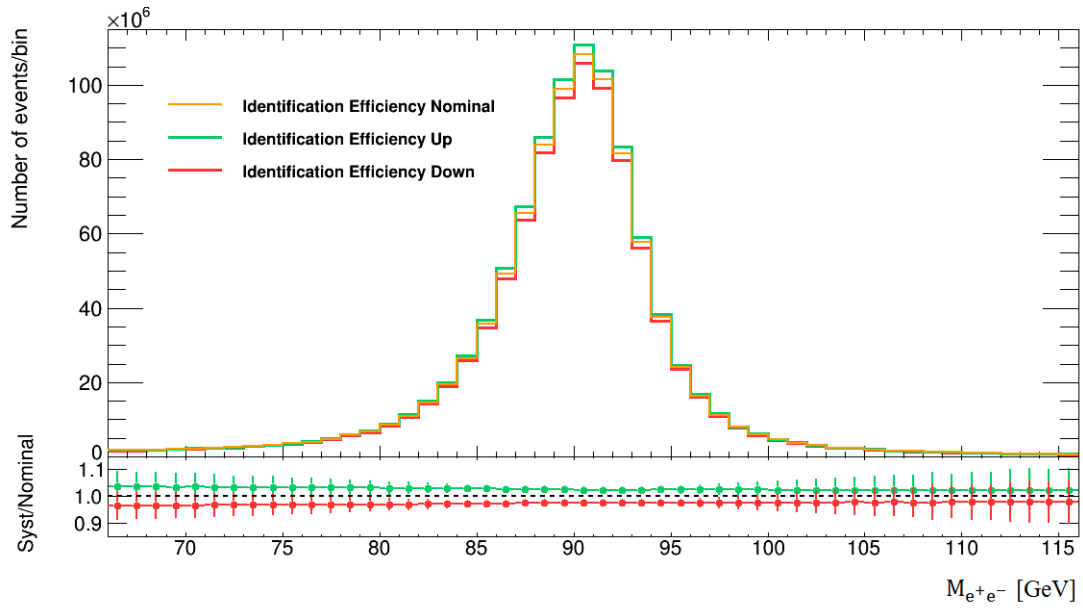


Figure A.4: Identification Efficiency

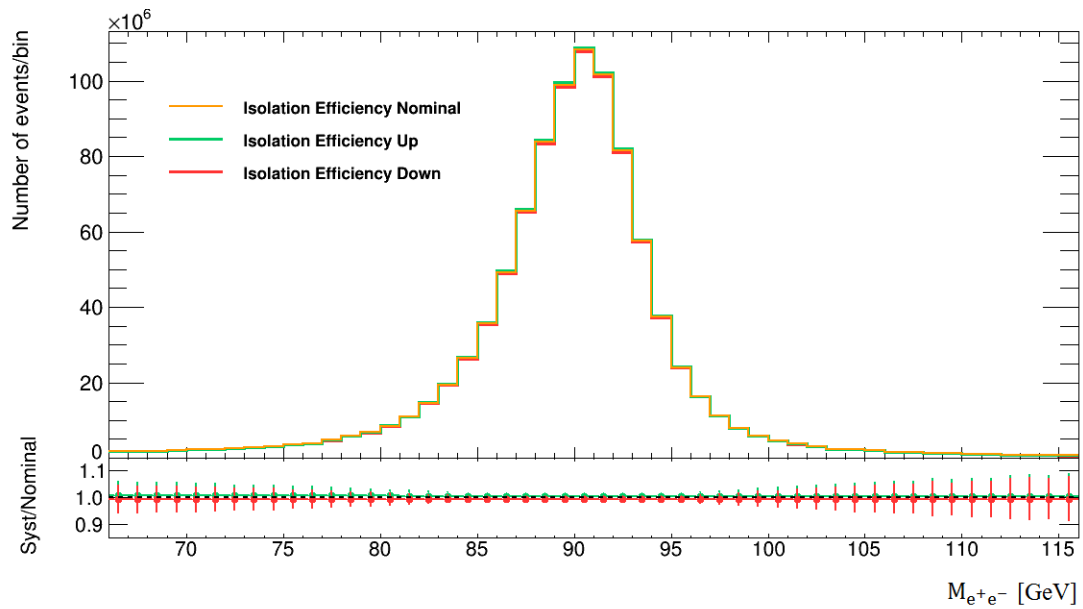


Figure A.5: Isolation Efficiency

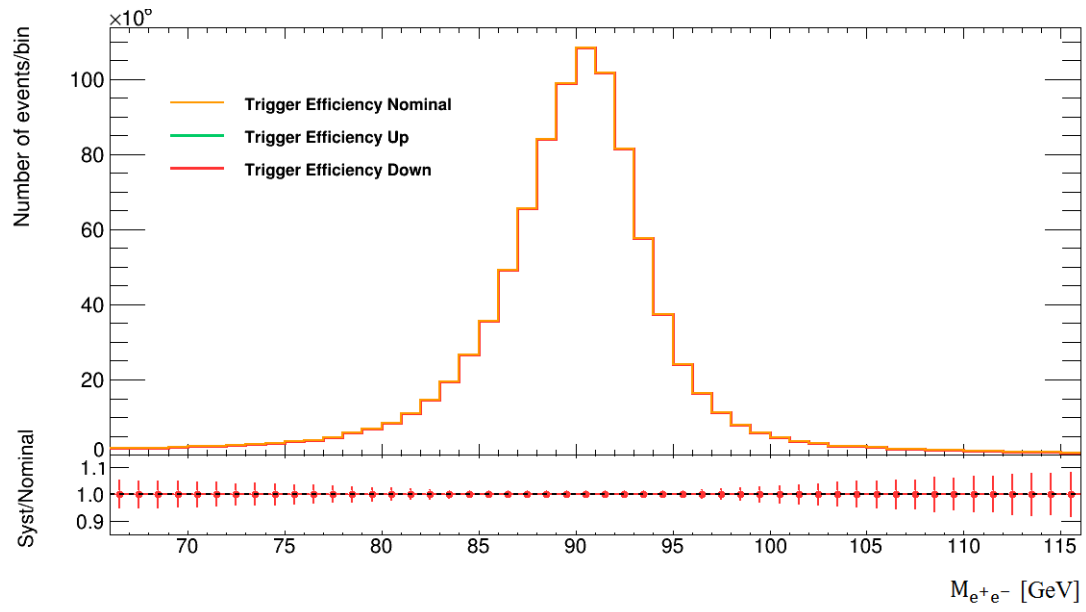


Figure A.6: Trigger Efficiency

Appendix B

Comparison with the previous results

The production cross-section of the Z boson measured differentially as a function of its transverse momentum [see Section 9.2.1] is compared with the Run I results from the ATLAS and the CMS experiments in Figure B.1. Figure B.2 compares the differential cross-section as a function of the rapidity of the Z boson [see Section 9.2.2]. The ATLAS and the CMS results presented are performed at $\sqrt{s} = 7$ TeV with the proton-proton collision data recorded in 2011 and 2010 respectively.

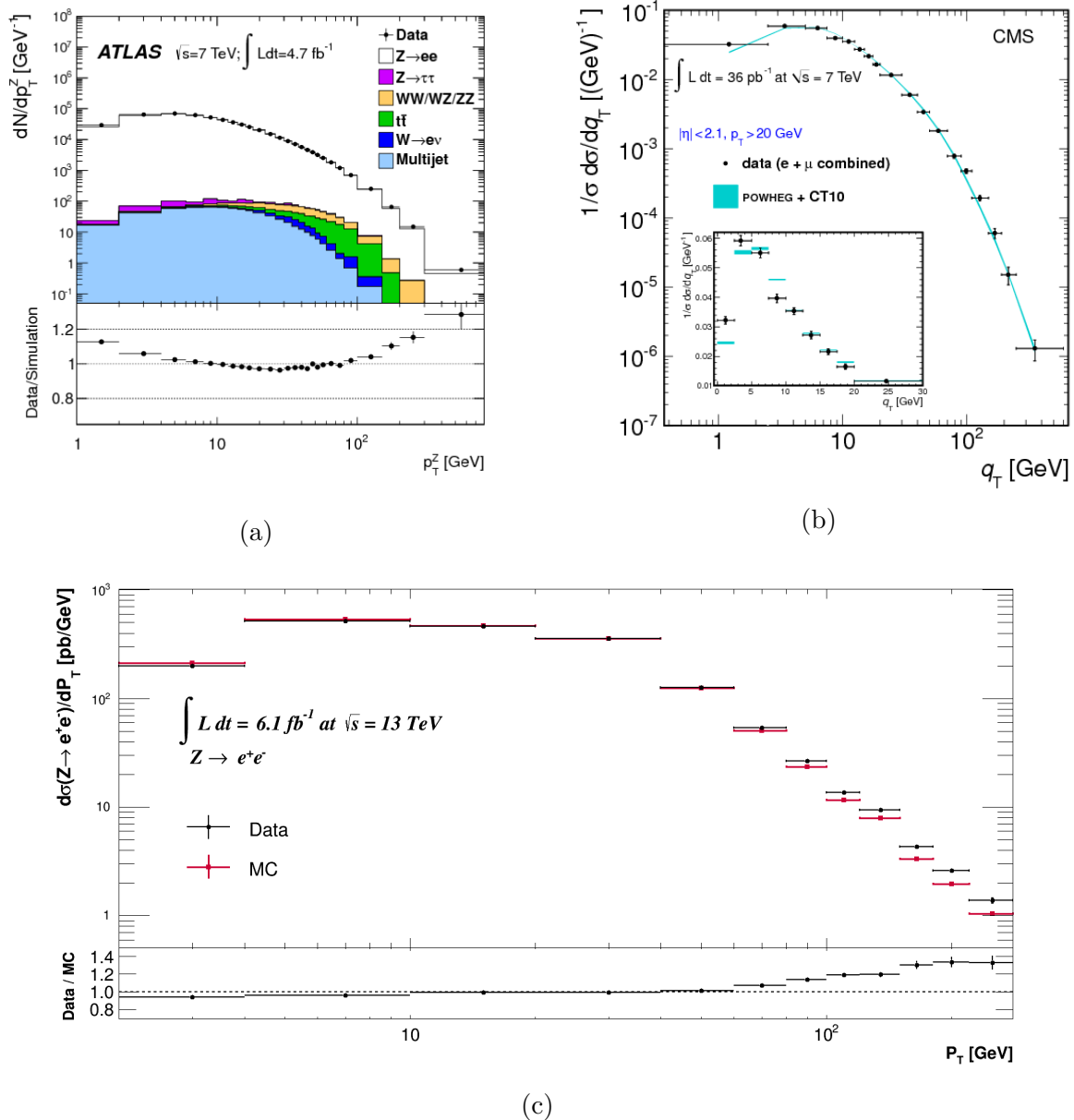


Figure B.1: The differential production cross-section of the Z boson as a function of its transverse momentum is shown. The ATLAS measurement [101] made with $\sqrt{s} = 7$ TeV at 4.7 fb $^{-1}$ is given in (a) and the CMS measurement [92] with $\sqrt{s} = 7$ TeV at 36 pb $^{-1}$ is given in (b). The ATLAS and the CMS measurements given are for the electron and the muon channels combined. (c) shows the measurement made in this analysis (with $\sqrt{s} = 13$ TeV at 6.1 fb $^{-1}$) on logarithmic scales for comparison with (a) and (b). The data in this figure is the same as in Figure 9.1 in Section 9.2.1 but with the scales changed.

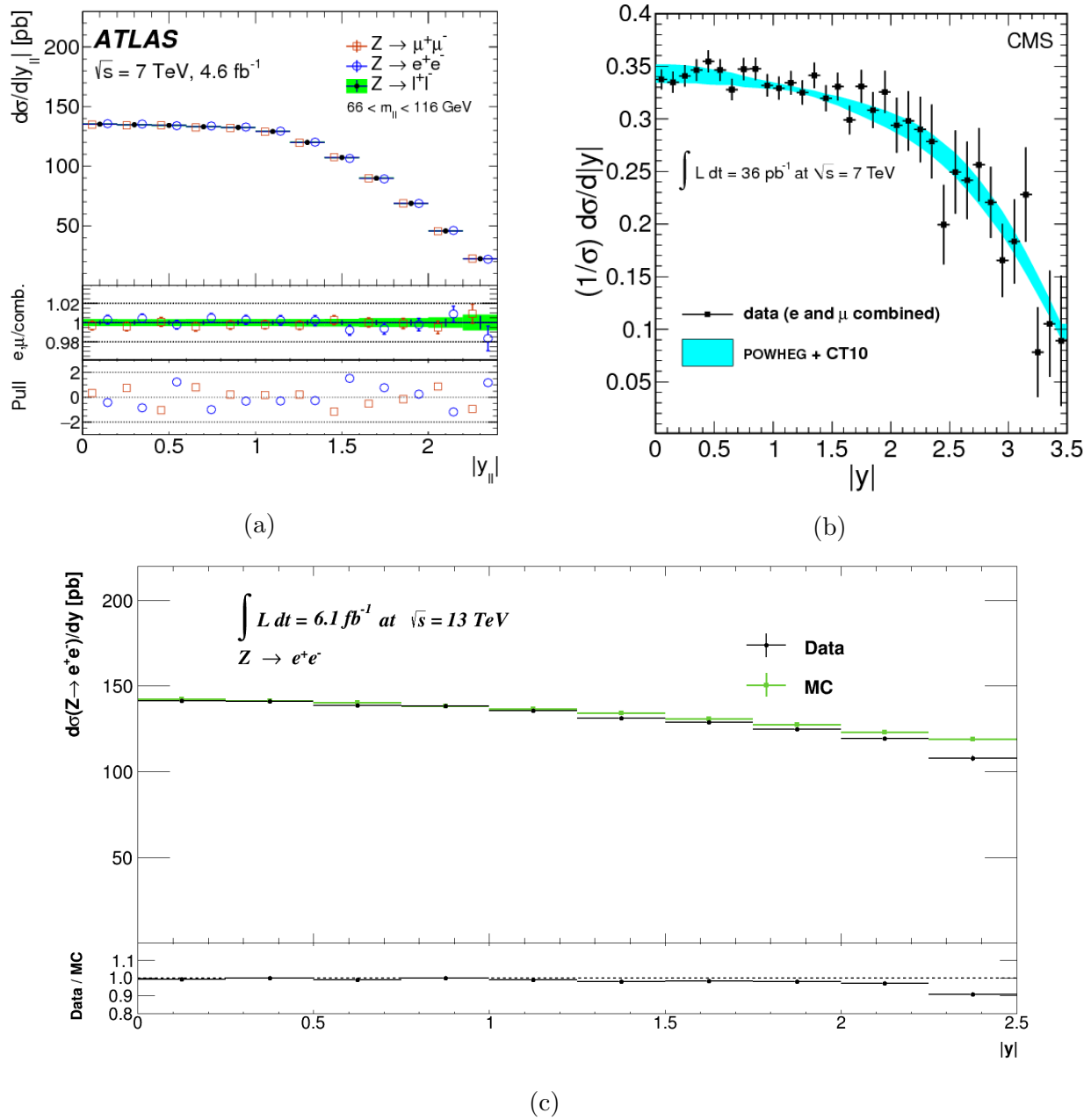


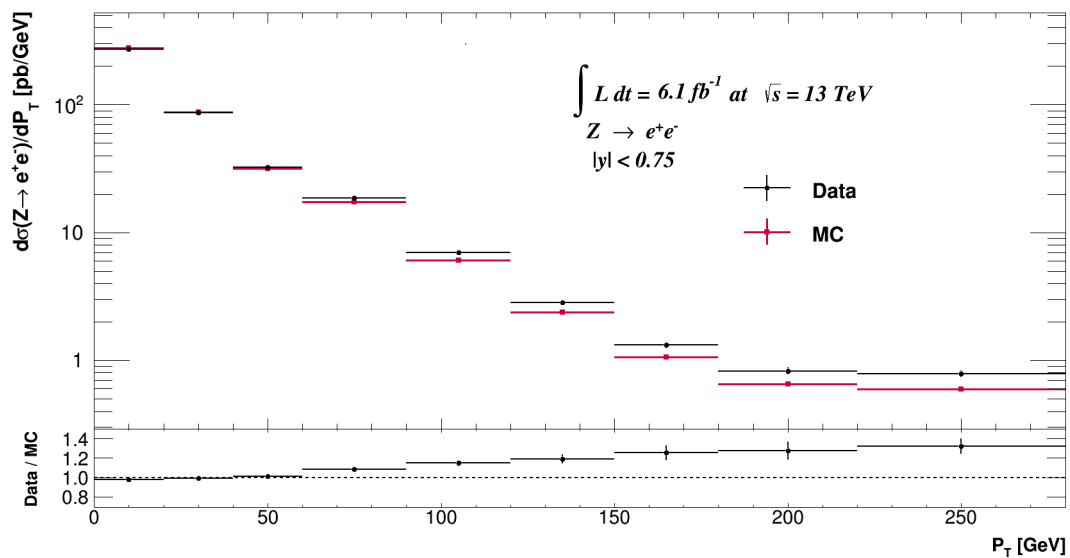
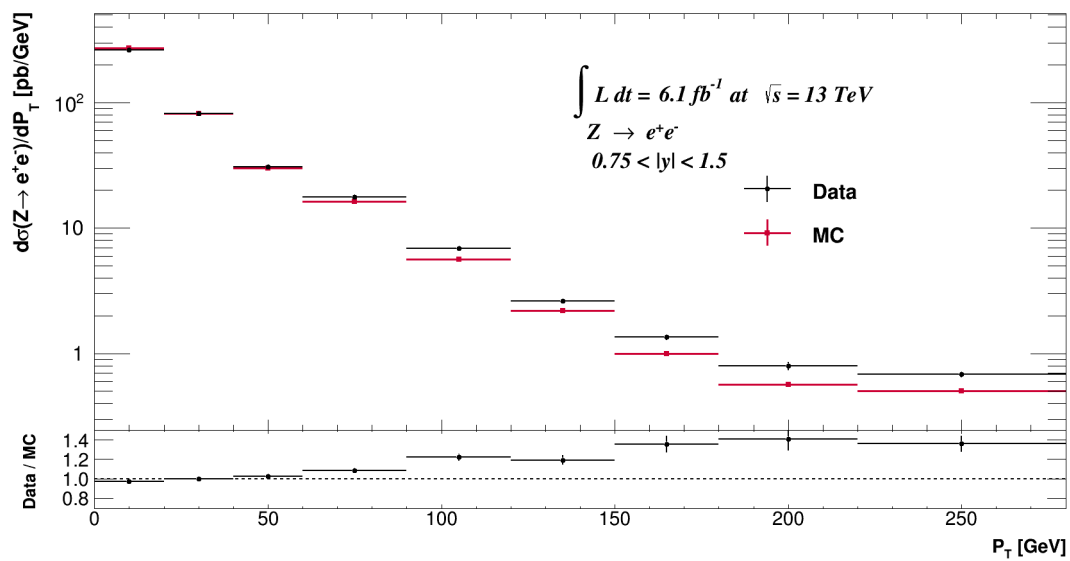
Figure B.2: The differential cross-section of the Z boson as a function of its rapidity is shown. The ATLAS measurement [91] with $\sqrt{s} = 7$ TeV at 4.6 fb^{-1} is given in (a) and the CMS measurement [92] with $\sqrt{s} = 7$ TeV at 36 pb^{-1} is given in (b). The ATLAS and the CMS measurements given are for the electron and the muon channels combined. (c) shows the measurement made in this analysis (with $\sqrt{s} = 13$ TeV at 6.1 fb^{-1}) on linear scales for comparison with (a) and (b). The data in this figure is the same as in Figure 9.5 in Section 9.2.2 but with the scales changed

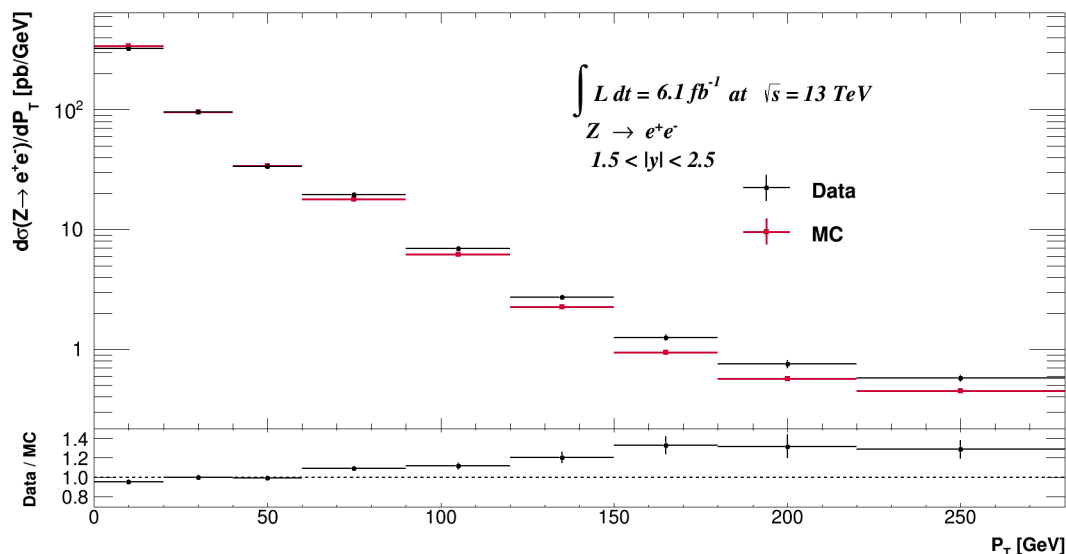
Appendix C

Double differential cross-section of Z boson production

Cross-section measured differentially as a function of transverse momentum in different ranges of rapidity [refer to Section 9.2.1]:

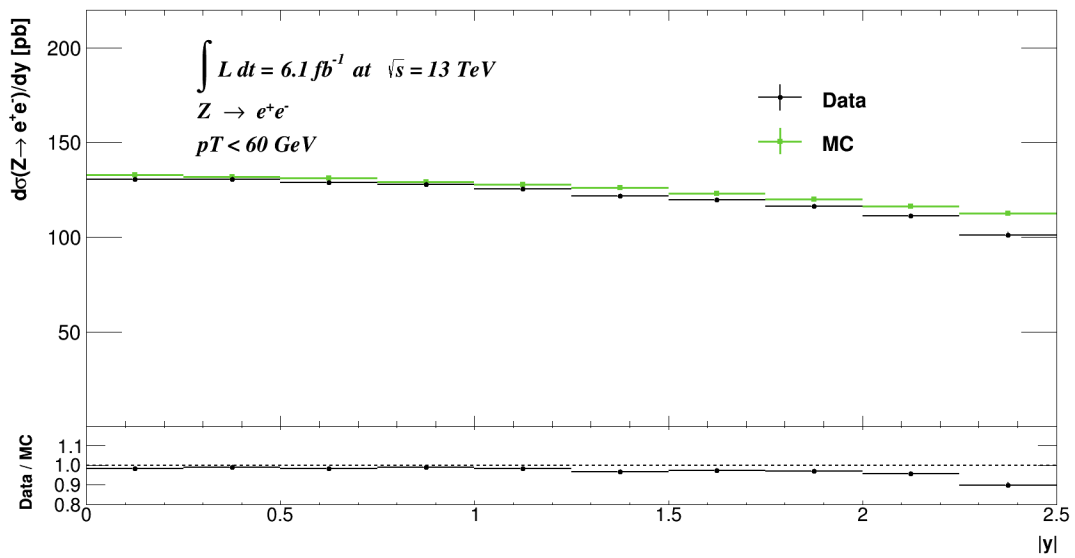
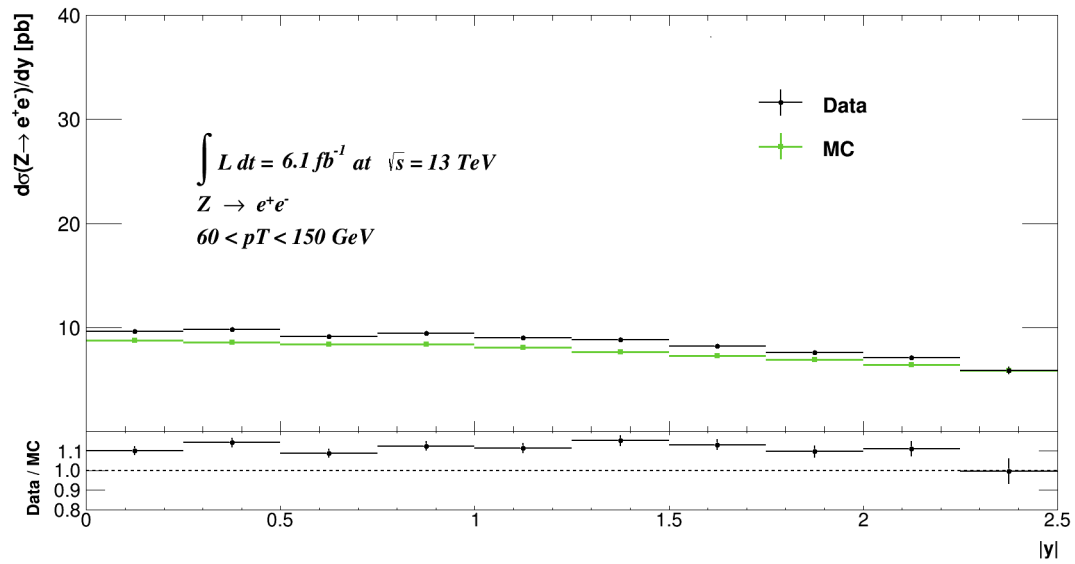
The differential production cross-section of the Z boson as a function of its transverse momentum in different slices of its rapidity is shown in Figures C.1-C.3. One can notice that the distribution is roughly independent of rapidity. The data exhibits a higher cross-section than the prediction at large transverse momenta as the MC is generated only at NLO.

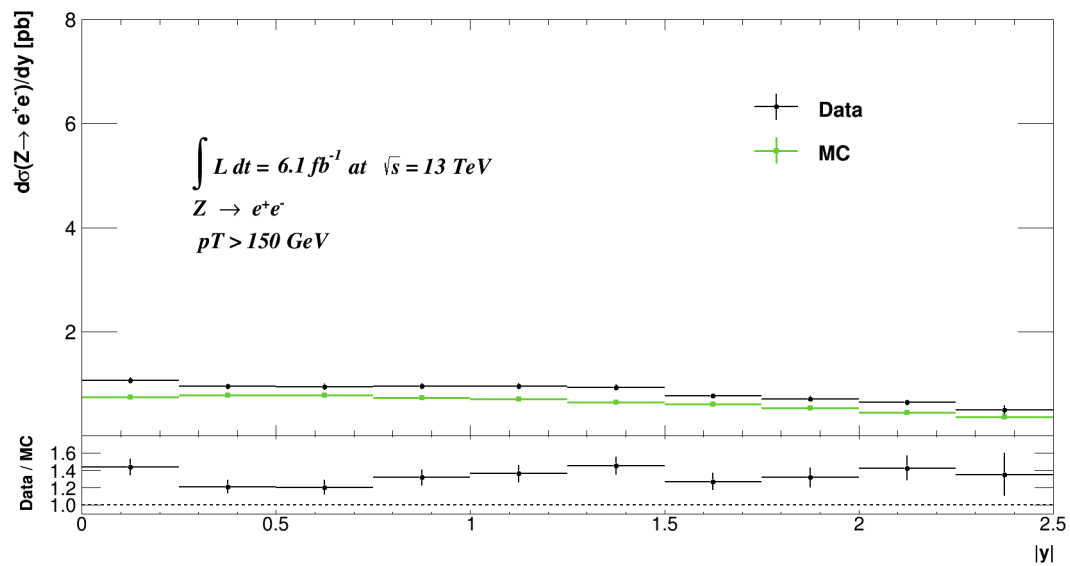
Figure C.1: For $|y| < 0.75$ Figure C.2: For $0.75 < |y| < 1.5$

Figure C.3: For $1.5 < |y| < 2.5$

Cross-section measured differentially as a function of rapidity in different ranges of transverse momentum [refer to Section 9.2.2]:

Figures C.4-C.6 show the cross-section as a function of the rapidity of the Z boson in different slices of its transverse momentum. The distribution exhibits a strong dependence on the transverse momentum of the Z particle. Clearly, the cross-section is the highest at low transverse momenta and falls considerably with increasing values. A higher cross-section is predicted at low transverse momenta which is consistent with Figure C.1 and the disagreement widens with increasing rapidities. But with increasing transverse momenta, the agreement between the prediction and the data improves at large rapidities.

Figure C.4: For $p_T < 60 \text{ GeV}$ Figure C.5: For $60 < p_T < 150 \text{ GeV}$

Figure C.6: For $p_T > 150 \text{ GeV}$

Appendix D

Toy example to illustrate the unrepresented phase space

Consider 100 generated Z boson events. Let the events be binned as functions of transverse momentum and rapidity, each in two bins as shown below.

	Bin 1	Bin 2		Bin 1	Bin 2
Number of generated events	50	50	Number of generated events	50	50
	Transverse momentum			Rapidity	

Assume that only 50 out of the 100 generated events pass acceptance (or numerator of the acceptance factor), such that the number of events in each bin is now as follows. Note that, at this point, one enters the regime of fiducial phase space.

	Bin 1	Bin 2		Bin 1	Bin 2
Number of events passing acceptance	25	25	Number of events passing acceptance	50	0
	Transverse momentum			Rapidity	

Recall that the acceptance factor is the fraction of events that pass the detector acceptance, which when shown as a function of the variables used is:

	Bin 1	Bin 2
Acceptance factor	0.5	0.5
	Transverse momentum	

	Bin 1	Bin 2
Acceptance factor	1	0
	Rapidity	

Again, to retrieve the total number of generated events or to extrapolate the information at the fiducial space space to the total phase space, the number of events passing acceptance is divided by the acceptance factor bin-by-bin.

	Bin 1	Bin 2
Number of events	50	50
	Transverse momentum	
	Number of events = 50 + 50 = 100	

	Bin 1	Bin 2
Number of events	50	undefined
	Rapidity	
	Number of events = 50 + undefined = undefined	

This is exactly what is happening to the differential cross-section of the Z boson studied as functions of its transverse momentum and rapidity [see Sections 9.2.1 and 9.2.2]. When cross-section is measured as a function of p_T , one can get the total cross-section when the fiducial cross-section is extrapolated to the entire phase space. But in the case of differential cross-section plotted as a function of the Z rapidity, total cross-section remains undefined. This is because the second bin in the example given for rapidity, where the acceptance is zero, corresponds to $|y| > 2.5$ for the reconstructed Z bosons. As a result, one cannot get the cross-section for Z production in this region due to “*missing*” information.

Glossary

ATLAS A Toroidal LHC ApparatuS. 2, 3, 4, 28, 30, 31, 35, 37, 38, 39, 41, 42, 43, 44, 45, 46, 48, 49, 52, 53, 56, 57, 58, 64, 65, 78, 82, 85, 89, 98, 99, 100, 109, 110, 116

BR Branching Ratio. 26, 78

BT Barrel toroid. 45

CERN European Organization for Nuclear Research. 2, 3, 12, 22, 30, 31

CMS Compact Muon Solenoid. 38, 85, 89, 116

CS Collins-Soper frame. 100, 104, 105

CSC Cathode Strip Chamber. 44

DY Drell-Yan. 22, 25

ECal Electromagnetic Calorimeter. 42, 43, 44, 72, 80

ECT End-cap toroid. 45

FCal Forward Calorimeter. 43, 44

FSR Final State Radiation. 17, 71

HCal Hadronic Calorimeter. 42, 43, 44

HEC Hadronic End-cap Calorimeter. 43

- HLT** High-level Trigger. 45, 46, 59, 60
- IBL** insertable B-layer. 41
- ID** Inner Detector. 41, 48
- ISR** Initial State Radiation. 17, 98
- L1** Level-1. 45, 46, 48
- LEP** Large Electron-Positron Collider. 3
- LHC** Large Hadron Collider. 2, 3, 4, 6, 16, 17, 18, 19, 21, 22, 24, 25, 26, 27, 30, 31, 32, 33, 34, 35, 38, 39, 45, 46, 67, 70, 78, 95, 109
- LO** Leading Order. 19, 25
- MC** Monte Carlo. 27, 28, 65, 69, 70, 71, 72, 75, 81, 82, 83, 85, 87, 89, 90, 91, 92, 103, 104, 105, 106, 109, 119
- MDT** Monitored Drift Tube. 44
- MS** Muon Spectrometer. 44
- NLO** Next-to-Leading Order. 19, 24, 25, 28, 82, 110, 119
- NNLO** Next-to-Next-Leading Order. 19, 24, 25
- PD** Pixel Detector. 41, 42
- PDF** Parton Distribution Function. 3, 16, 70, 82
- PDG** Particle Data Group. 67, 71, 72
- pQCD** Perturbative QCD. 19
- PU** Pile-Up. 35
- PV** Primary Vertex. 51

QCD Quantum Chromodynamics. 3, 10, 19, 24, 25, 110

QED Quantum Electrodynamics. 9, 10

RPC Resistive Plate Chamber. 44

SCT Semiconductor Tracker. 41, 42

SM Standard Model. 2, 3, 5, 6, 8, 9, 12, 104

SPS Super Proton Synchrotron. 22

TGC Thin Gap Chamber. 44

TRT Transition Radiation Tracker. 41, 42

References

- [1] S. Catani, L. Cieri, G. Ferrera, D. de Florian, and M. Grazzini, “Vector boson production at hadron colliders: a fully exclusive QCD calculation at NNLO,” *Phys. Rev. Lett.*, vol. 103, p. 082001, 2009.
- [2] R. Boughezal, A. Guffanti, F. Petriello, and M. Ubiali, “The impact of the LHC Z-boson transverse momentum data on PDF determinations,” *JHEP*, vol. 07, p. 130, 2017.
- [3] G. Aad *et al.*, “Observation of a new particle in the search for the Standard Model Higgs boson with the ATLAS detector at the LHC,” *Phys. Lett.*, vol. B716, pp. 1–29, 2012.
- [4] S. Chatrchyan *et al.*, “Observation of a new boson at a mass of 125 GeV with the CMS experiment at the LHC,” *Phys. Lett.*, vol. B716, pp. 30–61, 2012.
- [5] M. Krasny, F. Fayette, W. Płaczek, and A. Siodmok, “Z boson as the standard candle for high-precision W boson physics at LHC,” *The European Physical Journal C*, vol. 51, no. 3, pp. 607–617, 2007.
- [6] M. Aaboud, G. Aad, B. Abbott, J. Abdallah, O. Abdinov, B. Abeloos, S. Abidi, O. AbouZeid, N. Abraham, H. Abramowicz *et al.*, “Measurement of the W-boson

-
- mass in pp collisions at $\sqrt{s} = 7$ TeV with the ATLAS detector,” *The European Physical Journal C*, vol. 78, no. 2, p. 110, 2018.
- [7] C. Patrignani *et al.*, “Review of Particle Physics,” *Chin. Phys.*, vol. C40, no. 10, p. 100001, 2016.
- [8] C. Burgess and G. Moore, *The Standard Model: A Primer*. Cambridge University Press, 2006.
- [9] W. N. Cottingham and D. A. Greenwood, *An Introduction to the Standard Model of Particle Physics*. Cambridge University Press, 2007.
- [10] A. Purcell, “Go on a particle quest at the first CERN webfest. Le premier webfest du CERN se lance la conquête des particules,” no. BUL-NA-2012-269. 35/2012, p. 10, Aug 2012. [Online]. Available: <https://cds.cern.ch/record/1473657>
- [11] M. E. Peskin and D. V. Schroeder, *An Introduction to Quantum Field Theory*. Reading, USA: Addison-Wesley, 1995. [Online]. Available: <http://www.slac.stanford.edu/~mpeskin/QFT.html>
- [12] D. J. Gross and F. Wilczek, “Ultraviolet behavior of non-abelian gauge theories,” *Phys. Rev. Lett.*, vol. 30, pp. 1343–1346, Jun 1973. [Online]. Available: <https://link.aps.org/doi/10.1103/PhysRevLett.30.1343>
- [13] H. D. Politzer, “Reliable perturbative results for strong interactions?” *Phys. Rev. Lett.*, vol. 30, pp. 1346–1349, Jun 1973. [Online]. Available: <https://link.aps.org/doi/10.1103/PhysRevLett.30.1346>

-
- [14] S. L. Glashow, “Partial-symmetries of weak interactions,” *Nuclear Physics*, vol. 22, no. 4, pp. 579–588, 1961.
- [15] S. M. Bilenky and J. Hošek, “Glashow-Weinberg-Salam theory of electroweak interactions and the neutral currents,” *Physics Reports*, vol. 90, no. 2, pp. 73–157, 1982.
- [16] J. Goldstone, A. Salam, and S. Weinberg, “Broken symmetries,” *Phys. Rev.*, vol. 127, pp. 965–970, Aug 1962. [Online]. Available: <https://link.aps.org/doi/10.1103/PhysRev.127.965>
- [17] P. W. Higgs, “Broken symmetries and the masses of gauge bosons,” *Physical Review Letters*, vol. 13, no. 16, p. 508.
- [18] P. W. Higgs, “Broken symmetries, massless particles and gauge fields,” *Phys. Lett.*, vol. 12, pp. 132–133.
- [19] M. Banner *et al.*, “Observation of Single Isolated Electrons of High Transverse Momentum in Events with Missing Transverse Energy at the CERN anti-p p Collider,” *Phys. Lett.*, vol. B122, pp. 476–485, 1983, [,7.45(1983)].
- [20] G. Arnison *et al.*, “Experimental Observation of Lepton Pairs of Invariant Mass Around 95-GeV/c² at the CERN SPS Collider,” *Phys. Lett.*, vol. B126, pp. 398–410, 1983, [,7.55(1983)].
- [21] K. M. Ecker, H. Kroha, and S. Kortner, “Measurement of the Higgs boson tensor coupling in $H \rightarrow ZZ^* \rightarrow 4\ell$ decays with the ATLAS detector - How odd is the Higgs boson?” Apr 2018, presented 22 May 2018. [Online]. Available: <https://cds.cern.ch/record/2624277>

-
- [22] R. P. Feynman, “Very high-energy collisions of hadrons,” *Phys. Rev. Lett.*, vol. 23, pp. 1415–1417, Dec 1969. [Online]. Available: <https://link.aps.org/doi/10.1103/PhysRevLett.23.1415>
- [23] E. Perez and E. Rizvi, “The quark and gluon structure of the proton,” *Reports on Progress in Physics*, vol. 76, no. 4, p. 046201, 2013. [Online]. Available: <http://stacks.iop.org/0034-4885/76/i=4/a=046201>
- [24] S. Höche, “Introduction to parton-shower event generators,” in *Journeys Through the Precision Frontier: Amplitudes for Colliders: TASI 2014 Proceedings of the 2014 Theoretical Advanced Study Institute in Elementary Particle Physics*. World Scientific, 2016, pp. 235–295.
- [25] T. Han, “Collider phenomenology: Basic knowledge and techniques,” in *Physics in $D \geq 4$. Proceedings, Theoretical Advanced Study Institute in elementary particle physics, TASI 2004, Boulder, USA, June 6-July 2, 2004*, 2005, pp. 407–454.
- [26] G. F. Sterman, “QCD and jets,” in *Physics in $D \geq 4$. Proceedings, Theoretical Advanced Study Institute in elementary particle physics, TASI 2004, Boulder, USA, June 6-July 2, 2004*, 2004, pp. 67–145.
- [27] J. J. Sakurai, *Modern Quantum Mechanics; rev. ed.* Reading, MA: Addison-Wesley, 1994. [Online]. Available: <https://cds.cern.ch/record/1167961>
- [28] P. Bagnaia *et al.*, “Evidence for $Z^0 \rightarrow e^+ e^-$ at the CERN anti-p p Collider,” *Phys. Lett.*, vol. B129, pp. 130–140, 1983, [7.69(1983)].
- [29] C. Quigg, “Particle Physics after the Higgs-Boson Discovery: Opportunities for the Large Hadron Collider,” *Contemp. Phys.*, vol. 57, no. 2, pp. 177–187, 2016.

-
- [30] S. Farid, “Search for New Physics Beyond the Standard Model,” Master’s thesis, University of Cape Town, June 2016.
- [31] H. Ogul and K. Dilsiz, “Cross Section Prediction for Inclusive Production of Z Boson in pp Collisions at $\sqrt{s}= 14$ TeV: A Study of Systematic Uncertainty Due to Scale Dependence,” *Adv. High Energy Phys.*, vol. 2017, p. 8262018, 2017.
- [32] A. Buckley *et al.*, “General-purpose event generators for LHC physics,” *Phys. Rept.*, vol. 504, pp. 145–233, 2011.
- [33] S. Frixione, P. Nason, and C. Oleari, “Matching NLO QCD computations with Parton Shower simulations: the POWHEG method,” *JHEP*, vol. 11, p. 070, 2007.
- [34] T. Sjostrand, S. Mrenna, and P. Z. Skands, “A Brief Introduction to PYTHIA 8.1,” *Comput. Phys. Commun.*, vol. 178, pp. 852–867, 2008.
- [35] G. Aad *et al.*, “The ATLAS Simulation Infrastructure,” *Eur. Phys. J.*, vol. C70, pp. 823–874, 2010.
- [36] E. Mobs, “The CERN accelerator complex. Complexe des accelrateurs du CERN,” Jul 2016, general Photo. [Online]. Available: <https://cds.cern.ch/record/2197559>
- [37] X. C. Vidal and R. C. Manzano, “Taking a closer look at LHC,” 2014. [Online]. Available: https://www.lhc-closer.es/taking_a_closer_look_at_lhc/0.lorentz_force
- [38] L. Rossi, “The LHC superconducting magnets,” in *Proceedings of the 2003 Particle Accelerator Conference*, vol. 1, May 2003, pp. 141–145.

-
- [39] O. S. Brning, P. Collier, P. Lebrun, S. Myers, R. Ostojic, J. Poole, and P. Proudlock, *LHC Design Report*, ser. CERN Yellow Reports: Monographs. Geneva: CERN, 2004. [Online]. Available: <https://cds.cern.ch/record/782076>
- [40] X. C. Vidal and R. C. Manzano, “Taking a closer look at LHC,” 2014. [Online]. Available: https://www.lhc-closer.es/taking_a_closer_look_at_lhc/0.magnetic_multipoles
- [41] A. Hoecker, “Physics at the LHC Run-2 and Beyond,” in *Proceedings, 2016 European School of High-Energy Physics (ESHEP2016): Skeikampen, Norway, June 15-28 2016*, 2016.
- [42] “Luminosity Public Results Run2.” [Online]. Available: <https://twiki.cern.ch/twiki/bin/view/AtlasPublic/LuminosityPublicResultsRun2>
- [43] “ATLAS: letter of intent for a general-purpose pp experiment at the large hadron collider at CERN,” 1992. [Online]. Available: <https://cds.cern.ch/record/291061>
- [44] A. Airapetian *et al.*, “ATLAS: Detector and physics performance technical design report. Volume 1,” Tech. Rep. CERN-LHCC-99-14, ATLAS-TDR-14, 1999.
- [45] A. Airapetian *et al.*, “ATLAS: Detector and physics performance technical design report. Volume 2,” Tech. Rep. CERN-LHCC-99-15, ATLAS-TDR-15, 1999.
- [46] G. Aad, J. Butterworth, J. Thion, U. Bratzler, P. Ratoff, R. Nickerson, J. Seixas, I. Grabowska-Bold, F. Meisel, S. Lokwitz *et al.*, “The ATLAS experiment at the CERN large hadron collider,” *Jinst*, vol. 3, p. S08003, 2008.
- [47] S. Chatrchyan *et al.*, “The CMS Experiment at the CERN LHC,” *JINST*, vol. 3, p. S08004, 2008.

-
- [48] J. Pequenaó, “Computer generated image of the whole ATLAS detector,” Mar 2008. [Online]. Available: <https://cds.cern.ch/record/1095924>
- [49] D. Puldon, “Measurement of the WW and WZ production cross section in the semi-leptonic final state using $\sqrt{s} = 7$ TeV pp collisions with the ATLAS detector,” Ph.D. dissertation, State University of New York at Stony Brook, 2014.
- [50] M. S. Alam *et al.*, “ATLAS pixel detector: Technical design report,” Tech. Rep. CERN-LHCC-98-13, 1998.
- [51] G. Aad *et al.*, “ATLAS pixel detector electronics and sensors,” *JINST*, vol. 3, p. P07007, 2008.
- [52] M. Capeans, G. Darbo, K. Einsweiler, M. Elsing, T. Flick, M. Garcia-Sciveres, C. Gemme, H. Pernegger, O. Rohne, and R. Vuillermet, “ATLAS Insertable B-Layer Technical Design Report,” Tech. Rep. CERN-LHCC-2010-013. ATLAS-TDR-19, Sep 2010. [Online]. Available: <https://cds.cern.ch/record/1291633>
- [53] A. Abdesselam *et al.*, “The barrel modules of the ATLAS semiconductor tracker,” Tech. Rep. ATL-COM-INDET-2006-009, ATL-INDET-PUB-2006-005, 2006.
- [54] A. Abdesselam *et al.*, “The ATLAS semiconductor tracker end-cap module,” *Nucl. Instrum. Meth.*, vol. A575, pp. 353–389, 2007.
- [55] E. Abat *et al.*, “The ATLAS TRT barrel detector,” *JINST*, vol. 3, p. P02014, 2008.
- [56] E. Abat *et al.*, “The ATLAS TRT end-cap detectors,” *JINST*, vol. 3, p. P10003, 2008.
- [57] “ATLAS liquid argon calorimeter: Technical design report,” Tech. Rep. CERN-LHCC-96-41, 1996.

-
- [58] M. J. Varanda, “The tile hadronic calorimeter for the ATLAS experiment,” *IEEE Trans. Nucl. Sci.*, vol. 48, pp. 367–371, 2001.
- [59] D. M. Gingrich *et al.*, “Construction, assembly and testing of the ATLAS hadronic endcap calorimeter,” Tech. Rep. ATL-LARG-PUB-2007-009, ATL-COM-LARG-2007-006, 2007.
- [60] A. Artamonov *et al.*, “The ATLAS forward calorimeters,” *JINST*, vol. 3, p. P02010, 2008.
- [61] “ATLAS muon spectrometer: Technical design report,” Tech. Rep. CERN-LHCC-97-22, ATLAS-TDR-10, 1997.
- [62] “ATLAS magnet system: Technical design report,” Tech. Rep. CERN-LHCC-97-18, 1997.
- [63] “ATLAS central solenoid: Technical design report,” Tech. Rep. CERN-LHCC-97-21, 1997.
- [64] “ATLAS barrel toroid: Technical design report,” Tech. Rep. CERN-LHCC-97-19, 1997.
- [65] “ATLAS endcap toroids: Technical design report,” Tech. Rep. CERN-LHCC-97-20, 1997.
- [66] ATLAS Outreach, “ATLAS Fact Sheet: To raise awareness of the ATLAS detector and collaboration on the LHC,” 2010.
- [67] M. L. Dunford and P. Jenni, “The ATLAS experiment,” *Scholarpedia*, vol. 9, no. 10, p. 32147, 2014, revision #184627.

-
- [68] A. R. Martnez, “The Run-2 ATLAS Trigger System,” *J. Phys. Conf. Ser.*, vol. 762, no. 1, p. 012003, 2016.
- [69] “ATLAS first level trigger: Technical design report,” Tech. Rep. CERN-LHCC-98-14, ATLAS-TDR-12, 1998.
- [70] “ATLAS high-level trigger, data acquisition and controls: Technical design report,” Tech. Rep. CERN-LHCC-2003-022, ATLAS-TRD-016, 2003.
- [71] M. Aaboud *et al.*, “Performance of the ATLAS Trigger System in 2015,” *Eur. Phys. J.*, vol. C77, no. 5, p. 317, 2017.
- [72] S. D. Jones, “The ATLAS Electron and Photon Trigger,” CERN, Geneva, Tech. Rep. ATL-DAQ-PROC-2017-040, Oct 2017. [Online]. Available: <https://cds.cern.ch/record/2290123>
- [73] R. Fruhwirth, “Application of Kalman filtering to track and vertex fitting,” *Nucl. Instrum. Meth.*, vol. A262, no. HEPHY-PUB-87-503, pp. 444–450, 1987.
- [74] T. G. Cornelissen, M. Elsing, I. Gavrilenko, J. F. Laporte, W. Liebig, M. Limper, K. Nikolopoulos, A. Poppleton, and A. Salzburger, “The global χ^2 track fitter in ATLAS,” *J. Phys. Conf. Ser.*, vol. 119, p. 032013, 2008.
- [75] “Improved electron reconstruction in ATLAS using the Gaussian Sum Filter-based model for bremsstrahlung,” CERN, Geneva, Tech. Rep. ATLAS-CONF-2012-047, May 2012. [Online]. Available: <http://cds.cern.ch/record/1449796>

-
- [76] G. Tarna, “Electron identification with the ATLAS detector,” CERN, Geneva, Tech. Rep. ATL-PHYS-PROC-2017-173, Sep 2017. [Online]. Available: <https://cds.cern.ch/record/2286383>
- [77] F. Meloni, “Primary vertex reconstruction with the ATLAS detector,” *Journal of Instrumentation*, vol. 11, no. 12, p. C12060, 2016.
- [78] P. Wells, “Tracking at the LHC,” 2011. [Online]. Available: <https://indico.cern.ch/event/96989/contributions/2124495/attachments/1114189/1589705/WellsTracking.pdf>
- [79] W. Shen, J. Neyman, E. Pearson, G. Bolch, S. Greiner, H. de Meer, K. Trivedi, R. Sahnner, K. Trivedi, A. Puliafito *et al.*, “On the problem of the most efficient tests of statistical hypotheses,” *Interfaces*, vol. 48, no. 3, pp. 285–289, 2018.
- [80] “Electron efficiency measurements with the ATLAS detector using the 2015 LHC proton-proton collision data,” CERN, Geneva, Tech. Rep. ATLAS-CONF-2016-024, Jun 2016. [Online]. Available: <https://cds.cern.ch/record/2157687>
- [81] G. Aad *et al.*, “Measurement of W^\pm and Z -boson production cross sections in pp collisions at $\sqrt{s} = 13$ TeV with the ATLAS detector,” *Phys. Lett.*, vol. B759, pp. 601–621, 2016.
- [82] R. Avinery, “Particle Lifetime,” The Mossbauer Effect. [Online]. Available: https://m.tau.ac.il/~lab3/MOSSBAUER/Introduction/Particle_lifetime.html
- [83] G. Breit and E. Wigner, “Capture of slow neutrons,” *Physical review*, vol. 49, no. 7, p. 519, 1936.

-
- [84] W. Buttinger, “Using Event Weights to account for differences in Instantaneous Luminosity and Trigger Prescale in Monte Carlo and Data,” CERN, Geneva, Tech. Rep. ATL-COM-SOFT-2015-119, May 2015. [Online]. Available: <https://cds.cern.ch/record/2014726>
- [85] M. Oreglia, “A Study of the Reactions $\psi' \rightarrow \gamma\gamma\psi$,” Ph.D. dissertation, SLAC, 1980.
- [86] J. E. Gaiser, “Charmonium Spectroscopy From Radiative Decays of the J/ψ and ψ' ,” Ph.D. dissertation, SLAC, 1982.
- [87] M. Aaboud *et al.*, “Luminosity determination in pp collisions at $\sqrt{s} = 8$ TeV using the ATLAS detector at the LHC,” *Eur. Phys. J.*, vol. C76, no. 12, p. 653, 2016.
- [88] G. Avoni *et al.*, “The new LUCID-2 detector for luminosity measurement and monitoring in ATLAS,” *Journal of Instrumentation*, vol. 13, no. 07, p. P07017, 2018.
- [89] <https://ami.in2p3.fr/AMI/servlet/net.hep.atlas.Database.Bookkeeping.AMI.Servlet.Command>.
- [90] M. Aaboud *et al.*, “Measurements of the production cross section of a Z boson in association with jets in pp collisions at $\sqrt{s} = 13$ TeV with the ATLAS detector,” *Eur. Phys. J.*, vol. C77, no. 6, p. 361, 2017.
- [91] M. Aaboud *et al.*, “Precision measurement and interpretation of inclusive W^+ , W^- and Z/γ^* production cross sections with the ATLAS detector,” *Eur. Phys. J.*, vol. C77, no. 6, p. 367, 2017.

-
- [92] S. Chatrchyan *et al.*, “Measurement of the Rapidity and Transverse Momentum Distributions of Z Bosons in pp Collisions at $\sqrt{s} = 7$ TeV,” *Phys. Rev.*, vol. D85, p. 032002, 2012.
- [93] J. C. Collins and D. E. Soper, “Angular distribution of dileptons in high-energy hadron collisions,” *Phys. Rev. D*, vol. 16, pp. 2219–2225, Oct 1977. [Online]. Available: <https://link.aps.org/doi/10.1103/PhysRevD.16.2219>
- [94] Y. Nagashima, *Elementary particle physics: Foundations of the Standard Model*. John Wiley & Sons, 2013, vol. 2.
- [95] G. Aad *et al.*, “Measurement of the angular coefficients in Z -boson events using electron and muon pairs from data taken at $\sqrt{s} = 8$ TeV with the ATLAS detector,” *JHEP*, vol. 08, p. 159, 2016.
- [96] K. Schmieden and N. Wermes, “Measurement of the Weak Mixing Angle and the Spin of the Gluon from Angular Distributions in the Reaction $pp \rightarrow Z/\gamma^* + X \rightarrow \mu^+\mu^- + X$ with ATLAS,” Dec 2012, presented 22 Apr 2013. [Online]. Available: <https://cds.cern.ch/record/1566623>
- [97] C. S. Lam and W.-K. Tung, “Systematic approach to inclusive lepton pair production in hadronic collisions,” *Phys. Rev. D*, vol. 18, pp. 2447–2461, Oct 1978. [Online]. Available: <https://link.aps.org/doi/10.1103/PhysRevD.18.2447>
- [98] C. Lam and W.-K. Tung, “Structure function relations at large transverse momenta in lepton-pair production processes,” *Physics Letters B*, vol. 80, no. 3, pp. 228 – 231, 1979. [Online]. Available: <http://www.sciencedirect.com/science/article/pii/0370269379902041>

- [99] C. S. Lam and W.-K. Tung, “Parton-model relation without quantum-chromodynamic modifications in lepton pair production,” *Phys. Rev. D*, vol. 21, pp. 2712–2715, May 1980. [Online]. Available: <https://link.aps.org/doi/10.1103/PhysRevD.21.2712>
- [100] L. Motyka, M. Sadzikowski, and T. Stebel, “Lam-Tung relation breaking in Z^0 hadroproduction as a probe of parton transverse momentum,” *Phys. Rev.*, vol. D95, no. 11, p. 114025, 2017.
- [101] G. Aad *et al.*, “Measurement of the Z/γ^* boson transverse momentum distribution in pp collisions at $\sqrt{s} = 7$ TeV with the ATLAS detector,” *JHEP*, vol. 09, p. 145. 55 p, Jun 2014. [Online]. Available: <https://cds.cern.ch/record/1708940>